

# Luminescent and electronic properties of perovskite solar cells

Présentée le 12 août 2022

Faculté des sciences de base  
Laboratoire de photonique et interfaces  
Programme doctoral en physique

pour l'obtention du grade de Docteur ès Sciences

par

**Brian Irving CARLSEN**

Acceptée sur proposition du jury

Prof. J. H. Dil, président du jury  
Prof. M. Graetzel, Dr W. R. Tress, directeurs de thèse  
Prof. A. di Carlo, rapporteur  
Prof. G. Grancini, rapporteuse  
Prof. J.-E. Moser, rapporteur





# Acknowledgements

I would like to thank my entire family for their support throughout my educational path, Profs. Michael Grätzel and Anders Hagfeldt for hosting me in their labs, Dr. Wolfgang Tress for giving me the opportunity to pursue my PhD, the support staff at EPFL, and my colleagues in both the LPI and LSPM groups.

*Lausanne, 29 April 2022*

B. C.





# Abstract

Perovskite solar cells show great promise to serve as an alternative for traditional silicon-based solar cells, however there are still several obstacles blocking their commercialization. Standard perovskite cells contain lead, which is toxic to humans and harmful to the environment. Alternative perovskite compositions offer the opportunity to replace lead with non-toxic metals. Lead can be directly replaced by tin. Unfortunately, tin-based perovskite solar cells do not show the same efficiency or stability as their lead-based counterparts. Using numerical modeling, a study of a current optimized, tin-based solar cell was performed to understand its efficiency limitations and where the most gains can be acquired. While the short-circuit current of the device is high, its limiting factors arise from those already known, primarily the alignment of the electron transport layer with the perovskite conduction band.

Another option for replacing lead is by using a double perovskite. This class of perovskites replaces lead with two different metals that maintain charge neutrality. While providing more compositional freedom compared to the direct replacement of lead, double perovskites offer their own challenges. To better understand transport phenomenon between the transport layers and the perovskite, an investigation into the temperature dependent photoluminescence of  $\text{Cs}_2\text{AgBiBr}_6$  with different hole and electron transport layers was performed. No clear trends appeared allowing a comparison of the transport layers, but some speculations are provided to explain the results common amongst all the samples.

Lead is not the only roadblock for perovskites though, as they also show instability across multiple domains. Two of the most prominent ways instability shows up are closely linked – ionic motion and reversible degradation. A continuation of an insightful paper by Domanski *et al.* was performed to further elucidate the effects of ionic movement on reversible degradation processes. We show that these processes can be controlled by the application of a bias voltage and that the enhancement of these processes by illumination is not significant. We continued the examination of these reversible processes by studying their effects under real-world conditions. Several perovskite solar cells were subjected to real-world conditions in a controlled environment during which we tracked their performance. By comparing the measured data to those calculated if the cells had remained pristine we are able to quantify and separate the reversible from irreversible processes.

Finally, a more fundamental investigation was made into the internal mechanisms of the perovskite cells. A temperature dependent study correlating photoluminescence spectra

and current-voltage curves was performed revealing two different regimes of operation. The potential mechanisms underlying each regime are explored.

Key words: Perovskite solar cells, Lead free, Photoluminescence, Temperature dependence

# Zusammenfassung

Perowskit-Solarzellen stellen eine vielversprechende Alternative zu konventionellen silizium-basierten Solarzellen dar. Es bestehen jedoch mehrere Hürden für ihre Kommerzialisierung. Standard Perowskit-Zellen beinhalten Blei, welches für Mensch und Umwelt schädlich ist. Alternative Perowskit-Kompositionen bieten die Möglichkeit, Blei mit ungiftigen Metallen zu ersetzen. Blei kann direkt mit Zinn ersetzt werden. Unglücklicherweise weisen solche Zinn-basierten Solarzellen geringere Wirkungsgrade und Stabilität auf als die Blei-basierten Zellen. Mittels numerischer Modelle wurde eine Zinn-basierte Solarzelle analysiert um die Limitationen der Effizienz zu verstehen und herauszufinden, wo die größten Effizienzgewinne erzielt werden können. Während der Kurzschlussstrom dieser Zellen sehr hoch ist, scheinen die limitierenden Faktoren hauptsächlich vom Unterschied im Leitungsband der Elektronentransportschicht im Vergleich zum Perowskit herzurühren.

Eine weitere Möglichkeit Blei zu ersetzen ist mittels Doppelperowskit. Diese Klasse von Perowskiten ersetzt Blei mit zwei verschiedenen Metallen, die die Ladungsneutralität aufrecht erhalten. Obschon dies mehr Freiheiten gibt als das direkte Ersetzen von Blei, haben die Doppelperowskite ihre eigenen Hürden. Um Transportphänomene zwischen den verschiedenen Schichten und Perowskit zu verstehen, wurde eine Studie mittels Photolumineszenz von  $\text{Cs}_2\text{AgBiBr}_6$  mit verschiedenen Loch- und Elektron-Transportschichten durchgeführt. Obwohl keine klaren Trends für den direkten Vergleich zwischen den Transportschichten beobachtet werden konnten, werden einige Erklärungsmöglichkeiten der Resultate vorgestellt.

Blei ist nicht die einzige Schwierigkeit für Perowskite, die zusätzlich Stabilitätsprobleme in mehreren Bereichen aufweisen. Zwei der wichtigsten Instabilitäten sind eng miteinander verknüpft – ionische Bewegung und reversible Degradation. Basierend auf einem Artikel von Domanski *et. al.* wurde eine weiterführende Studie durchgeführt, um den Effekt von ionischer Bewegung auf reversible Degradationsprozesse besser zu verstehen. Wir haben gezeigt, dass diese Prozesse durch Anwendung einer Vorspannung kontrolliert werden können. Die Verstärkung dieser Prozesse durch Beleuchtung war insignifikant. Die Studie dieser reversiblen Prozesse wurde weitergeführt, indem die Effekte unter realen Bedingungen getestet wurden. Mehrere Perowskit-Zellen wurden in kontrolliertem Umfeld realen Bedingungen ausgesetzt und der Wirkungsgradverlauf gemessen. Durch den Vergleich der gemessenen Daten mit denen, die berechnet wurden, wenn die Zellen unversehrt geblieben wären, können wir die reversiblen von den irreversiblen Prozessen quantifizieren und unterscheiden.

Schliesslich wurden die internen Mechanismen der Perowskit-Solarzellen auf grundlegendere Art untersucht. Eine temperaturabhängige Studie mittels einer Korrelation von Photolumineszenzspektren und Strom-Spannungskurven offenbarte zwei Betriebsbereiche und die zugrundeliegenden Wirkungsweisen wurden erforscht.

Stichwörter: Perowskit-Solarzellen, Bleifrei, Photolumineszenz, Temperaturabhängigkeit

## Résumé

Les cellules solaires pérovskites représentent une alternative prometteuse pour remplacer les traditionnels panneaux au silicium et dont la production est très énergivore. Cependant d'importants problèmes subsistent, empêchant encore de nos jours leur commercialisation. Les pérovskites de référence utilisent en effet toujours du plomb dans leur composition de base, ce qui représente une source de toxicité néfaste tant pour l'humain que pour l'environnement. Des alternatives existent, le plomb pouvant être potentiellement remplacé, notamment par l'étain. Malheureusement, en termes d'efficacité, les pérovskite à base d'étain ne présentent pas les mêmes performances que ceux au plomb. Via l'utilisation de modèles numériques, une étude approfondie d'une cellule solaire pérovskites à base d'étain a été menée dans le but d'en définir les mécanismes responsables des pertes d'efficacité et de comprendre comment ces dernières pourraient être limitées. Quand bien-même le photocourant électrique généré s'avère performant, la principale perte d'efficacité provient d'un mauvais alignement des bandes d'énergie du transporteur d'électron vis-à-vis de la bande de conduction du pérovskite à base d'étain.

Une stratégie alternative pour le remplacement du plomb est l'utilisation d'un pérovskite double. Cette classe de matériel suggère de remplacer le plomb par deux métaux différents assurant le maintien de la neutralité de charge. Et bien que prometteuse de part la liberté que cette stratégie offre quant aux possible candidats pouvant remplacer le plomb, elle présente aussi ses propres défis. Dans l'optique de mieux appréhender cette classe de matériaux, notamment en ce qui concerne les phénomènes de transport de charges entre les pérovskites et les couches transporteuses de charge, l'investigation de la photoluminescence du pérovskite  $\text{Cs}_2\text{AgBiBr}_6$  en fonction de la température et en utilisant différents transporteurs d'électrons et de trous a été entreprise. Si l'absence de tendance claire n'a pas permis de comparaison directe entre les différents transporteurs de charge, une discussion tente d'expliquer les résultats, semblables parmi tous les échantillons.

Le plomb n'est toutefois pas le seul facteur limitant en ce qui concerne les cellules solaires pérovskites, étant donné l'instabilité de mes matériaux et ce, à plusieurs niveaux. Les deux sources majeurs d'instabilité sont deux phénomènes très proches et liés, à savoir le mouvement des ions au sein du pérovskite et la dégradation réversible. Un article pertinent sur le sujet par Domanski *et. al.* est discuté et des pistes de continuation de l'étude en question sont amenées, avec pour objectif de mieux comprendre et déterminer les effets du mouvement

ionique sur la dégradation réversible. Nous démontrons que ces phénomènes peuvent être contrôlés en appliquant un potentiel de polarisation, et que l'accélération de ces processus n'est pas significative lorsque les pérovskites sont exposés à la lumière. Nous avons poussé nos recherches en étudiant l'étude de ces phénomènes réversibles en étudiant leurs effets en conditions réelles. Plusieurs cellules solaires pérovskites furent sujettes à ces conditions réelles simulées et contrôlées durant lesquelles nous avons mesurés leurs performances. Par comparaison entre les données mesurées et celles calculées dans le cas où les cellules n'avait pas subi de migration ionique, nous furent en mesure de quantifier et séparer les processus réversibles et irréversibles.

Finalement, une investigation plus fondamentale et portant sur les mécanismes internes des cellules pérovskites a été menée. Une étude corrélant les spectres de photoluminescence aux courbes intensité-tension en fonction de la température a été entreprise, révélant l'existence de deux régimes distincts. Les mécanismes régissant potentiellement chaque régime sont explorés.

Mots clefs : Cellules solaires pérovskites, Sans plomb, photoluminescence, Fonction de la température

# Contents

<b>Acknowledgements</b>	<b>i</b>
<b>Abstract (English/Français/Deutsch)</b>	<b>iii</b>
<b>List of figures</b>	<b>xi</b>
<b>List of tables</b>	<b>xix</b>
<b>1 Introduction</b>	<b>1</b>
1.1 Importance of renewable energy sources . . . . .	1
1.1.1 Human well-being and energy consumption . . . . .	1
1.1.2 Climate change . . . . .	2
1.2 Role of perovskite solar cells . . . . .	4
1.3 Development of perovskites . . . . .	6
1.3.1 Fabrication . . . . .	7
1.3.2 Composition . . . . .	8
1.3.3 Transport layers . . . . .	9
1.3.4 2D perovskites . . . . .	12
1.3.5 Tandem solar cells . . . . .	12
1.3.6 Perovskites for other uses . . . . .	13
1.4 Experimental setup . . . . .	14
1.5 Synopsis . . . . .	16
<b>I Lead free perovskites</b>	<b>17</b>
<b>2 Tin Perovskite</b>	<b>21</b>
<b>3 Double perovskite</b>	<b>45</b>
<b>II Physics</b>	<b>59</b>
<b>4 Reversible degradation and ionic movement</b>	<b>63</b>
4.1 Ionic movement and reversible degradation . . . . .	64
4.2 Degradation in the real world . . . . .	81
	ix

<b>5</b>	<b>Temperature dependence of photoluminescent and electronic properties</b>	<b>97</b>
<b>6</b>	<b>Conclusion</b>	<b>109</b>
<b>A</b>	<b>Temperature calibration</b>	<b>113</b>
<b>B</b>	<b>Software listing</b>	<b>119</b>
<b>C</b>	<b>Thot: Data management and analysis</b>	<b>123</b>
<b>D</b>	<b>Instrument listing</b>	<b>125</b>
<b>E</b>	<b>Attributions</b>	<b>127</b>
<b>F</b>	<b>Fabrication methods</b>	<b>129</b>
E.1	Standard superstrate preparation . . . . .	129
E.2	Standard device contact deposition . . . . .	129
<b>G</b>	<b>Methods</b>	<b>133</b>
	<b>Bibliography</b>	<b>151</b>
	<b>Curriculum Vitae</b>	<b>153</b>



# List of Figures

1.1	Human development index (HDI) from 1990 to 2019 as a function of energy consumption per capita per country per year. A clear logarithmic trend is present.	2
1.2	Structure of the perovskite crystal. The A site cations sit at the blue positions at the corners of the cube, the B site cation sits at the black position in the center of the cube, and the X site anions sit at the red sites in the center of the cube's faces [60]. . . . .	6
1.3	Structure of an (a) MAPbI <sub>3</sub> and (b) PbI <sub>2</sub> crystal [69, 70]. (a) The middle molecule is the methylammonium (MA) A-cation, the purple sites represent the iodine X-site anion, and the lead B-site cations are in the center of the green octahedra. (b) The purple dots are the iodine, and the lead resides inside the octahedra. . .	8
1.4	(a) n-i-p and (b) p-i-n cell architectures. The red layer is the HTL, blue is the ETL, dark blue is the perovskite, and light grey is the superstrate. . . . .	10
1.5	Schematic of the experimental set up. Three lasers are available, as well as white and colored LED sources (not shown). A variety of photodetectors are available in conjunction with a monochromator (Mono) and spectrometer (Spectro). To measure electrical signals there is a picoammeter (red), oscilloscope (purple), and galvanometer/potentiometer (yellow). Electrical signals can be driven with a wave function generator (green). Finally, a 4 K cryostat (blue box) is available for temperature controlled experiments, and an integrating sphere (IS) is available to measure absolute quantum yields. Connections between the devices are indicated by the colored circles, and the orange lines indicate possible optical paths for measurement. . . . .	15
2.1	(a) Comparison of the experimentally obtained JV curve and that produced by SCAPS varying the given parameters. (b) Relative errors of the model compared to experimental characterization parameters. (c) Band diagram at V <sub>oc</sub> . Spatial parameters of the layers are indicated by the background color. Red is P3HT, black is MAFASnI <sub>3</sub> , and blue is TiO <sub>2</sub> . . . . .	23
2.2	Effect of absorber layer thickness on characterization parameters. . . . .	27
2.3	Effect of bulk defects on characterization parameters. . . . .	28

2.4	The effect of ETL and HTL alignment on characterization parameters. ETL values are the electron affinities of the $\text{TiO}_2$ layer, and HTL values are the ionization energy of the P3HT layer. All values are in eV. (a) Shows the effect of both parameters, while (b) slices through HTL values, and (c) slices through ETL values. The red boxes in (a) and gray lines both in the plots and on the color bar of (b) and (c) indicate the base parameter values. . . . .	30
2.5	The effect of interface defects at the HTL and ETL on characterization parameters. Values are defect density in $\text{cm}^{-2}$ at the respective interfaces. (a) Shows the effect of both variations, while (b) slices through ETL values, and (c) through HTL values. The red boxes in (a) and gray lines both in the plots and on the color bar in (b) and (c) indicate the base parameter values. . . . .	31
2.6	The effect of bulk mobility of electrons and holes on characterization parameters. Axes show carrier mobility in $\text{cm}^2 \text{V}^{-1} \text{s}^{-1}$ . (a) Shows the variation of both parameters, while (b) slices through hole mobility values, and (c) slices through electron mobility values. The red boxes in (a) and gray lines both in the plots and on the color bar of (b) and (c) indicate the base parameter values. . . . .	32
2.7	The effect of interface defects at the ETL and hole mobility on characterization parameters. Axes show carrier mobility in $\text{cm}^2 \text{V}^{-1} \text{s}^{-1}$ and defect concentrations in $\text{cm}^{-3}$ . (a) Shows the variation of both parameters, while (b) slices through hole mobility values. The red boxes in (a) and gray lines both in the plots and on the color bar of (b) indicate the base parameter values. . . . .	33
2.8	The effect of donor and acceptor concentrations on characterization parameters. (a) The effect on JV characterization parameters of varying both concentrations. The red boxes indicate the base parameter values. Concentrations are in units of $\text{cm}^{-3}$ . (b) The effect of the dopant ratio on characterization parameters. The base value is at 0 where the doping concentrations of $N_a$ and $N_d$ are equal. The horizontal grey bar in the color bar indicates the base level of $N_a$ doping. . . . .	35
2.9	The effect of bulk defects on JV characterization parameters. (a) JV plot of the base model compared to a model with no bulk defects. (b) Comparison of both models to the Shockley-Queisser limit of JV characterization parameters for the base model. All error values are negative. . . . .	36
2.10	The effect of ETL and HTL alignment on JV characterization parameters. (a) JV plots of the different models. (b) The relative change in the JV characterization parameters of each of the optimized models compared to the base model. (c) Comparison of all the models to the Shockley-Queisser limit JV characterization parameters of the base model. All errors are negative. . . . .	37
2.11	The effect of interface defects on JV characterization parameters. (a) JV plots of the different models. (b) The relative change in the JV characterization parameters of each of the optimized models compared to the base model. (c) Comparison of all the models to the Shockley-Queisser limit JV characterization parameters of the base model. All errors are negative. . . . .	38

2.12	The effect of ETL alignment on a model with no interface defects. (a) Energy diagram of the model with no interface defects. Substantial band bending is seen at the ETL interface. (b) JV plots of the model with no interface defects as the ETL energy changes relative to the conduction band of the perovskite layer. (c) The change in JV characterization parameters as the energy of the ETL changes relative to the perovskite conduction band. A positive $\Delta\chi$ indicates the ETL electron affinity is larger than, i.e. towards the valence band of, the perovskite layer. . . . .	39
2.13	The effect of charge mobilities on JV characterization parameters. (a) JV plots of the different models. (b) The relative change in the JV characterization parameters of each of the optimized models compared to the base model. (c) Comparison of all the models to the Shockley-Queisser limit JV characterization parameters of the base model. All errors are negative. . . . .	40
2.14	The effect of applying all previously discussed optimizations to the base model. (a) JV plots of the different models. (b) The relative change in the JV characterization parameters of each of the optimized models compared to the base model. (c) Comparison of all the models to the Shockley-Queisser limit JV characterization parameters of the base model. All errors are negative. . . . .	41
2.15	The effect of the radiative recombination rate $k_r$ on the (a) JV curves and (b) $V_{oc}$ . . . . .	42
3.1	Structure of the double perovskite $A_2BB'X_6$ [133]. . . . .	45
3.2	(a, b) Demonstration (a) order and (b) disorder with the alternating B cation metals. (c, d) (c) Because both metals are coordinated with the same halide atom (green), if (d) the halide is not present the metals can form a covalent bond with each other. . . . .	47
3.3	Example spectra used in the PLQY calculations. . . . .	49
3.4	PLQY parameters for each combination of ETL and HTL, split by pre and post temperature cycling. QFLS is quasi-Fermi level splitting, $\Delta V$ is the calculated voltage loss, $V_{SQ}$ is the Shockley-Queisser limit assuming the PL Peak represents the band gap, PL Peak is the peak position of the PL spectra, PLQY is the photoluminescence quantum yield, and A is absorption. . . . .	49
3.5	Example of the (a) raw and (b) normalized PL spectra at various temperatures. (c) Comparison of the normalized PL spectra for all the samples. . . . .	50
3.6	Example of two reference PL and PLQY calculations used to calculate the PLQY at various temperatures. While the integrated area showed consistent trends of growing with the incident power as expected, the PLQY showed no such trend with respect to incident power. . . . .	51
3.7	Plots showing the calculated PLQY at various temperatures and incident powers. (a) Shows the PLQY against both temperature and incident power. (b) Shows the same data sliced along the incident power axis. The thin opaque lines are the measured data and the broader transparent lines are the sigmoid fits. . . . .	52

3.8	Calculated PLQY for all samples, at all incident powers, both warming and cooling in (a) linear and (b) log scale. . . . .	53
3.9	Example of a sigmoid curve in linear and log scales. . . . .	54
3.10	Sigmoid fit parameters for samples without spiro-OMeTAD. (a) Shows $T_0$ , and (b) shows $T_a$ . . . . .	55
3.11	Sigmoid fit parameters for each sample. (a) Shows $T_0$ , and (b) shows $T_a$ . . . . .	56
3.12	Energy levels of $\text{Cs}_2\text{AgBiBr}_6$ , $\text{TiO}_2$ , spiro-OMeTAD, and P3HT, showing their alignment. . . . .	57
3.13	Example sigmoid fits for the (a) peak position, (b) center of mass, and (c) full width at half maximum. The thin opaque lines are the measured data and the broader transparent lines are the sigmoid fits. . . . .	58
4.1	Design of the experiment. (a) Visualization of the MPP tracking and hold voltage cycling. (b) The hold voltages. . . . .	65
4.2	Example of all the data from a single device during the experiment. This device had the lights turned off during the hold voltage periods. . . . .	67
4.3	Example of the effect of the hold voltage on the power characteristic during MPP tracking. The data shown is for a single device during a single cycle. The power of each is normalized to the final power to accentuate the different shapes. . . .	68
4.4	Example of opposing settling behavior showing degradation and amelioration. The power of each is normalized to the final power to accentuate the different shapes. . . . .	68
4.5	Comparison of JV scans for multiple devices before and after the experiment. .	69
4.6	Example of the fits for a single sample at a single hold voltage. The thin opaque lines are the measured data and the thick transparent lines are the fits of the corresponding data. . . . .	69
4.7	Fit parameters versus hold voltage for a single sample. . . . .	70
4.8	Fit parameters versus hold voltage correlation for all samples. $X$ represents either $P$ or $I$ . . . . .	70
4.9	Example of normalized fit parameters with delta values versus hold voltage for the (a) power and (b) current. Outlying data points with an absolute standard score greater than 2 were removed. . . . .	72
4.10	Example of correlation between $P_1$ and $P_2$ . . . . .	73
4.11	The effect of composition on the power fit parameters in relation to the hold voltage. The composition of the (a) X-site anion and (b) A-site cation is varied. .	74
4.12	The effect of composition on the current fit parameters in relation to the hold voltage. The composition of the (a) X-site anion and (b) A-site cation is varied. .	75

4.13 Example comparison of (a) power and (b) current when allowing the light to turn off (with rest) during the hold voltage, or keeping it on (without rest). The grey shaded regions indicate periods of hold voltage, while the unshaded regions are periods of MPP tracking. The respective power and current traces are from the same devices, while the devices for with and without rest have the same composition. . . . .	76
4.14 Example of the relative difference between the $I_0$ fit parameter and its normalized version $I_{0n}$ for cells with and without rest during the hold voltage periods. The value of the fit parameter when rest was allowed is used as the base value. Inset axes are of the log of the absolute value of the same data. The error bars represent the magnitude of the original error for reference, not the error of the log values. . . . .	77
4.15 Example of fit parameters of during the hold voltage intervals when no rest is allowed. . . . .	79
4.16 Initial cell parameters of the silicon (a, c, e) and perovskite (b, d, f) solar cells. JV scans were performed over a matrix of light intensities and temperature, and the (a, b) PCE, (c, d) $J_{sc}$ , (e, f) $V_{oc}$ were measured. . . . .	82
4.17 (a, b) PCE versus temperature for the (a) silicon and (b) perovskite cell. (c, d) PCE versus illumination intensity for the (c) silicon and (d) perovskite cell. . . .	83
4.18 (a, b) Integrated energy density over the course of the experiment of the (a) silicon and (b) perovskite cell. (c, d) Average PCE over the experiment for the (c) silicon and (d) perovskite cell. (e) Difference in energy density between the silicon and perovskite cell for each temperature-intensity bin. Positive values indicate the silicon cell had a higher energy density. (f) Total incident energy density. . . . .	85
4.19 Daily PCE for the (a) silicon and (b) perovskite cells. The grey lines indicate the instantaneous PCE, the red dots are the daily average PCE when the light intensity was greater than 0.075 sun, and the red and blue area is the temperature. Red indicates temperatures above 0 °C and blue is temperatures below 0 °C. While the temperatures appear different in the plots, they are actually the same. This is an artifact of how the plotting was performed. . . . .	86
4.20 Average daily PCE for the silicon (Si) and perovskite (PSC) solar cells with linear fits. Clear degradation is seen for the perovskite cell. . . . .	87
4.21 The measured and predicted efficiency of the silicon (SHJ) and perovskite (PSC) cell, along with the temperature and intensity. The solid lines are the measured data, while the dotted lines are the predicted PCE calculated from the calibration data given current temperature and intensity the cell is experiencing. . . . .	87

4.22	The measured and predicted efficiencies of the (a) silicon and (b) perovskite cell for each day. The predicted efficiencies are found by linearly interpolating the calibration data. The increasing separation between the measured and predicted PCE of the perovskite cell reveals the degradation occurring, while the measured PCE for the silicon cell shows no such trend, correlating closely with its predicted PCE. . . . .	88
4.23	Visualization of the steps taken to calculate the reversible and irreversible degradation. (a) We first locate the point at which the difference between the measured PCE and the PCE predicted from the calibration data is minimized. (b) We then scale the measured PCE such that the PCE at the point of minimum difference is equal to that of the calibration PCE. (c) The energy losses from reversible degradation are calculated as the difference in energy between the calibration PCE and the adjusted PCE (orange). Energy losses from irreversible degradation are the remaining losses between the adjusted PCE curve and the measured PCE curve (blue). . . . .	90
4.24	Day by day plot of (a) reversible and (b) irreversible energy losses in comparison with the total energy loss. The values for day 0 are due to the measured PCE exceeding the calibration PCE. (c) Stacked plot of the reversible and irreversible degradation for each day. Energy losses are as a percentage of the possible energy as calculated from the calibration data. . . . .	91
4.25	(a) Dependence of energy losses caused by reversible degradation on temperature as a percentage of the total daily energy loss. The value above 1 is from day 0, when the measured PCE exceeded the calibration PCE. (b) Correlation between the temperature and intensity throughout the experiment. The red line is the linear fit. . . . .	92
4.26	Difference in PCE between the first three days – (a, b) day 0, (c, d) day 1, and (e, f) day 2 – of the experiment and after the experiment when those days were run again. (a, c, e) The absolute difference between PCEs. (b, d, f) The relative difference between the PCEs. The grey background indicates regions in the temperature-intensity space that did not occur during that day. . . . .	93
4.27	(a) Mean of the difference between the predicted and measured PCE for each region in the temperature-intensity space over the course of the experiment. (b) Energy loss for each region in the temperature-intensity space throughout the experiment. In both plots, data with intensities lower than 0.1 sun were excluded due to large errors. (c) Total time spent in each region of the temperature-intensity space. Data with an intensity less than 0.075 sun was removed. (d) Total incident energy for each region in the temperature-intensity space over the course of the experiment. This is the same as Fig. 4.18f, reprinted here for convenience. . . . .	94
4.28	Plot of the change in PCE with time as a function of temperature, colored by intensity. . . . .	95

5.1	Visualization of how PLQY and $V_{oc}$ can diverge. (a) With flat quasi-Fermi levels the $V_{oc}$ and quasi-Fermi level splitting are the same. (b) However, when the quasi-Fermi levels bend they differ. . . . .	98
5.2	(a) Circuit diagram of a basic solar cell model consisting of a current source $I_l$ , photodiode, shunt resistor $R_{sh}$ , and series resistor $R_s$ . (b, c, d, e) Effect of varying the (b, d) series resistance $R_s$ and (c, e) shunt resistance $R_{sh}$ values on JV curves and their characteristic values. Insets show the effect on fill factor or $V_{mpp}$ and $J_{mpp}$ . Resistances have arbitrary units. . . . .	99
5.3	Example of the JV curves as a function of temperature. . . . .	101
5.4	The calculated (a) fill factor (FF), (b) $V_{oc}$ , and (c) normalized $J_{sc}$ vs temperature traces for every measurement with intensity larger than 0.5 sun illumination. The inset in (c) is a zoomed version of the same data. . . . .	102
5.5	Example of calculated JV parameters. The short-circuit current density is relative to better show the trends because the absolute values change linearly with intensity. Units of the plots are: Rel. $J_{sc}$ has arbitrary units normalized to the maximum current for each level of illumination, $V_{oc}$ is in Volts, FF is in percent, and the efficiency $\eta$ is also in percent. . . . .	103
5.6	(a) Example of open circuit voltage vs. intensity at various temperatures, used to calculate ideality factor. (b) The calculated ideality factors along with cubic fits. While this data looks quadratic, other data had a cubic shape. . . . .	103
5.7	(a) Example of the raw PL spectra at various incident powers and temperatures. (b) The calculated PL parameters and the same data normalized to the maximum value for easier comparison. . . . .	104
5.8	Example of a correlation of the $V_{oc}$ and integrated PL area. . . . .	105
5.9	(a) Raw JV scans of spiro-OMeTAD at various temperatures. (b) Calculated conductivity from the JV scans. The opacity of the points indicates their relative error, with more transparent having a larger error. (c) Exponential fits of all conductivity experiments, along with the mean fit. . . . .	106
A.1	Schematic showing the different substrates and orientations used for the calibration experiments. . . . .	115
A.2	Peak position as a function of measured temperature for the perovskite on glass with thermal contact, FTO, and aluminum. The vertical lines show the turning point for each trace. . . . .	116
A.3	Peak positions after calibration using the method described. . . . .	117





# List of Tables

2.1	SCAPS parameters of the base model. (a) Layer parameters. (b) Interface defect parameters. (c) MAFASnI <sub>3</sub> recombination model. (d) Parameters that varied during each batch of fitting. . . . .	24
2.2	Characterization parameters of the measured device and base SCAPS model. Most initial values come from the model presented in [122] with modifications from [123, 124, 125]. . . . .	25
2.3	Units for characterization parameters. . . . .	26
2.4	Effect of different optimizations on $J_{sc}$ . Relative change is relative to the base model. . . . .	36
4.1	Average correlation coefficient $r^2$ of each of the two-term exponential parameters across all samples. $X$ represents $P$ or $I$ in their respective rows. . . . .	71
4.2	Relative error between the mean of the fit parameters and their normalized counter parts for cells without rest and with rest across all hold voltages. The rest cells were used as the base value, so the values represent the change of the cells without rest relative to those with rest. Values were weighted inversely to their standard deviation. . . . .	78
4.3	Total energy density produced by each cell throughout the entirety of the experiment. . . . .	84
4.4	Fit parameter values of the instantaneous change in PCE as a function of temperature and intensity. Absolute values are the absolute change in the PCE, while Relative values are the relative change in PCE. Temperature values were computed conditioned on intensity, and vice versa. . . . .	95
A.1	Parameters for each substrate for the temperature calibration function. . . . .	114



# 1 Introduction

## 1.1 Importance of renewable energy sources

### 1.1.1 Human well-being and energy consumption

The material well-being of humans has increased drastically ever since we began using tools. In the last 200 years this growth hit an inflection point, beginning with the Industrial Revolution and leading to our modern society. Although human well-being is ultimately a subjective measure left to the person experiencing their life to judge, there are basic metrics that attempt to quantify the subjective experience of the individual in an objective way across populations. The Human Development Index (HDI) was developed to go beyond the traditional measure of a nation's economy to measure well-being and include other factors. These indicators are made up of life expectancy, educational opportunities, and standard of living [1]. While not perfect, the HDI is a first step towards being able to measure the progress of general well-being across diverse times and cultures [2].

A main facilitator of the improvement in well-being is the increased use of energy [3]. There is a direct correlation between energy consumption per capita and well-being which is seen in Figure 1.1. This is especially true for underdeveloped and developing nations as the relationship between the two is logarithmic [4, 5, 6, 7, 8, 9]. While direct energy consumption can benefit peoples' lives through the use of heating, cooking, transportation, and entertainment, there are many indirect consequences of energy use. Until now all energy sources have been labor intensive to acquire. Whether it was trees pre-Industrial Revolution, coal during the Industrial Revolution, or gas and oil since the end World War One, all require massive human capital. Because a significant amount of this human capital is in the form of physical labor, populations who are resource rich often do not invest in the well-being of their workers. Known as part of the Resource Curse, when a state can derive its income through natural resource exports there is no need to invest in the population to sustain the domestic economy. This leads to the oppression of the population because the government does not need to rely on taxes for income, so has no incentive for workers to earn their own income [10, 11]. We see these indirect impacts in oil rich regions such as the Middle East, the Gulf States, and Central

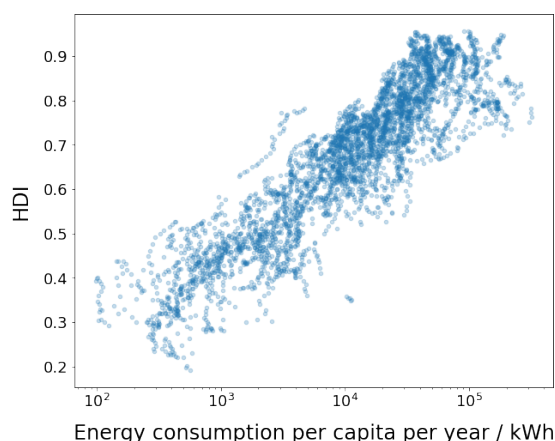


Figure 1.1 – Human development index (HDI) from 1990 to 2019 as a function of energy consumption per capita per country per year. A clear logarithmic trend is present.

Africa where foreign actors intervene, either directly as was the case in and after World War Two, or indirectly via proxies as is occurring in Yemen since 2014. The battle for resources creates instability for those living in the region, and as is often the case those without power are most effected.

Until now, our main source of energy has come from burning carbon based fuels – first in the form of wood, and now in the form of gas and oil. A major benefit of these resources is that they store their own energy in the form of chemical bonds. This allows the energy concealed within to be easily stored and transported. When releasing the energy from these fuels, the carbon, whose bonds stored the energy, reacts with oxygen forming  $\text{CO}_2$ . This  $\text{CO}_2$  is then released into the atmosphere and has led to the significant increase in atmospheric  $\text{CO}_2$  we have today. Because  $\text{CO}_2$  is soluble in water, the increased concentration of atmospheric  $\text{CO}_2$  has also led to increased concentrations of oceanic  $\text{CO}_2$ .

### 1.1.2 Climate change

$\text{CO}_2$  has two properties that has knocked our ecosystem out of its pre-Industrial Revolution equilibrium. The first is that it has a resonant energy level in the infrared wavelength [12, 13]. This means that it traps the heat energy radiated from the Earth, acting as an insulator. This could lead to the warmest global temperatures in 34 million years, at a rate that is more than ten times faster than it would be otherwise [14, 15, 16]. The other property  $\text{CO}_2$  has that has affected our ecosystem is its acidity. Much of the  $\text{CO}_2$  released from the burning of fuels has been absorbed by the oceans, acidifying them [17].

The increase in global temperature has already caused an increase in both the frequency and intensity of extreme weather events [18, 19]. This includes floods, droughts, storms, and fires. Swiss Re – the world's largest reinsurance company – estimates that by mid-century the global economic output could drop by 10% relative to a world without anthropogenic climate change

[20]. However, this value ranges from a best case scenario, outlined under the Paris Climate Accord, of a 4.2% drop to the worst case scenario, where no mitigation strategy is pursued, creating a drop of 18%. The brunt of this impact will be taken by those populations who are already most vulnerable.

So far the ocean has been able to act as a carbon and heat sink, absorbing between one-quarter and one-third of the additional CO<sub>2</sub> released by humans and roughly 90% of the heat energy that has accompanied this [21, 22, 23]. This has tempered the impact humans have felt from the CO<sub>2</sub> release. However, the rate at which the ocean can absorb CO<sub>2</sub> depends on its pH level, as well as the surface level of dissolved CO<sub>2</sub> [17, 24]. As the ocean absorbs more CO<sub>2</sub> it acidifies, reducing the amount of CO<sub>2</sub> it can absorb in the future. There is also a positive feedback loop occurring. The warming ocean has changed its current, reducing the mixing taking place [23]. This means that new water is not being replaced at the surface to allow efficient absorption of the atmospheric CO<sub>2</sub>, creating more atmospheric CO<sub>2</sub> furthering the warming, and reducing the ocean's effectiveness as a heat and carbon sink.

The direct impact of ocean acidification from the absorption of CO<sub>2</sub> has resulted in wide spread coral bleaching events and the mass extinction of fisheries [25]. These aquatic ecosystems not only provide economic activity for local peoples by way of tourism and commerce, they also act as protection against oceanic events. Coral and oyster reefs act as break waters against storm swells shielding those in low lying areas from the full brunt of the damage [26, 27].

The effect on oceanic wildlife is significant. Both ocean creatures with shells and coral depend on aqueous CaCO<sub>3</sub> to form their protective layers [17]. However, with the absorption of CO<sub>2</sub>, the available CaCO<sub>3</sub> has significantly decreased. This has left these animals without defense and vulnerable to predators and other environmental factors. Algae and plankton have also been negatively affected by ocean acidification [17, 28]. Again, these effects have multifaceted impacts. First, both algae and plankton are at the base of the food chain, forming the foundation of the oceanic ecological pyramid. Decreasing amounts of either of these will have ripple effects that affect the entire ecosystem in significant ways. Not only do both of these form the foundation of the pyramid, they also play their own important roles in the carbon cycle. Algae is one of the most abundant plants on earth and is incredibly efficient at absorbing carbon, up to 400 times more efficient than trees when aided by humans [29]. This obviously presents a massive opportunity to capture oceanic CO<sub>2</sub>. Plankton, while also utilizing carbon directly, aids in the carbon sequestration process in another way [30, 28, 31]. When they die they begin to sink to the bottom of the ocean in a process known as *marine snowfall*. This creates a carbon flow from the surface to the oceanic depths creating a carbon pump, mitigating the effects of the current stagnation discussed before.

Apart from CO<sub>2</sub>, burning fossil fuels also releases NH<sub>3</sub>, HNO<sub>3</sub>, and H<sub>2</sub>SO<sub>4</sub>. These further decrease surface seawater alkalinity, particularly near the coast where they have a greater direct impact on human populations [17].

A strong push from scientists, citizens, and governments world-wide has begun after the

recognition of the urgency of the situation, however significant and rapid action must be taken if we wish to reduce the impact of our warming globe on our ecosystem. An increase of 2 °C has been found to be the threshold for linear effects of global temperature rise, after which the consequences become non-linear and could result in an earth that is uninhabitable not only for humans but for many of today's plants and animals [32].

Apart from the global impact of climate change there are many local impacts from hydro-carbon fuel sources. Like the global effects, local effects also tend to effect poorer people disproportionately [33, 34]. In the United States poorer communities are often downwind of centers of commerce and industry [35, 36, 37]. This is not a coincidence. Wind carries air born pollutants from these centers with it, thus lowering the value of the downwind land. Fuel pipelines are diverted from wealthy areas and into the lands of native peoples, such as was the case for the Keystone XL and Dakota Access pipelines [38, 39, 40].

While increased energy use has lifted, and will continue to lift, millions of people out of poverty, the negative impacts of traditional energy source are beginning to outweigh their benefit. As technology has advanced we have both acquired the tools to destroy and save ourselves as a species. Until now the incentives for behavior that prioritizes short term gains over long term benefits have ruled the global economy. This is especially evident in the legal responsibility for publicly traded companies to maximize profits for their shareholders. There is no room allowed for considerations of the climate, well-being of local residents, or secondary and tertiary effects of the business' decisions unless they play directly into the revenues of the company. This compounds the human psychology of placing more importance on short term events over long term ones. Climate change is not only a technological issue, it is a psychological one as well [41, 42]. Thus, just having sufficient technology to solve the problem is not enough, we must have technology that is aligned with our short term economic incentives to make the rapid changes needed to solve the impending climate crisis.

## 1.2 Role of perovskite solar cells

By moving away from fossil fuels, the benefits of additional energy consumption can be spread while mitigating the negative impacts of additional CO<sub>2</sub> and other pollutant release. While a sustainable energy grid will need to incorporate a diversity of energy sources to deal with intermittency, solar energy has the potential to be the largest contributor in a fully sustainable grid [43].

Current consumer solar cell technology is silicon based. Silicon is abundant, making the raw materials cheap, and stable, meaning the solar cells produced from it last 20 to 25 years. As recently as 2015 a significant portion of the cost of silicon solar cells were still coming from obtaining, purifying, and processing the silicon. However, in the past several years these costs have greatly decreased, largely due to economies of scale, and in 2020 the price of electricity for some solar systems had become cheaper than any other source [44, 45, 46]. Even with these amazing developments, there is still room for improvement.

Silicon solar cells are brittle, meaning they need to be housed in a protective case, usually made of metal. This increases the weight of each of the solar panels, requiring a sturdy scaffold to support them, further increasing the weight of the system. This also means that the cells must have a flat surface on which to rest. These two requirements greatly restrict the areas on which silicon solar panels can be installed. Another major issue is not a technical one, but an aesthetic one. Homeowners do not like the sight of solar panels covering their clay tile roofs, for instance. This led Solar City, now owned by Tesla, to produce the Solar Roof [47]. Perovskite solar panels may be able to address both these issues, as well as continue to drive down the price of solar energy.

Because perovskites are a direct band gap semiconductor they have an extremely high absorption coefficient, requiring about 500 nm of active material. This is 10 to 1000 times less material than needed in the active layer of a silicon solar cell, which requires a thickness of tens or hundreds of micrometers [48, 49]. This results in the perovskite cells being significantly lighter than silicon cells. Further, perovskite cells can be deposited on flexible substrates allowing them to be adapted to a variety of surfaces and removing the requirement of a mechanically protective casing and scaffold [50]. These two factors alone have the potential to significantly decrease the balance of system cost when purchasing a solar energy system. These advantages appear in other ways as well.

Because perovskites are solution processed, they can be sprayed on to their substrate. Along with their flexibility, this allows them to be roll-to-roll processed using low temperatures, which could result in a significant cost advantage relative to silicon cells [51].

A key metric to analyze when evaluating the cost of an energy source is the levelized cost of energy (LCOE) which is a measure of the cost of each unit of energy taking into consideration all the costs of the system over its lifetime [52].

$$\text{LCOE} = \frac{\text{Total cost of the system over its lifetime}}{\text{Total energy produced by the system of its lifetime}}$$

There are still many technical advances that need to be made for perovskite solar cells to become commercializable, but ultimately it is predicated that they could produce energy at roughly between 90% to 65% the cost of silicon cells depending on the size of the installation [53, 54]. This fraction is even further reduced when considering tandem perovskite-silicon cells. Another important measure that perovskites show great promise in is their energy payback time (EPBT). This measures the amount of time required for the solar cell to produce more energy than it took to be produced. Due to the high temperatures required for silicon cells, their EPBT is around two years. However, the solution processed, low-temperature fabrication of perovskites can bring this time down to about six months [55]. This reduced EPBT is a critical metric of a solar cell's life cycle, pointing to the additional benefits perovskites provide over traditional solar cells. There is still a ways to go until this energy payback time is viable though, as the short lifetime of the perovskite cells currently overwhelm this benefit.

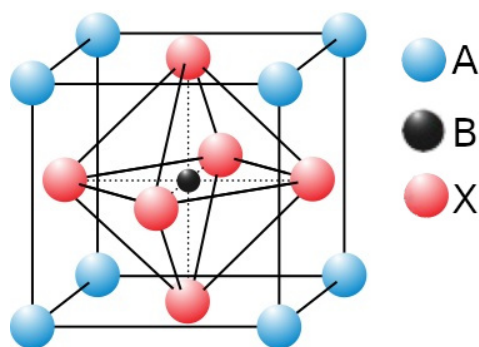


Figure 1.2 – Structure of the perovskite crystal. The A site cations sit at the blue positions at the corners of the cube, the B site cation sits at the black position in the center of the cube, and the X site anions sit at the red sites in the center of the cube's faces [60].

Ultimately the hope is that the flexibility in use requirements and reduced manufacturing costs of perovskite solar cell will help make solar energy more economically attractive than traditional carbon-based sources, as well as allow the democratization of energy by penetrating into areas of the world that have not yet benefited from increased energy availability, lifting up the well-being of humans across the globe.

### 1.3 Development of perovskites

Perovskites have a longer history than the current hype around the material suggests. Discovered in the mid 1800's, the original perovskite material,  $\text{CaTiO}_3$ , received limited interest for a century [56, 57]. Then, in the 1950's, perovskite's commercial uses became apparent, spurring research on their development. However, it was not until the early 1990's that perovskite's optoelectronic properties became a main focus [58, 59]. At this point *perovskite* had come to refer to any material with the general chemical formula and crystal structure of the original perovskite mineral  $\text{CaTiO}_3$ ,  $\text{ABX}_3$  with a cubic unit cell, which is shown in Fig 1.2. In this formulation A is a monovalent cation, B is a divalent cation, and X is a monovalent anion.

Modern perovskites garnered their initial interest as light absorbers for use in dye-sensitized solar cells. In 2009 modern perovskite were born with a publication from Kojima and Miyasaka, who synthesized a dye-sensitized solar cell using  $\text{MAPbI}_3$ , a perovskite, as the sensitizer [61]. Then in 2012, Grätzel and Park created the first solid state perovskite solar cell, setting off the current research trends in the field [62]. These first solar cells had a low power conversion efficiency of less than 4%. Over the next ten years efficiencies quickly increased with current day cells exceeding 25%. This has shifted the burden of perovskites from proving their efficiency, to proving their stability.

This rapid improvement in efficiency can be split into five focuses. The first focus was on optimizing and understanding the fabrication process of perovskites. Once the fabrication processes had been well established, researchers began to investigate how the composition



of the material affects its properties. This led to the inclusion of novel A-site cations and an understanding of how the X-site halide affects the material. By optimizing these two focuses, the first significant gains in efficiency were made. Researchers then began using additives to modify and tune the perovskite's behavior. Most recently, researchers have been exploring alternative perovskite materials. This includes lead-free materials to make it non-toxic, and the development of 2-dimensional perovskites.

### 1.3.1 Fabrication

Perovskites were first fabricated using a single step deposition. First, a precursor solution is prepared by mixing an organic halide, AX, with a metal halide  $BX_2$  in an aprotic, polar solvent such as DMF or DMSO. This solution is then deposited onto a superstrate. For typical cells, this superstrate is glass covered with a transparent conductive oxide. Various intermediate layers are also be present to aid in charge extraction, which is discussed in more detail in Section 1.3.3. The superstrate is then spin coated with the perovskite precursor solution. The sample is annealed, most typically on a hot plate, to crystallize the perovskite. Later, it was found that by using toluene as an antisolvent cell stability and efficiency could be enhanced [63]. This antisolvent method is still one of the most widely used deposition techniques.

From the original single step method, the two-step method emerged [64]. The two-step method begins by depositing a layer of metal halide  $BX_2$  onto a superstrate. AX is then added to this by dipping the superstrate into a solution containing AX, or spin coating an AX solution onto the superstrate. The sample is then annealed as in the one-step method. The advantage of the two-step method is that it produced more homogeneous and densely packed films than the one-step method.

Finally, evaporation methods have been developed. Both vapor assisted solution processing and thermal evaporation are used to create more homogeneous films than the one- or two-step methods can produce [65]. Evaporation methods also remove the need for high temperature annealing, and the use of solvents. Along with their high quality film morphology, these could enable large area, stable perovskites. While both these methods produce high quality perovskite films and allow for fine tuned control over the composition, they may not be commercializable for single junction perovskite solar cells due to their cost [66]. Neither method easily scales to industrial sizes as they require sealed deposition chambers, and the fabrication process is significantly slower than other methods, limiting their production efficiency. They do, however, show promise in multijunction solar cells, especially those using a tandem approach with a silicon bottom layer and perovskite top layer.

Alternative fabrication steps are also being investigate now. One of these technologies is flash infrared annealing (FIRA). Using this method allows for high throughput fabrication by cutting down on the annealing time needed with the one and two step fabrication processes [67].

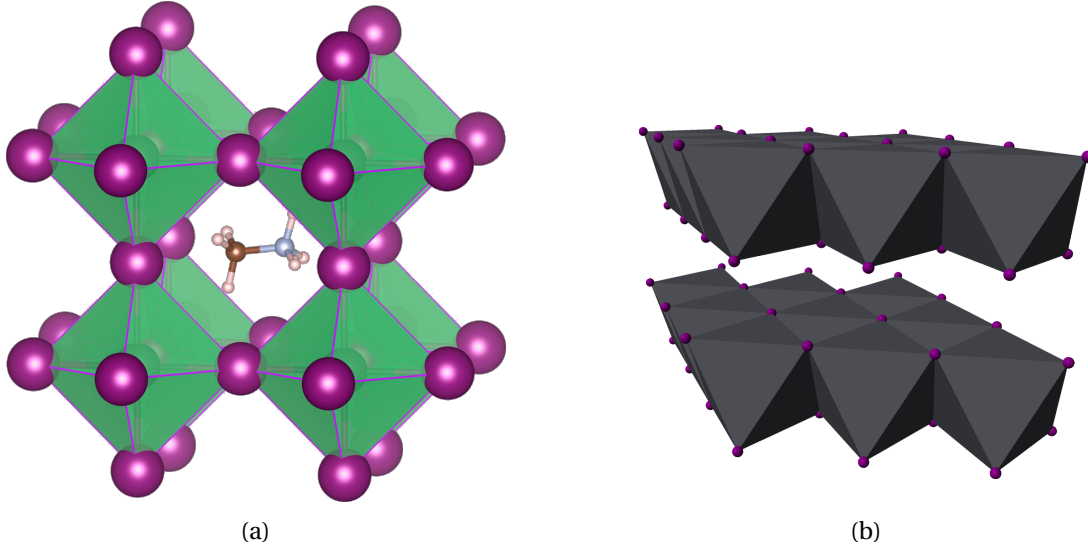


Figure 1.3 – Structure of an (a)  $\text{MAPbI}_3$  and (b)  $\text{PbI}_2$  crystal [69, 70]. (a) The middle molecule is the methylammonium (MA) A-cation, the purple sites represent the iodine X-site anion, and the lead B-site cations are in the center of the green octahedra. (b) The purple dots are the iodine, and the lead resides inside the octahedra.

### 1.3.2 Composition

The classic perovskite composition of  $\text{MAPbI}_3$  brought the field a long way and is still used as a benchmark. However, the three components of the perovskite structure – A, B, and X – allow for a great deal of compositional fine tuning. After the establishment of  $\text{MAPbI}_3$  these tuning options were quickly explored by taking a combination of species for each component to adjust the properties of the perovskite.

The main purpose of the A-site cation is to hold the cubic structure formed by the B and X ions open. For instance, in the standard perovskite formulation of  $\text{MAPbI}_3$  if the methylammonium (MA) is removed  $\text{PbI}_2$  is created and the corner-shared octahedra formed by the lead and iodide collapse into a crystal with edge-shared octahedra, as seen in Fig. 1.3. It has been found that the A-site cation does not play a significant direct role in the electronic structure of the material as the valence and conduction bands are composed of the  $\text{B}_s\text{-X}_p \sigma^*$  and  $\text{B}_p\text{-X}_p \sigma^* \pi^* \pi^*$  orbitals respectively [68]. However, the A-site cations can have an indirect influence on the band structure by inducing stress into the crystal structure.

The suitability of a species to act as an A-site cation can be initially assessed using the Goldschmidt tolerance factor.

$$t = \frac{r_A + r_B}{\sqrt{2}(r_A + r_X)}$$

where  $r_S$  is the ionic radius of the corresponding species with  $S \in \{A, B, X\}$ . For a species to have a chance of forming a perovskite structure, the tolerance factor must be between roughly

$t = 0.8$  and  $t = 1.0$  [71]. This puts a tight size constraint on the species that can fulfill this role. All that being said, the A-site cation does not need to consist of a single species. By varying the composition of the species forming the A-site cation a wide range of behaviors can be created.

Typical A-site cation species in modern perovskite cells are methylammonium (MA), formamidium (FA), and cesium (Cs), with other species such as rubidium (Rb) and guanidinium (Ga/Gua) also having been explored. By optimizing the relative concentrations of each of these components the band gap can be tuned, environmental stability can be enhanced, and dynamic behaviors – such as ionic motion and current-voltage hysteresis – can be suppressed [71, 72, 73, 74].

As stated before the B-site cation is directly responsible for the formation of the conduction and valence bands, predominantly forming the conduction band [75]. The most common B-site cation used today is lead. However, because lead is toxic to both humans and the environment en masse, a search for alternatives has come to the forefront of research. This has opened up the frontiers of tin-based perovskites, as well as the class of double perovskites. Lead and tin are similar enough that tin can be used to directly replace lead – they are both group 14 heavy metals with almost the same ionic radii. Double perovskites, on the other hand, use two atoms to replace lead. To do this the atoms must maintain charge neutrality, replacing the single  $B^{2+}$  atom with one  $B^+$  and one  $B^{3+}$  atom, doubling the size of the unit cell length. This is most commonly done by pairing a trivalent, group 15 heavy metal such as bismuth, antimony, or indium with silver, which is monovalent [76]. The changes made to form these double perovskites significantly change their properties compared to traditional perovskite cells, and demand their own line of research.

The final component of the perovskite structure is the X-site anion, which is predominantly responsible for the formation of the valence band [75]. Iodine, bromine, and chlorine are the only elements currently being used in this position. Varying the X-site species allows the bandgap of the material to be tuned anywhere from 400 to 800 nm [77]. Similar to the A-site cation, the X-site anion can be a combination of species.

### 1.3.3 Transport layers

In order to efficiently extract charge carriers produced in the perovskite bulk, selective contact layers are used. It is critical that these layers allow for easy transport of their selected charges, electrons at the electron transport layer (ETL) and holes at the hole transport layer (HTL), while blocking the opposite type of charge. Perovskites can be built in two architectures. n-i-p – which has the ETL contacting the superstrate – and p-i-n – which has the HTL contacting the superstrate. This is demonstrated in Fig. 1.4. In either case the light always passes through the superstrate before interacting with the active components of the solar cell. This presents an interesting design challenge for whichever layer is contacting the superstrate as it must be optically transparent to allow the active components of the solar cell to absorb as much light as possible. The layer contacting the superstrate may also serve as a scaffolding material for

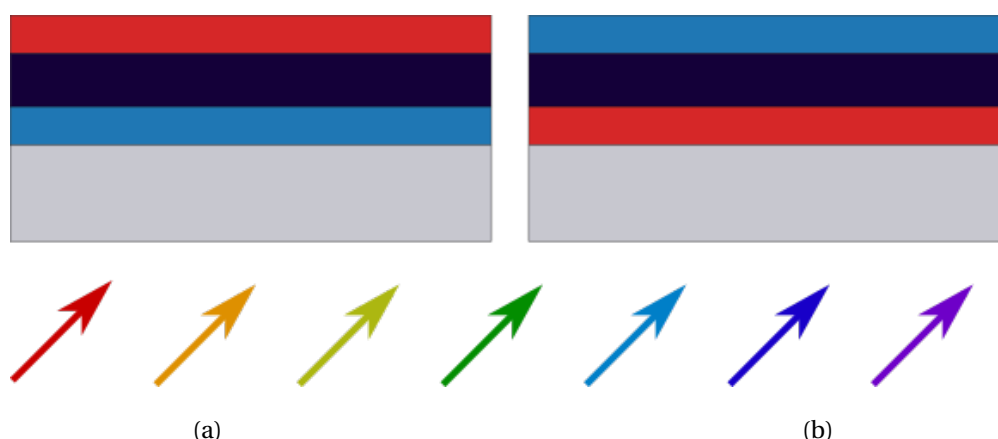


Figure 1.4 – (a) n-i-p and (b) p-i-n cell architectures. The red layer is the HTL, blue is the ETL, dark blue is the perovskite, and light grey is the superstrate.

the perovskite to what to, ensuring good electrical and physical contact between the layers. This adds a further design constraint on the materials available to serve this role.

TiO<sub>2</sub> was the original ETL and is still the most common one used in n-i-p architectures to date. It has good alignment with standard perovskite conduction bands and has a deep valence band creating the charge selectivity required for an operational solar cell. However, ETLs are not one size fits all. For alternative perovskites, such as tin-based ones, TiO<sub>2</sub> as an ETL is one of the main limiting factors in performance. This is explored further in Chapter 2. TiO<sub>2</sub> also shows degradation under UV light, contributing to the already tenuous stability of perovskite cells. From a commercialization viewpoint, traditional TiO<sub>2</sub> deposition requires high temperatures which could be a cost barrier [78]. While alternative fabrication methods may offer a path towards lower cost fabrication methods, as well as allowing TiO<sub>2</sub> deposition to be integrated into larger scale production flows such as roll-to-roll printing, these limitations are enough to prompt an investigation into alternative materials to serve as the ETL [79].

Other common ETL materials that have been used in the n-i-p architecture are SnO<sub>2</sub>, which has shown better environmental stability than TiO<sub>2</sub>, and ZnO, which offers more flexibility compared to TiO<sub>2</sub> [80, 81]. There are also a host of other more complex solutions, such as using nanoparticles and interlayers, that show promise for increasing ETL performance.

In the p-i-n structure more freedom is allowed when developing ETL materials as they no longer need to be transparent. This has allowed the use of organic and polymer materials to be explored as a charge transport material. The most common of these is PCBM. Using these large molecular systems as a transport layer has tended to result in the reduction of hysteresis and defect passivation at their interface [80, 82]. These molecules are also often much cheaper to fabricate and deposit than TiO<sub>2</sub> and other metal-based ETL materials, and are more flexible, making them an attractive option when looking towards commercialization.

Spiro-OMeTAD (spiro) was the material that really drove the rapid efficiency boom in perovskite solar cells and is still the standard HTL material used for n-i-p architectures. It allowed perovskite cells to move from a liquid junction solar cell to being completely solid state, a major achievement for the technology [62]. While the advancement spiro offered was significant, there are several drawbacks to the material. Spiro does offer good alignment with the valence band of most popular perovskite compositions as well as good electron blocking due to its large bandgap, however, as noted before, a one-size fits all solution will not be optimized for any single case. The somewhat large offset of spiro's highest occupied molecular orbital (HOMO) energy level and the perovskite valence band results in open circuit voltage losses up to a few hundred millivolts. This is a significant loss for a material with a band gap between one and two electron-volts [83]. Spiro also shows issues with its environmental stability. Because it is more stable than perovskite to oxygen and moisture it does offer some protection to the perovskite layer. However, when considering the timescale that solar cells must be operational to allow for commercialization – tens of years – it is still lacking in this area. Further, pure spiro does not have the high conductivity required for efficient charge transport, and so must be doped with lithium [84]. These lithium ions can migrate into the bulk of the perovskite causing both reversible and irreversible degradation [85]. This is not just a one-way relationship though, as ions from the perovskite can also migrate into the spiro layer degrading its electrical properties [86].

PTAA is the other classic HTL material for use in n-i-p architectures. It has many of the same properties as spiro leading to its enduring popularity [84]. This includes its easy fabrication, relatively good thermal and moisture stability, and good electrical properties. However, with the good also comes the bad, and PTAA also requires doping to enable higher cell efficiencies leading to similar degradation mechanisms that are present with spiro.

In recent years the exploration of novel HTL materials has increased to address these issues, especially those that acts as barriers to commercialization, such as cost. One of the materials gaining interest for this use is P3HT. It is a low cost, high conductivity material that is easy to fabricate, making it ideal to take steps towards commercialization. Unfortunately, by itself it can not enable high efficiency solar cells mostly due to the high non-radiative recombination it creates at the perovskite interface [87]. To alleviate this unwanted recombination requires additional engineering, often in the form of interlayers further increasing the complexity of the solar cell.

With the recent interest in tin-based perovskites, the p-i-n architecture has become more relevant to prevent the oxidation of the tin that is aided by the  $\text{TiO}_2$  [88]. This is discussed further in Chapter 2. To enable this PEDOT:PSS has become a favorite HTL material for this architecture. It is optically transparent and easy to fabricate and deposit. However the HOMO energy level of PEDOT:PSS is not well aligned with the typical perovskite valence band resulting in large losses in open circuit voltage. It can also accelerate the degradation of the perovskite layer due to its hydrophilicity [89].

### 1.3.4 2D perovskites

While standard perovskites have shown promise, especially with their rapid increase in efficiency, they still have one major obstacle, stability. A standard perovskite solar cell lasts only about one month before significant degradation occurs. This is mainly caused by the perovskites reaction with both water and oxygen present in the atmosphere. To address this issue, 2D perovskites have started to gain traction.

One of the main drivers of the degradation of a standard 3D perovskite is its interaction with water. The hydrophilicity of a typical perovskite, though, can be flipped to hydrophobicity by breaking apart the structure with spacer molecules. This results in a layered structure alternating between the perovskite material and the spacers. It is this structure of perovskites that we refer to as *2D perovskites*.

2D perovskites have shown a significant improvement in environmental stability over their 3D counterparts, remaining operational for thousands of hours [90]. The cause of this stability arises from two factors. The first is that the spacers used to separate the perovskite layers are large molecules compared to the typical A-site cations used in 3D perovskites making them less volatile. They are also typically more hydrophobic than the usual A-site cations, providing an internal defense against water that has penetrated the material [91]. The second source of this stability is due to the enhanced thermodynamic stability that their surfaces offer. It is usually the case the surfaces are high energy compared to the bulk of a material, however the opposite behavior is observed for perovskite. The cause of this thermodynamic favorability has been a hotly debated topic, but likely comes from the different termination surfaces that are available in a perovskite. The 2D material also allows for more structural deformation than its 3D counterpart, allowing the crystal to relax into a more favorable state [92].

While 2D perovskites offer the significant benefit of better stability, they suffer from a low efficiency relative to 3D perovskites. This is caused by a large band gap, high binding energies and poor charge transport. To get the best of both worlds, a combination of 2D and 3D perovskites have been investigated. The 2D perovskite is used as a sort of armor for the 3D bulk to protect it from the environment, while the 3D perovskite is the main active component of the solar cell to maximize its efficiency [93].

### 1.3.5 Tandem solar cells

Another promising use for perovskites is in combination with a traditional silicon solar cell. By stacking multiple layers of solar cells on top of each other, the efficiency of the module as a whole can be increased significantly. In the limit of stacking infinitely many solar cells with band gaps from 0 to infinity one could acquire an efficiency of about 68% [94, 95, 96]. Unfortunately a cell with an infinite gradation like this has not yet been discovered. In pursuit of it though, perovskites offer a good companion to silicon cells. Jumping from one type of solar cell to two already increases the limiting efficiency from 33% to 42%, an almost 50%

elevation from the ceiling imposed by Shockley-Queisser limitations.

Using a large band gap perovskite on top of standard silicon cell offers two immediate benefits. First, the module as a whole gains significantly in efficiency. While both large area perovskite cells, and typical commercial silicon cells have efficiencies of around 22%, tandem cells are already exceeding efficiencies of 29%, a 30% increase [97, 98]. Additionally, the silicon solar cell acts as an environmental barrier for the perovskite, aiding in its stability. Because silicon modules already require a significant amount of encapsulation for mechanical robustness, the perovskite can piggyback on this protection for little additional cost. These cells do still offer challenges though. First, by combining the two materials the module becomes more complex to both manufacture and operate [99]. And perhaps more importantly, even though the perovskite is encapsulated, its lifetime is still significantly shorter than that of the silicon cell. This results in a shortening of the module's lifetime as a whole. Tandem silicon-perovskite cells are already receiving lots of attention. Companies such as Oxford PV have raised millions of dollars of investment to bring this technology to market [100]. Even with all the promise of this technology nearing its market release, we have still yet to see it available in any significant manner.

### 1.3.6 Perovskites for other uses

Perovskite materials exhibit many interesting phenomena and a wide array of structures. The solar cells discussed so far have fallen under the class of hybrid, organometallic, halide, and thin films perovskites. Perovskites offer many other variations though including all inorganic, non-halide, single crystal, and quantum dots, each of which has its own unique properties.

Just as any other solar cell, perovskites can be used as light emitting diodes (LEDs). The advantage to using perovskites over standard LED materials such as gallium arsenide and other III-V semiconductors is their easy band gap tunability and cheap fabrication. Their sensitivity to light also enables their use as photodetectors. The same properties that are important for perovskite as a solar cell and LED material are present here – namely their band gap tunability and cheap and easy fabrication. Another main advantage for perovskites as photodetectors is their direct band gap which gives them a significantly increased photosensitivity over an indirect band gap material, for instance silicon [101]. The photoproperties that perovskites exhibit can also make them useful as chemical detectors [102]. Apart from the photoproperties of perovskites, there have also been reports that they are ferroelectric and piezoelectric [103, 104]. The wide range of materials that the perovskite family encompasses is reflective of their potential uses and applications. Combined with their cheap and easy fabrication, this points to the increased use of these materials as we move forward, and begs for continued research in the field.

## 1.4 Experimental setup

To investigate the properties of perovskite solar cells, we used optical and electronic measurements. The experiments, which include wavelength and time resolved photo- and electroluminescence (PL, EL, TRPL, and TREL), provide multiple methods to probe the properties of the perovskite material. In addition, temperature dependent measurements were enabled with the integration of a cryostat.

To allow for a wide range of experiments, a custom experimental setup was built. Due to the poor reproducibility of the properties of perovskite solar cells, I wanted to have a statistical approach to my research. To accomplish this much of the experimental setup was automated and designed in a way that allowed the incorporation of a variety of experimental techniques. The design of the setup was modular so new experiments could be added as needed. A schematic of the setup is shown in Fig. 1.5.

For optical spectroscopy three experiments were installed. A free standing sample holder allowed samples to be illuminated in a transmission and reflection configuration. Samples could also be placed on an integrating sphere (IS) to measure absolute quantum yields. A 4 K cryostat (blue box) was available for temperature controlled experiments. For each of these setups, the samples could be optically or electrically driven. The luminesced light was directed to a spectrometer (Spectro), an avalanche diode (SPAD), or a photodiode with a 1 ns rise time (ns). The light could also be passed through a monochromator (Mono) before arriving to the SPAD or photodiode. For illumination, three lasers as well as white and colored LED arrays (not shown) were available. The lasers consisted of a red (660 nm) and blue (422 nm) continuous wave lasers, and a green (532 nm) pulsed laser with a 2 ns pulse width.

For electrical spectroscopy an oscilloscope (purple), picoammeter (red), and galvanometer/potentiometer (yellow) were available. Samples could be illuminated by the lasers and LED arrays, or driven by a function generator (green). Samples could also be placed in the cryostat for temperature dependent measurements. For details about the commonly used instruments throughout this thesis refer to Appendix D

In addition to the hardware setup, a significant amount of software was created to automate and control experiments. Automating these experiments removed the possibility of experimenter error when running them, as well as enabled experiments that would not be feasible otherwise. Many experiments required the coordination of multiple pieces of equipment or ran over long periods of time. A listing of the software created can be found in Appendix B.

To aid with data analysis, a software program called Thot was created. This software allows multiple pieces of data to be integrated automatically, significantly increasing the analysis speed when performing statistical analysis. A further explanation of this software is found in Appendix C.



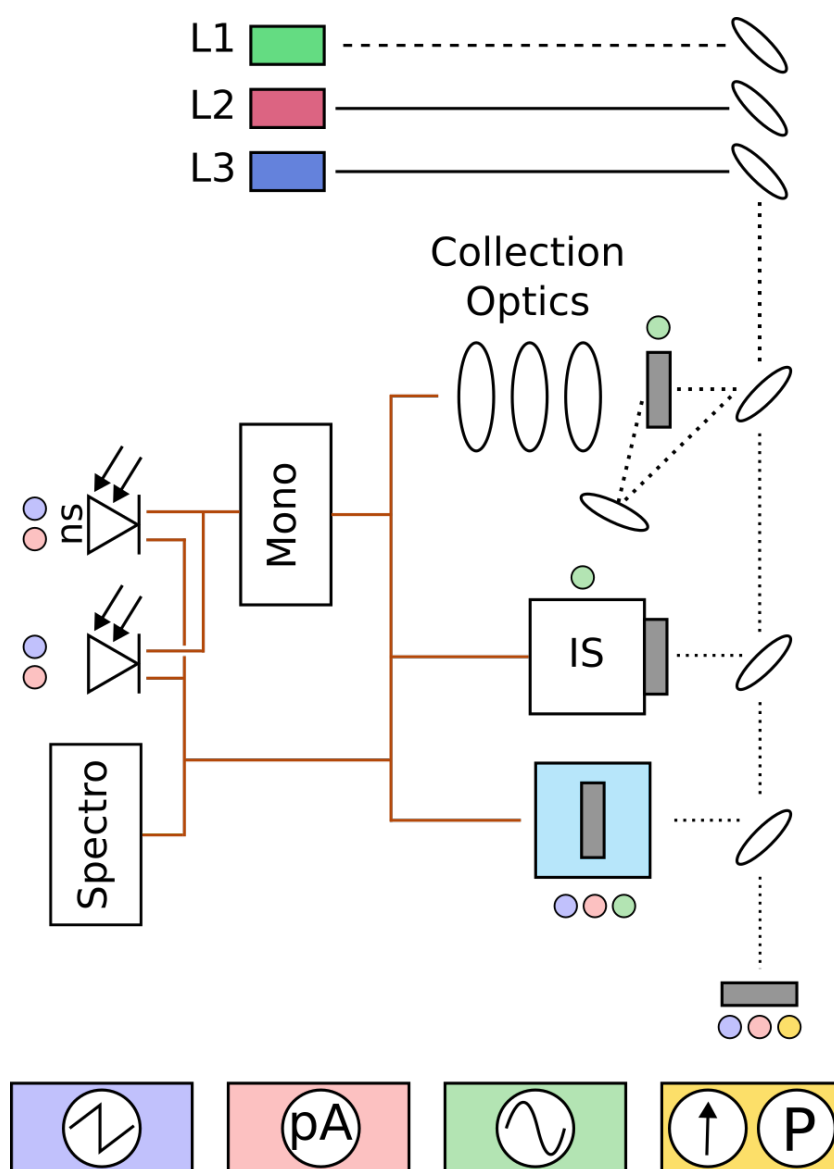


Figure 1.5 – Schematic of the experimental set up. Three lasers are available, as well as white and colored LED sources (not shown). A variety of photodetectors are available in conjunction with a monochromator (Mono) and spectrometer (Spectro). To measure electrical signals there is a picoammeter (red), oscilloscope (purple), and galvanometer/potentiometer (yellow). Electrical signals can be driven with a wave function generator (green). Finally, a 4 K cryostat (blue box) is available for temperature controlled experiments, and an integrating sphere (IS) is available to measure absolute quantum yields. Connections between the devices are indicated by the colored circles, and the orange lines indicate possible optical paths for measurement.

## 1.5 Synopsis

This thesis is a conglomeration of projects focused around the application of optical and electrical characterization techniques. Chapter 2 uses numerical analysis to model the results from a current-voltage (JV) scan to explore the possible routes forward towards improving tin-based solar cells. Chapter 3 uses temperature dependent photoluminescence quantum yield (PLQY) measurements in an attempt to elucidate some of the fundamental mechanisms of charge transport at work in double perovskites. Chapter 4 again uses electrical measurements in the form of maximum power point (MPP) tracking to track degradation. Section 4.1 is a continuation of the paper *Migration of cations induces reversible performance losses over day/night cycling in perovskite solar cells* by Domanski *et. al.* in which we vary the applied voltage and illumination condition during rest on various compositions to gauge the effect [105]. Section 4.2 looks at the effects of degradation under real-world conditions, exploring and quantifying reversible and irreversible degradation. Finally, Chapter 5 attempts to combine temperature dependent JV scans and photoluminescent spectra to extract material properties of highly efficient perovskite solar cells.

## **Lead free perovskites**

### **Part I**



Perovskite solar cells seem to offer a path forward for the large-scale penetration of solar panels needed to curb the world's CO<sub>2</sub> emissions, and the emissions of other pollutants, while at the same time increasing the available energy for worldwide consumption. However, traditional perovskites have a significant amount of lead in them, which presents several issues. The most pressing of these is that lead is toxic to both humans and the environment.

The lead compounds present in traditional perovskites are water soluble, meaning that when these solar cells are exposed to the environment they will not only degrade, but lead will leach into the ground contaminating the soil and water. To prevent this, a push has been made to replace lead with other elements. There have been two main routes taken in this regard. The first is to replace lead directly with tin, and the second is to replace lead with two different elements, creating a double perovskite.



## 2 Tin Perovskite

While the main attraction to tin-based perovskites is that they do not contain lead, they also offer other benefits. First, they have the possibility of smaller band gaps than lead-based ones [106]. This is due to the reduced relativistic effect of spin-orbit coupling [107]. Tin perovskites offer band gaps of down to roughly 1.25 eV compared to the 1.5 eV that lead-based perovskites can achieve. This slightly increases their limiting Shockley-Queisser efficiency from about 32% to 33% [108]. However, tin perovskites can also have very large band gaps, in excess of 3.5 eV, which also provides a wider range of tunability than lead-based ones. These macroscopic benefits, of course, have their underlying fundamental causes.

While tin perovskites have the potential to replace lead-based perovskites with these advantages, they currently face enormous issues with both efficiency and stability. There are two main causes for these issues. The first is that tin is readily oxidized from  $\text{Sn}^{2+}$  to  $\text{Sn}^{4+}$ , which can happen exogenously or endogenously. This oxidation removes the Sn from the lattice to form other compounds, creating a vacancy defect and p-doping the material. The internal causes of this oxidation are due to the thermodynamic instability of  $\text{Sn}^{2+}$  compared to  $\text{Sn}^{4+}$  at surfaces and defects, while the external factors are driven by reactions with atmospheric oxygen and water [109]. This p-doping then leads to shorter carrier lifetimes and diffusion lengths, reducing charge extraction [110, 111, 112]. These defects also facilitate dynamic behavior in these perovskites, further degrading cell performance [113].

The second cause of tin-based perovskite's issues arises because both the conduction and valence band are shifted up in energy relative to lead [114]. This causes a significant mismatch between the perovskite bands and the transport layers commonly used because they were developed for lead-based perovskites. Most notably the significant misalignment with the electron transporting layer (ETL) causes a large drop in the open-circuit voltage.

To alleviate the p-doping of tin perovskites a switch from a normal n-i-p architecture to an inverted p-i-n architecture can help. A speculated mechanism for this is that by using an inverted architecture charge generation moves from near the ETL layer to the HTL layer, reducing the extraction of electrons and increasing that of holes. This could reduce the

amount of tin oxidation, however this claim has yet to be shown concretely [88]. As discussed in Sec. 1.3.3, this also has the benefit of reducing the cost of the cell by removing the expensive processing of  $\text{TiO}_2$  in favor of cheaper transport layers.  $\text{TiO}_2$  has also been observed to adsorb oxygen, which would further contribute to the oxidation of  $\text{Sn}^{2+}$  to  $\text{Sn}^{4+}$  [115]. While using inverted architectures has indeed led to higher efficiency cells, this is at the cost of a high short-circuit current due to reduced charge extraction [116, 117].

Tin cells today are nearing efficiencies of 15% but still have a significant way to go to catch up with the progress lead-based perovskites have made [118]. While both tin- and lead-based perovskites suffer from issues of stability and dynamic behavior, these issues are much more pronounced in the tin-based cells. However, the significant benefits that tin cells could provide warrant the further investigation and development they have been garnering.

During the course of characterizing an n-i-p structured tin-based perovskite cell optimized for current density, we performed photoluminescent quantum yield (PLQY) experiments to analyze  $V_{oc}$  losses [119]. The PLQY measurements were performed on the perovskite on glass only. From the PL spectra, we took the peak position of the spectra to represent the bandgap of the material, 1.33 eV. From this we calculated the Shockley-Queisser (SQ) limit of the open-circuit voltage,  $V_{sq} = 1.08$  V, which gives an upper bound on the  $V_{oc}$  [108]. Using the absolute photoluminescent yield, we then calculated the quasi-Fermi level splitting (QFLS) of the sample,  $V_{qfls} = 0.92$  V. Taking the difference of the  $V_{sq}$  with the measured  $V_{oc}$  from  $V_{qfls}$  gives us the loss in  $V_{oc}$ ,  $\Delta V_{oc} = (1.08 - 0.92)$  V = 0.16 V. This amounts to a  $0.16/1.08 = 15\%$  loss in  $V_{oc}$  relative to the ideal. However, a JV scan of the same type of perovskite as part of a full device resulted in a  $V_{oc}$  of only 0.33, amounting to a  $\Delta V_{oc} = (1.08 - 0.33)$  V = 0.75 V, or 69% loss. Compared to lead-based perovskites, which typically see a  $V_{oc}$  loss of roughly 20%, these sorts of large losses in  $V_{oc}$  are expected in tin-based perovskites, which often see losses of roughly 50%. These are mostly due to non-radiative recombination caused by defects, both in the bulk and at the transport layer interfaces [120]. To understand the significant mismatch between the  $V_{oc}$  found from PLQY and JV we investigated further.

To carry out this investigation at a semi-quantitative level SCAPS was used [121]. By matching the experimental JV scan, we were able to obtain a base point for the device's properties. Matching was performed by gradient descent on the parameters in Table 2.1d, starting from initial values taken from literature. While other parameters were also allowed to vary, they did not change from the base value in a significant way. The only pieces of data available to perform this matching were the JV scan and PLQY results, and SCAPS can not perform PLQY results as a target for matching, leaving only the JV scan as a target. Typically other experiments, such as external quantum efficiency (EQE) or intensity dependent JV scans, would be performed allowing for a more trustworthy matching by supplying a larger target data set. Due to the large number of parameters in the model and the small target data set, consisting of the single JV scan, there is likely a range of model parameters that would fit the data. However, after allowing different sets of parameters to vary, while keeping others pinned at their original values, the model selected showed the subjectively best trade-off between



accuracy of the JV fit, and parameter values.

The comparison of the JV scan from the model and experiment are seen in Fig. 2.1a, and the model parameters are listed in Table 2.1 giving the characterization parameters in Table 2.2. Using this model as a base point, we altered specific properties of the device to explore where the most gains in device performance could be acquired.

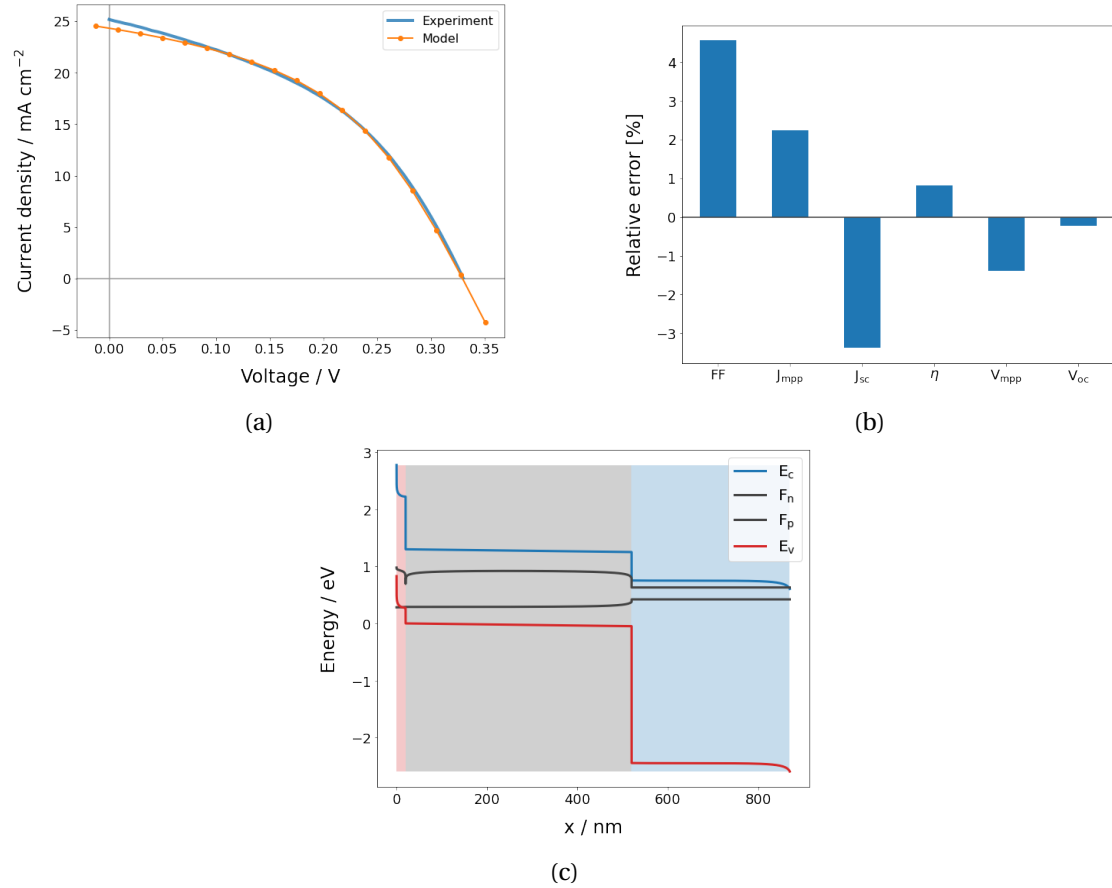


Figure 2.1 – (a) Comparison of the experimentally obtained JV curve and that produced by SCAPS varying the given parameters. (b) Relative errors of the model compared to experimental characterization parameters. (c) Band diagram at  $V_{\text{oc}}$ . Spatial parameters of the layers are indicated by the background color. Red is P3HT, black is MAFASnI<sub>3</sub>, and blue is TiO<sub>2</sub>.

Let's first examine the base model and its properties. Of note are the dopant concentrations ( $N_a$ ,  $N_d$ ) in the perovskite layer, which are equal at a value of  $1.00 \text{ E}+18 \text{ cm}^{-3}$ . As discussed above, we would expect the material to be p-doped, which is not seen. However, attempting to impose even a slight p-doping considerably decreases the match between the JV scan of the model and experiment, which we'll explore later. Because of this, the equal doping concentrations were accepted to maintain the good fit between model and experimental JV curves. Further, the effect of the absolute value of the dopant concentration was investigated, as one would not expect this to affect the model. Indeed this was the case. While varying the

	P3HT	MAFASnI <sub>3</sub>	TiO <sub>2</sub>
Thickness / nm	20	500	350
Band gap / eV	1.95	1.30	3.20
Electron affinity / eV	2.61	3.53	4.03
Relative dielectric permittivity	3.53	8.20	9.00
CB DOS / cm <sup>-3</sup>	2.20 E+18	1.00 E+18	1.00 E+18
VB DOS / cm <sup>-3</sup>	1.00 E+17	1.00 E+18	2.00 E+19
Electron thermal velocity / cm s <sup>-1</sup>	1.00 E+8	1.00 E+8	1.00 E+8
Hole thermal velocity / cm s <sup>-1</sup>	1.00 E+8	1.00 E+8	1.00 E+8
Electron mobility / cm <sup>2</sup> V <sup>-1</sup> s <sup>-1</sup>	3.80 E-4	2.66 E+1	2.00 E+1
Hole mobility / cm <sup>2</sup> V <sup>-1</sup> s <sup>-1</sup>	5.62 E-5	3.00 E+1	1.00 E+1
N <sub>d</sub> / cm <sup>-3</sup>	1.00 E+6	1.00 E+18	1.00 E+16
N <sub>a</sub> / cm <sup>-3</sup>	1.27 E+16	1.00 E+18	–
Defect density / cm <sup>-3</sup>	0	(c)	0

(a)

	P3HT/MAFASnI <sub>3</sub>	MAFASnI <sub>3</sub> /TiO <sub>2</sub>
Total Density / cm <sup>-2</sup>	4.35 E+15	2.45 E+14
Cross section / cm <sup>2</sup>	1.00 E-15	1.00 E-15
Energy level / eV	E <sub>i</sub>	E <sub>V</sub> + 0.6

(b)

Radiative recombination coefficient	6.00 E-11
Defect profile	Gauss
Defect type	Neutral
Defect density / cm <sup>-3</sup>	2.00 E+15
Defect energy level	E <sub>i</sub>
Defect characteristic energy / eV	0.10

(c)

Batch	Parameters
1	ETL and HTL interface defect density
	$\mu_e$ and $\mu_h$
	N <sub>a</sub> and N <sub>d</sub>
2	ETL electron affinity
	HTL band gap
	MAFASnI <sub>3</sub> band gap and electron affinity

(d)

Table 2.1 – SCAPS parameters of the base model. (a) Layer parameters. (b) Interface defect parameters. (c) MAFASnI<sub>3</sub> recombination model. (d) Parameters that varied during each batch of fitting.

Parameter	Measured	Model	Rel. error [%]
$V_{oc} / V$	0.33	0.33	-0.2
$J_{sc} / \text{mA cm}^{-2}$	25.17	24.3	-3.4
$V_{mpp} / V$	0.22	0.21	-1.4
$J_{mpp} / \text{mA cm}^{-2}$	16.46	16.82	2.2
FF [%]	42.87	44.5	4.6
$\eta$ [%]	3.54	3.54	0.8

Table 2.2 – Characterization parameters of the measured device and base SCAPS model. Most initial values come from the model presented in [122] with modifications from [123, 124, 125].

values of  $N_a = N_d$  from  $1.00 \text{ E}+1$  to  $1.00 \text{ E}+18$  no change in the JV curve occurred. A possible cause of the lack of p-doping is that the samples were kept in an inert atmosphere during fabrication and encapsulation, encapsulated with butane tape, and were measured fresh. Thus, they were never exposed to a significant amount of oxygen, as they would have been if left in atmosphere. This would prevent the oxidation of  $\text{Sn}^{2+}$  to  $\text{Sn}^{4+}$  keeping the material more intrinsic.

Because we only matched the model based on the JV curve, we can compare the model to the measured PLQY for comparison. The PLQY of a cell is [119]

$$\text{PLQY} = \frac{J_{\text{rad}}}{J_{\text{rad}} + J_{\text{non-rad}}} \quad (2.1)$$

where  $J_{\text{rad}}$  is the radiative recombination current and  $J_{\text{non-rad}}$  is the non-radiative recombination current. SCAPS provides information about generation and recombination currents allowing us to calculate the predicted PLQY from the model. In this model, non-radiative recombination caused by Shockley-Read-Hall (SRH) recombination is about six orders of magnitude larger than the radiative recombination across the geometric extent of the cell. This leads to essentially having zero PLQY, which unfortunately does not match the experimental value of roughly 0.2%. However, even though this mismatch occurs, we will explore this model to see what it has to tell us.

Fig. 2.1c shows the band diagram of the base simulation at  $V_{oc}$ . There are two significant features to point out. The first is the large band bending in the P3HT layer. This is caused by contact with the gold electrode and does not have a significant effect on the cells properties. The second is the bending of the quasi-Fermi levels near the perovskite-transport layer interfaces. This is a result of interfacial recombination and reduces the open-circuit voltage of the cell.

The band gap of the modeled perovskite layer is 1.30 eV which corresponds to an upper bound open-circuit voltage of 1.04 V, as found from the Shockley-Queisser limit. However a  $V_{oc}$  of only 0.33 V was recorded, meaning a voltage loss of 0.71 V, or 69% occurred, matching what was found experimentally.

From Fig. 2.1c we see that ETL alignment with the conduction band is likely the main source of voltage loss due to the large mismatch of 0.50 eV, or 38% of the band gap. The HTL also shows a significant misalignment of 0.27 eV, or 21% of the band gap. However, no band bending occurs at the HTL as it does at the ETL, pointing to the ETL as the main culprit of voltage loss. If we naively assume that the  $V_{oc}$  is limited by the conduction band of the ETL and valence band of the HTL, this reduces the potential  $V_{oc}$  from the 1.04 V found from the Shockley-Queisser limit to 0.53 V, a reduction of 51%. This points to just how important the transport layer alignment is in this model, which we will expand on later.

In this study we alter the perovskite layer thickness, band alignments, interface and bulk defects, and carrier mobilities, examining the trends in  $V_{oc}$ ,  $J_{sc}$ ,  $V_{mpp}$ ,  $J_{mpp}$ , fill factor (FF), and power conversion efficiency (PCE,  $\eta$ ). In order to save space in the figures, units for each of these is omitted, and use the canonical units shown in Table 2.3.

Table 2.3 – Units for characterization parameters.

Parameter	Unit
$V_{oc}$ , $V_{mpp}$	V
$J_{sc}$ , $J_{mpp}$	$\text{mA cm}^{-2}$
Fill factor (FF)	%
Efficiency ( $\eta$ )	%

We begin with the effect of changing the perovskite layer thickness, as seen Fig. 2.2. From the plot of  $\eta$ , we see that our base model, with a thickness of 500 nm is about 70 nm too thick from the ideal, around 430 nm. The negative correlation of  $J_{sc}$  and FF with thickness points towards mobility being an issue. Later, we will see that this is indeed the case.

Fig. 2.3 shows the effect of bulk defects on the characterization parameters. As discussed, tin-based perovskites are known to have a high defect concentration significantly caused by the oxidation of tin. Typical values are between  $10^{15}$  and  $10^{16} \text{ cm}^{-3}$ , roughly 100 times higher than that of lead-based perovskites, with the model's set to  $2 \times 10^{15}$  [116]. With these high defect concentrations, one may assume that this is a limiting factor in device performance. However, we can see that at a concentration  $10^{15} \text{ cm}^{-3}$ , we are at the boundary of saturating the effect of bulk defects. Thus, if no other parameters change, simply decreasing the bulk defect concentration will have little effect.

We now come to examine what appeared to be a major factor in the device's poor performance. Fig. 2.4 shows the effects of varying energetic level of the electron and hole transport layer (ETL/HTL) on the various characterization parameters. We will view these three types of plots through the rest of this investigation, so it is worth explaining how to read them. Fig. 2.4a shows how each of the characterization parameters varies as a function of both the ETL and HTL alignment. The red square indicates the region of the base model to use as a reference. Figs. 2.4b and 2.4c show the same data as in Fig. 2.4a as slices through each of the axes. The vertical grey lines in each of the plots indicates the base level for the parameter on the x-axis, and the horizontal grey line in the color bar indicates the base values of the axis being sliced

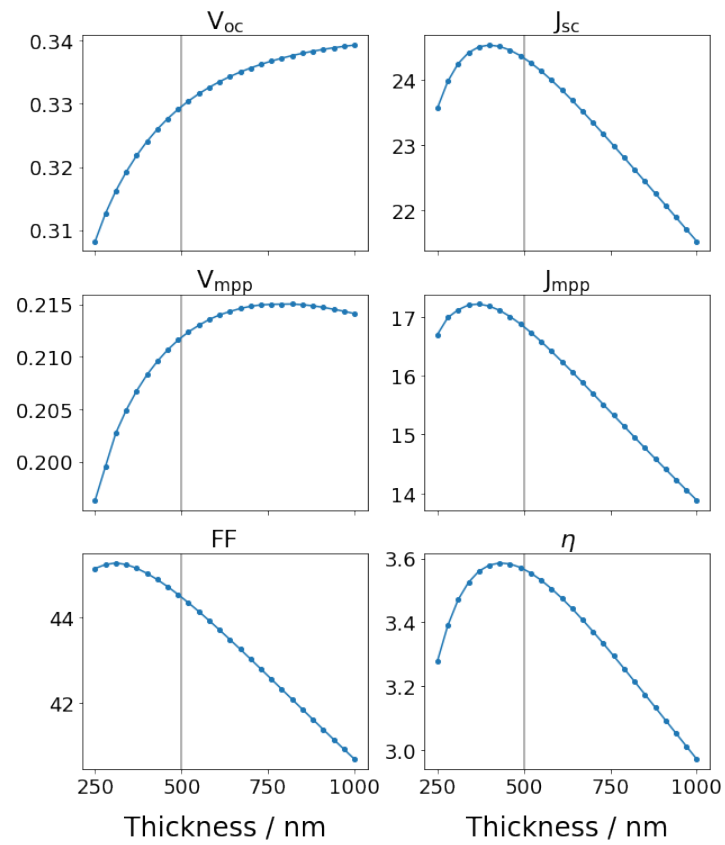


Figure 2.2 – Effect of absorber layer thickness on characterization parameters.

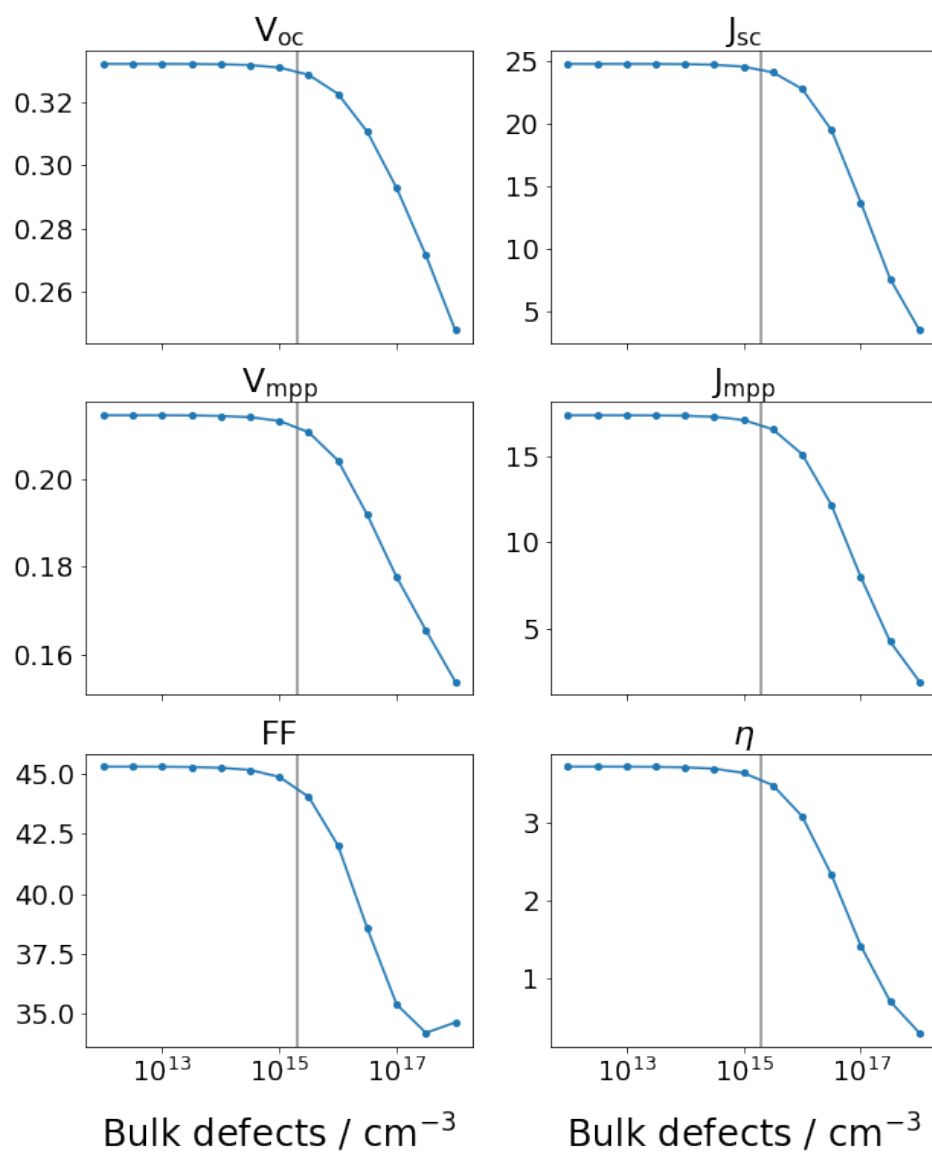


Figure 2.3 – Effect of bulk defects on characterization parameters.

across. The labels in these plots have been simplified to ETL and HTL to make the plots for the different variations more consistent. Due to this simplicity, the details of the variation are explained in the respective figure captions.

Viewing Fig. 2.4a we see a general biasing of higher values as the level of the ETL decreases. This amounts to decreasing the electron affinity of the  $\text{TiO}_2$  layer, better aligning it with the conduction band of the perovskite. This is reflected in Fig. 2.4b through the steep slopes, especially of  $\eta$  and  $V_{oc}$ . Looking at Fig. 2.4c we also see the larger impact of the ETL alignment through the more spread traces across ETL values. Note too that there is little gain in the  $J_{sc}$  to be had through transport layer alignment.

The effect of interface defects at the ETL and HTL are shown in Fig. 2.5. Here we see a dominant effect caused by the interface at the ETL. It is known that  $\text{TiO}_2$  oxidizes tin in the perovskite, causing a significant defect density. As discussed before, this is one of the reasons p-i-n architectures are preferred for tin-based solar cells.

Fig. 2.6 shows the effect of bulk mobility on the characterization parameters. While we would expect higher mobilities to generally yield better values for the characterization parameters, here we see that a lower hole mobility actually improves the efficiency and  $V_{oc}$ . Fig. 2.7 reveals why this occurs. Recombination at the ETL interface is strong enough that increasing the hole mobility leads to additional recombination at that interface. Thus, by reducing the ETL interface defects, we not only see a large improvement in the characterization parameters – just as we saw in Fig. 2.5 – but also a saturation of the effect of mobility once reaching an interface defect concentration below roughly  $10^{13} \text{ cm}^{-2}$ . While this is only an order of magnitude away from the base model value, it is three to four orders of magnitude from experimentally measured values [126]. While this shows there is a long way to go in terms of defect passivation, this is a known problem, and because there is such a high defect concentration to begin with, even slight improvements in the regime can show tremendous benefits.

One of the interesting results of this model was the lack of p-doping. Fig. 2.8 shows the effect of varying the dopant concentrations. In Fig. 2.8a there is a fairly clear line along the diagonal of each of the characterization plots that maintains a constant value. This diagonal indicates an equal doping of donors and acceptors. Notice that if  $N_d$  is larger than  $10^{16} \text{ cm}^{-3}$  the values of each parameter remains roughly constant. Fig. 2.8b shows the JV characterization parameters as a function of the ratio of the two dopant concentrations. A negative ratio indicates the material is n-doped, while a positive value indicates p-doping, and zero represents equal doping. Notice that for n-doped material there is a clear trend, especially for  $V_{oc}$  and  $V_{mpp}$ , showing that for the same dopant ratio the doping concentration has a significant effect, and this trend becomes more pronounced as the ratio approaches zero. This indicates more sensitivity to the doping concentrations as the doping moves from n-doped to intrinsic. This is explained by looking at the absolute concentration values. Let's compare, for instance, the

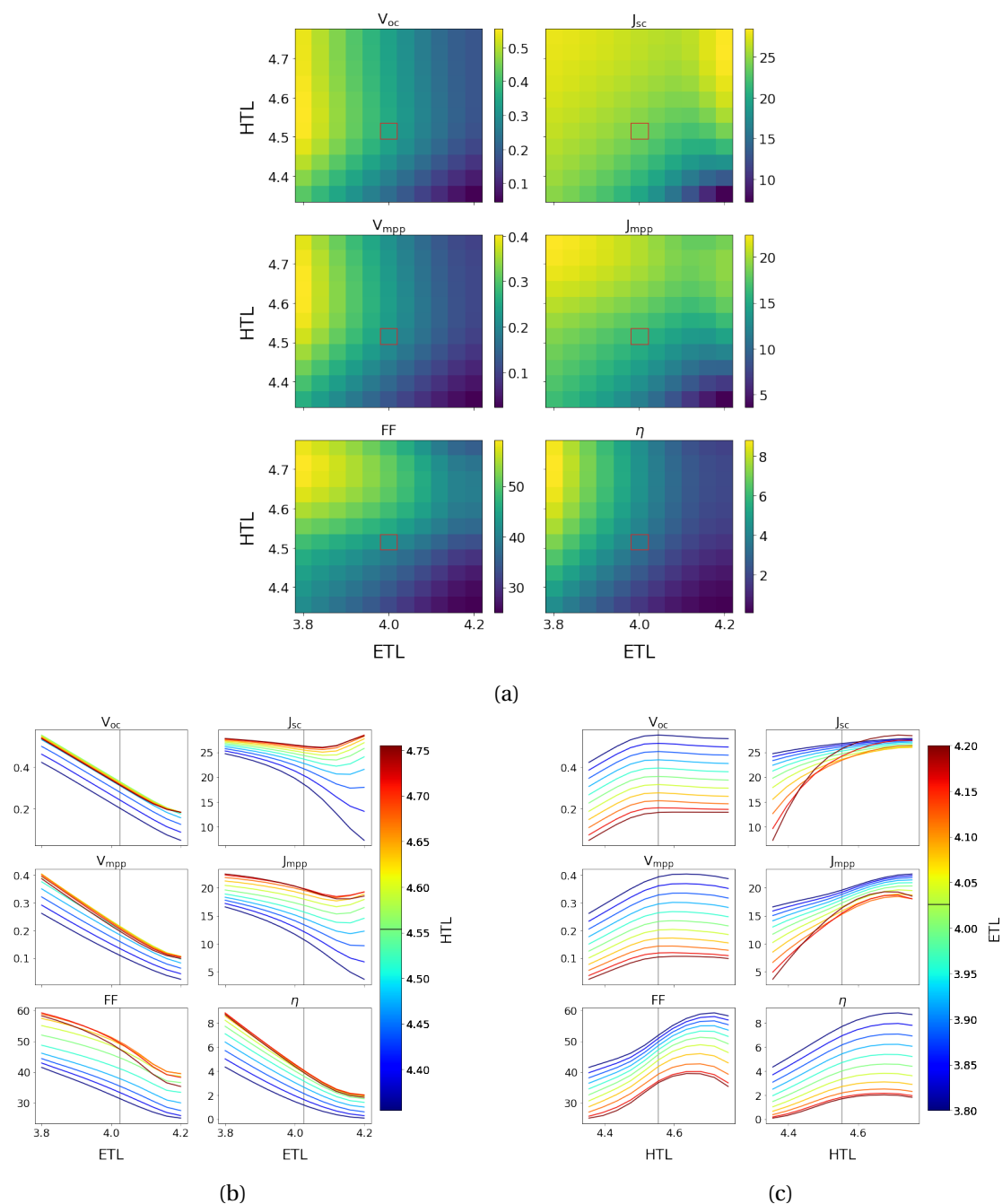


Figure 2.4 – The effect of ETL and HTL alignment on characterization parameters. ETL values are the electron affinities of the  $\text{TiO}_2$  layer, and HTL values are the ionization energy of the P3HT layer. All values are in eV. (a) Shows the effect of both parameters, while (b) slices through HTL values, and (c) slices through ETL values. The red boxes in (a) and gray lines both in the plots and on the color bar of (b) and (c) indicate the base parameter values.



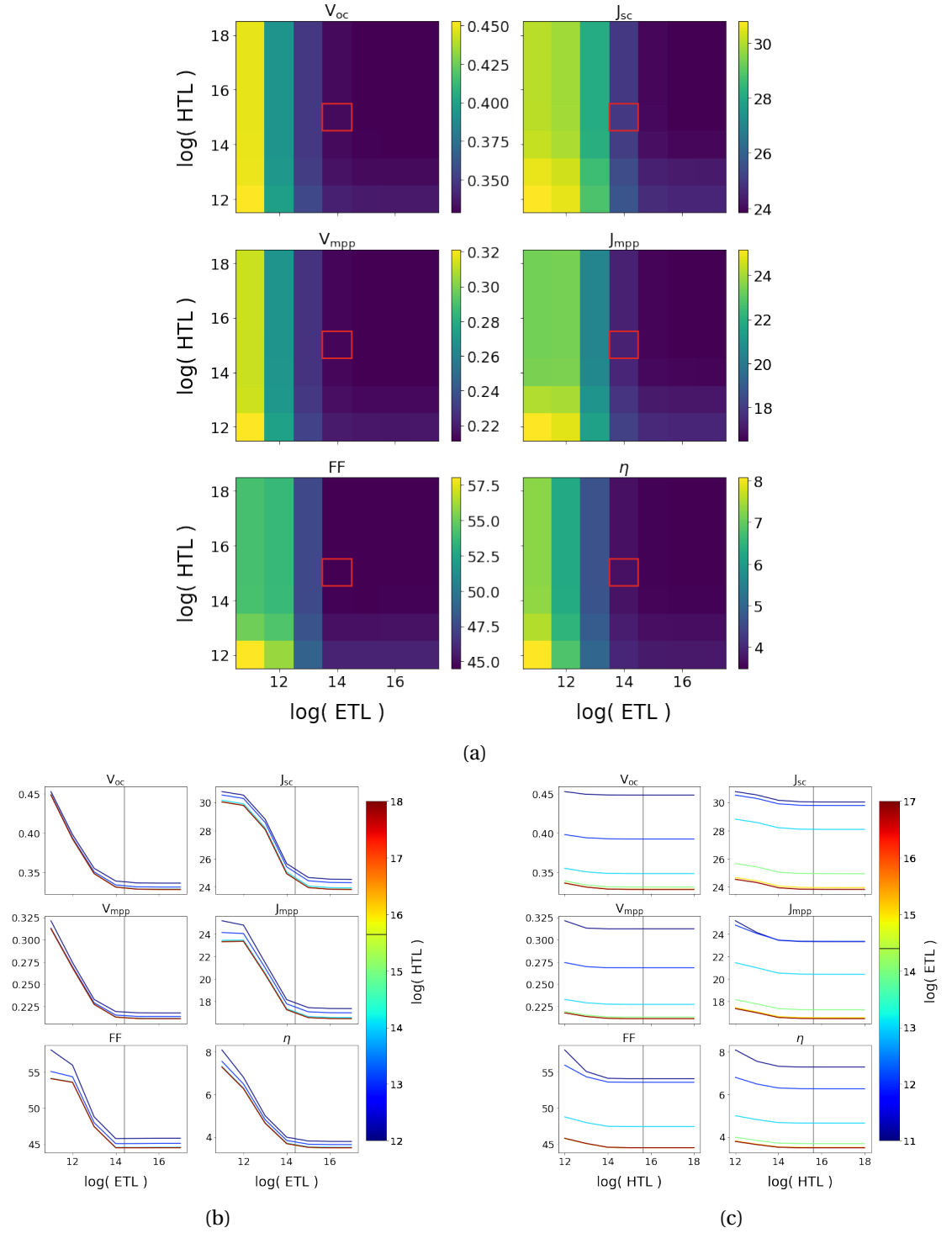


Figure 2.5 – The effect of interface defects at the HTL and ETL on characterization parameters. Values are defect density in  $\text{cm}^{-2}$  at the respective interfaces. (a) Shows the effect of both variations, while (b) slices through ETL values, and (c) through HTL values. The red boxes in (a) and gray lines both in the plots and on the color bar in (b) and (c) indicate the base parameter values.

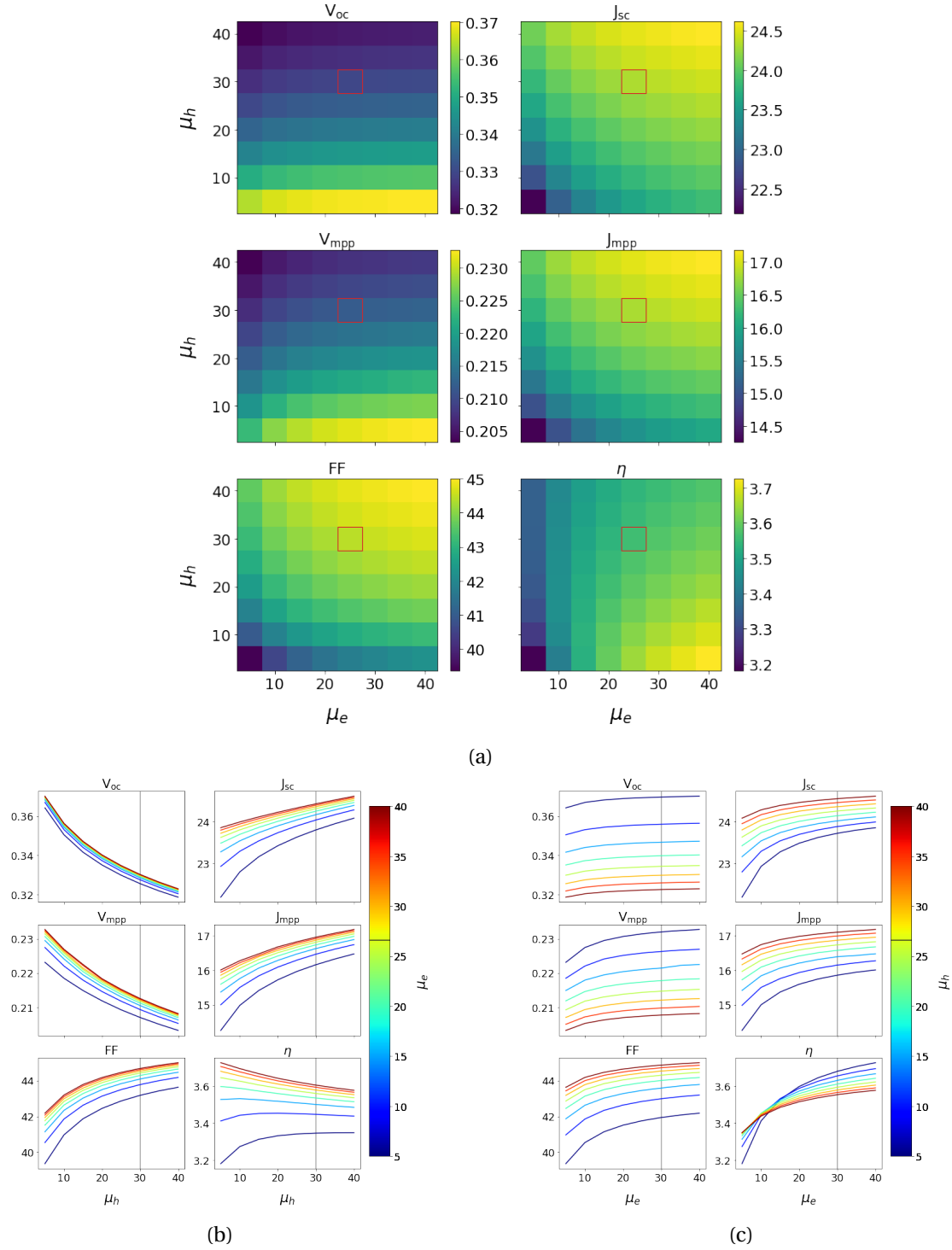


Figure 2.6 – The effect of bulk mobility of electrons and holes on characterization parameters. Axes show carrier mobility in  $\text{cm}^2 \text{V}^{-1} \text{s}^{-1}$ . (a) Shows the variation of both parameters, while (b) slices through hole mobility values, and (c) slices through electron mobility values. The red boxes in (a) and gray lines both in the plots and on the color bar of (b) and (c) indicate the base parameter values.

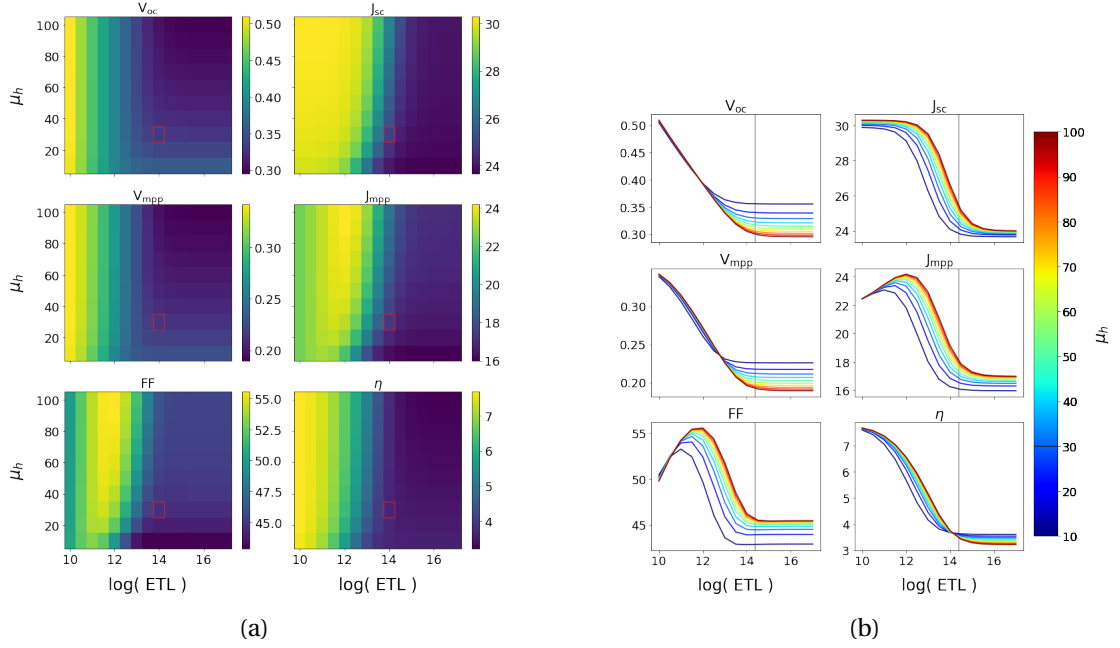


Figure 2.7 – The effect of interface defects at the ETL and hole mobility on characterization parameters. Axes show carrier mobility in  $\text{cm}^2 \text{V}^{-1} \text{s}^{-1}$  and defect concentrations in  $\text{cm}^{-3}$ . (a) Shows the variation of both parameters, while (b) slices through hole mobility values. The red boxes in (a) and gray lines both in the plots and on the color bar of (b) indicate the base parameter values.

points

$$x = (\log(N_a/N_d) = -5.0, \log(N_a) = 15), \text{ and}$$

$$y = (\log(N_a/N_d) = -0.5, \log(N_a) = 20)$$

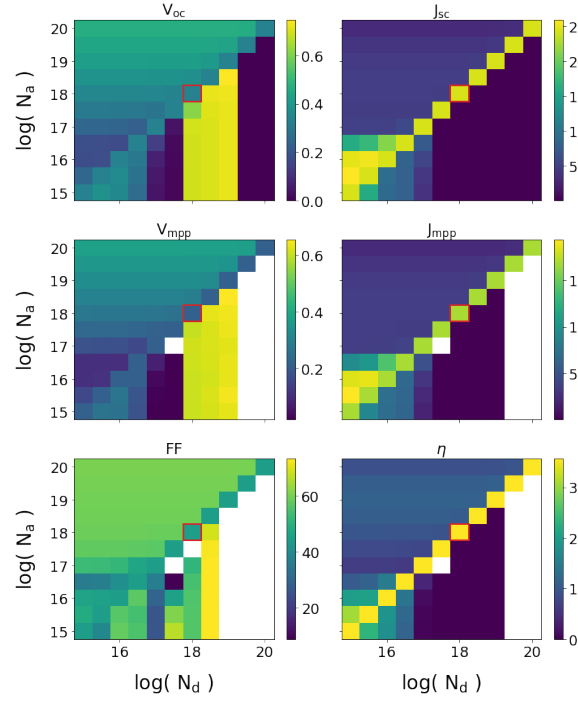
Even though the two doping concentrations have a significantly different ratio, the absolute difference between  $N_a$  and  $N_d$  for  $x$  is  $1.0 \text{ E}+20$  and for  $y$  is  $6.8 \text{ E}+19$ , almost the same. Interestingly, p-doping shows no such trend, essentially seeming chaotic in the face of doping concentration. Note also, the tight grouping of values for equal doping levels regardless of the doping concentration. This shows the detrimental effects of doping the material, at least for this model.

We now turn our attention towards the effect of optimization of each of the previously examined model parameters. We begin with the effect of removing bulk defects, seen in Fig. 2.9a. We see here no significant change between the base model and the defect free model, indicating that bulk defects do not play a significant role in this model compared to the other mechanisms. This goes counter to the previous discussion of self p-doping, pointing to a possible mismatch between this model and reality.

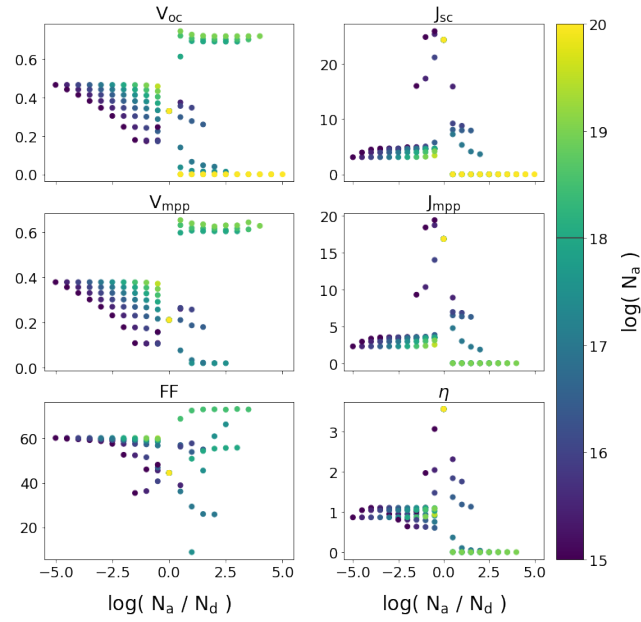
We next examine the effects of aligning the ETL and HTL with their respective perovskite band edges. Fig 2.10a shows the significant gains of better ETL alignment. With just ETL alignment the  $V_{oc}$  improves from 0.33 to 0.66 V – a 100% improvement – and the  $J_{sc}$  improves from 24.3 to 27.8  $\text{mA cm}^{-2}$  – a 14% improvement.

Optimizing the interface defects also shows a significant improvement, again pointing to the perovskite-ETL interface as the major issue in performance, as we saw in Fig. 2.5. The JV curves for optimizing the ETL and HTL interface defects – using the values previously found – as well as for the case with no defects at either interface are shown in Fig. 2.11a. This corresponds to a value of  $10^{12} \text{ cm}^{-2}$  for the ETL interface and, reducing both values from the base model by a factor the same factor of  $10^3 \text{ cm}^{-2}$ ,  $10^{11} \text{ cm}^{-2}$  for the HTL interface. Focusing on the defect free trace shows an interesting phenomenon of an S-curve. This has been shown to be caused by band bending at an interface [127, 128]. And indeed, when viewing the band diagram of the defect free model, shown in Fig. 2.12a, the bending at the ETL interface is significant. We can remove this band bending by better aligning the ETL with the perovskite conduction band. Fig. 2.12b shows the effect of this realignment. As expected from [127], the JV curves intersect as the extraction barrier resolves itself.

The effect of charge mobility optimization is seen in Fig. 2.13. Of interest is the seemingly orthogonal effects of the mobilities. Here again we see the drop in  $V_{oc}$  with an optimized hole mobility  $\mu_h$  caused by recombination at the ETL interface as discussed earlier. We also see a significant increase in  $J_{sc}$  caused by the increased charge collection. Optimizing the electron mobility  $\mu_e$  has only a minor effect on the  $J_{sc}$ , while greatly improving the  $V_{oc}$ . The dominance of  $\mu_e$  is seen when optimizing both mobilities as the character of the fully optimized JV curve matches the trend seen when optimizing only  $\mu_e$ .



(a)



(b)

Figure 2.8 – The effect of donor and acceptor concentrations on characterization parameters. (a) The effect on JV characterization parameters of varying both concentrations. The red boxes indicate the base parameter values. Concentrations are in units of  $\text{cm}^{-3}$ . (b) The effect of the dopant ratio on characterization parameters. The base value is at 0 where the doping concentrations of  $N_a$  and  $N_d$  are equal. The horizontal grey bar in the color bar indicates the base level of  $N_a$  doping.

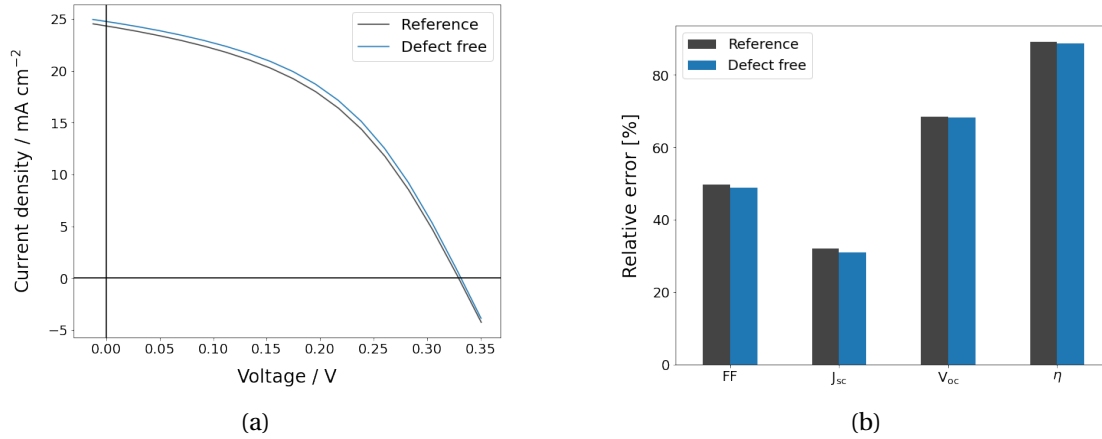


Figure 2.9 – The effect of bulk defects on JV characterization parameters. (a) JV plot of the base model compared to a model with no bulk defects. (b) Comparison of both models to the Shockley-Queisser limit of JV characterization parameters for the base model. All error values are negative.

Finally, combining all the optimized parameters shows us a more practical limit of what a tin perovskite of this sort can accomplish. The results are shown in Fig. 2.14. The gain in  $V_{oc}$  we saw from optimizing the ETL interface defects is present, and the improvement in the  $J_{sc}$  from the optimized ETL alignment, ETL interface defect density, and hole mobility is seen as well. Interestingly, while optimizing the ETL alignment, HTL interface defect density, and hole mobility independently all gave  $J_{sc}$ s of about  $30 \text{ mA cm}^{-2}$ , when they are all optimized at once, there is not much improvement over the individual optimizations. For comparison, each of these values is listed in Table 2.4.

Optimization	$J_{sc} / \text{mA cm}^{-2}$	Relative change [%]
Optimized	31.32	28.7
$\mu_h$	30.27	24.4
ETL interface defects	30.04	23.5
ETL alignment	27.81	14.3
Base model	24.33	–

Table 2.4 – Effect of different optimizations on  $J_{sc}$ . Relative change is relative to the base model.

Notice that the defect free model  $V_{oc}$  actually exceeds the SQ limit. This is concerning not only because the SQ limit should never be exceeded, even by an ideal cell, but also because the SQ limit assumes a step function absorption spectra, whereas the model uses a "square-root with exponential tails" model. This model uses an exponentially decaying density of states (DoS) into the band gap to model defect states, and a DoS that scales as the square root of the energy above the band gap, as derived for an ideal 3-dimensional crystal. Using this non-step function absorption should further lower the ideal  $V_{oc}$  from the SQ limit. The cause of this non-realistic  $V_{oc}$  is a low radiative recombination rate,  $k_r$ . Given the modeled radiative recombination rate, the model would not be in thermal equilibrium with the environment as assumed by the SQ

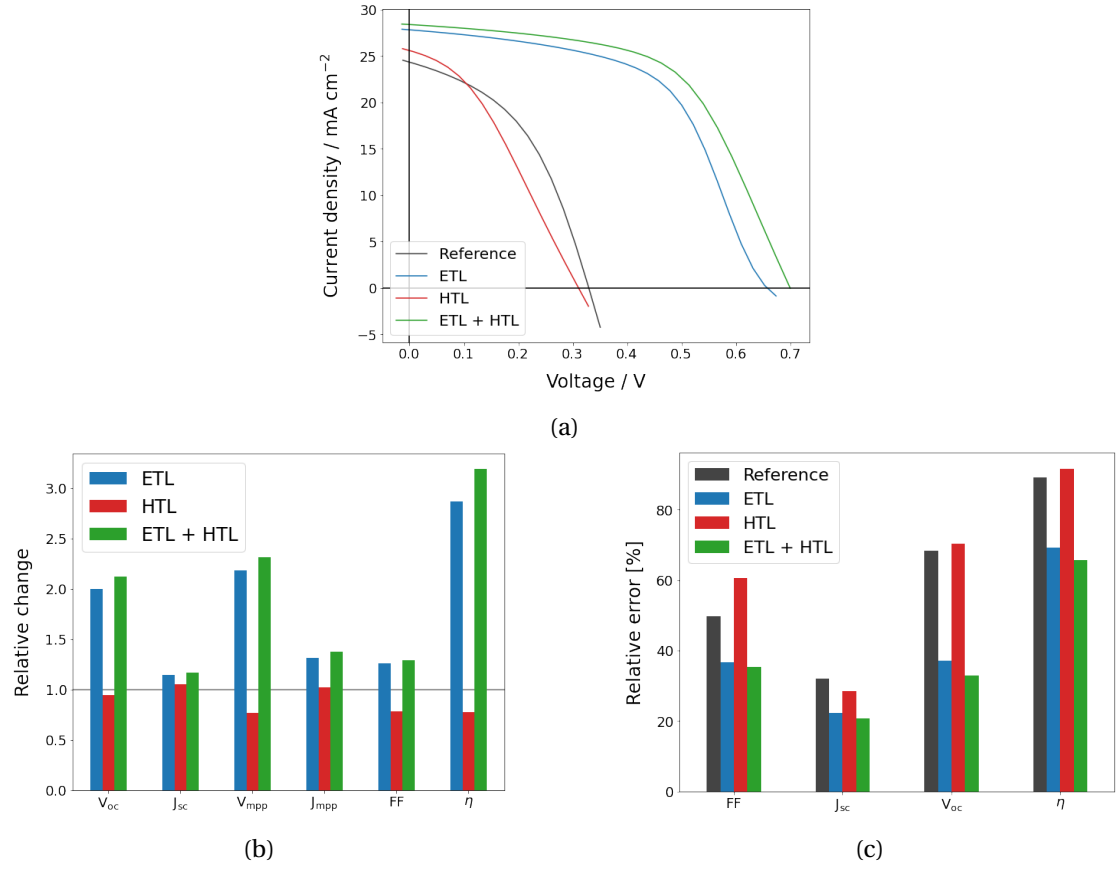


Figure 2.10 – The effect of ETL and HTL alignment on JV characterization parameters. (a) JV plots of the different models. (b) The relative change in the JV characterization parameters of each of the optimized models compared to the base model. (c) Comparison of all the models to the Shockley-Queisser limit JV characterization parameters of the base model. All errors are negative.

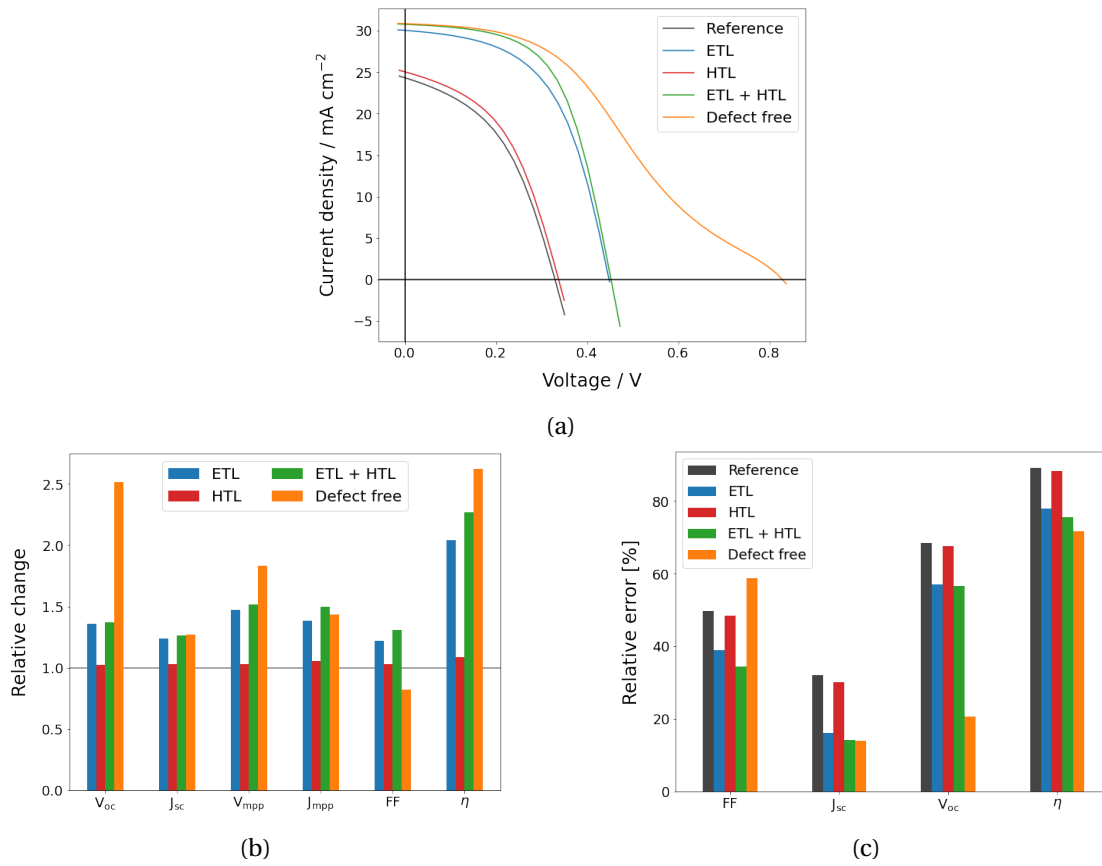


Figure 2.11 – The effect of interface defects on JV characterization parameters. (a) JV plots of the different models. (b) The relative change in the JV characterization parameters of each of the optimized models compared to the base model. (c) Comparison of all the models to the Shockley-Queisser limit JV characterization parameters of the base model. All errors are negative.



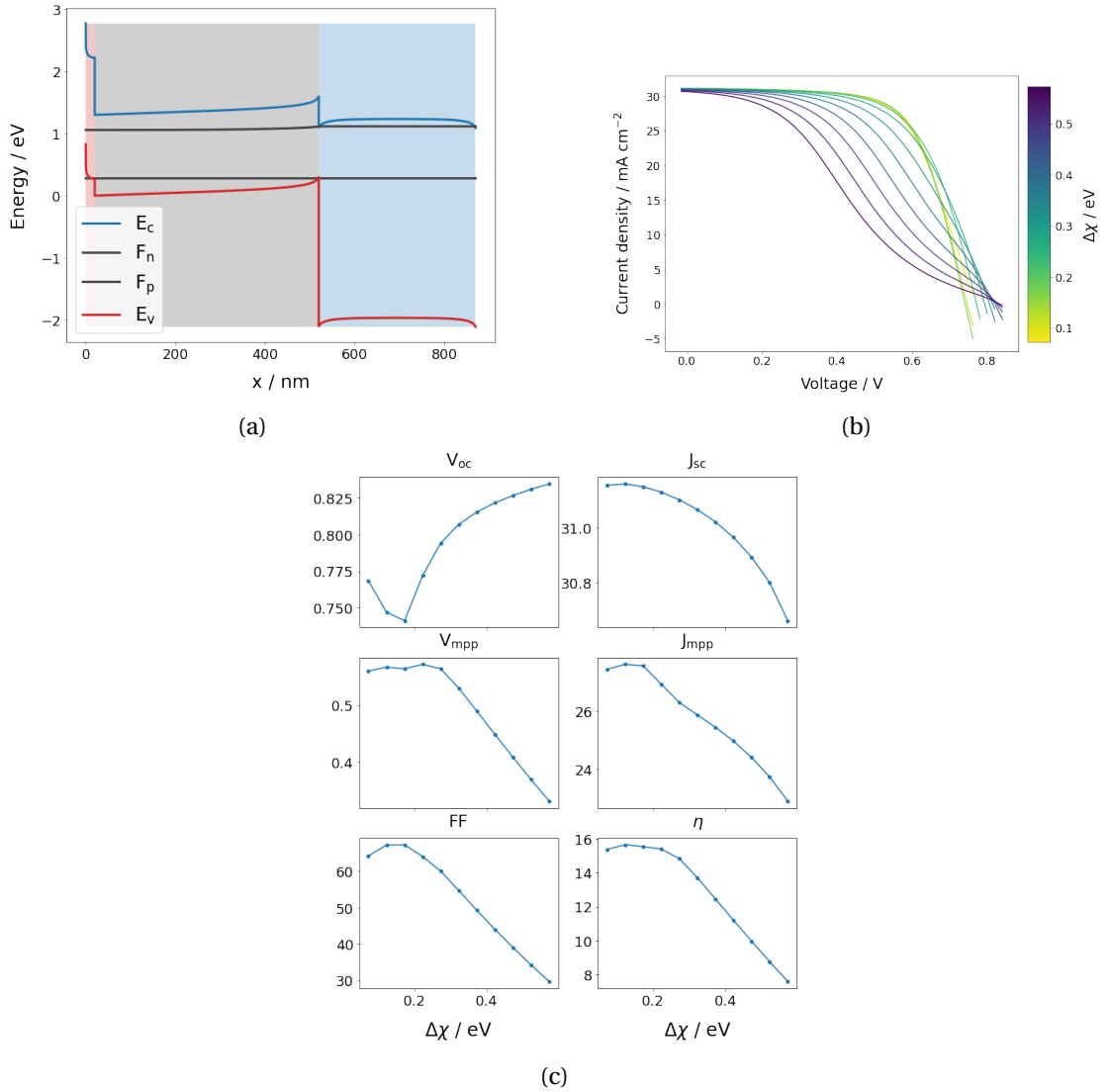


Figure 2.12 – The effect of ETL alignment on a model with no interface defects. (a) Energy diagram of the model with no interface defects. Substantial band bending is seen at the ETL interface. (b) JV plots of the model with no interface defects as the ETL energy changes relative to the conduction band of the perovskite layer. (c) The change in JV characterization parameters as the energy of the ETL changes relative to the perovskite conduction band. A positive  $\Delta\chi$  indicates the ETL electron affinity is larger than, i.e. towards the valence band of, the perovskite layer.

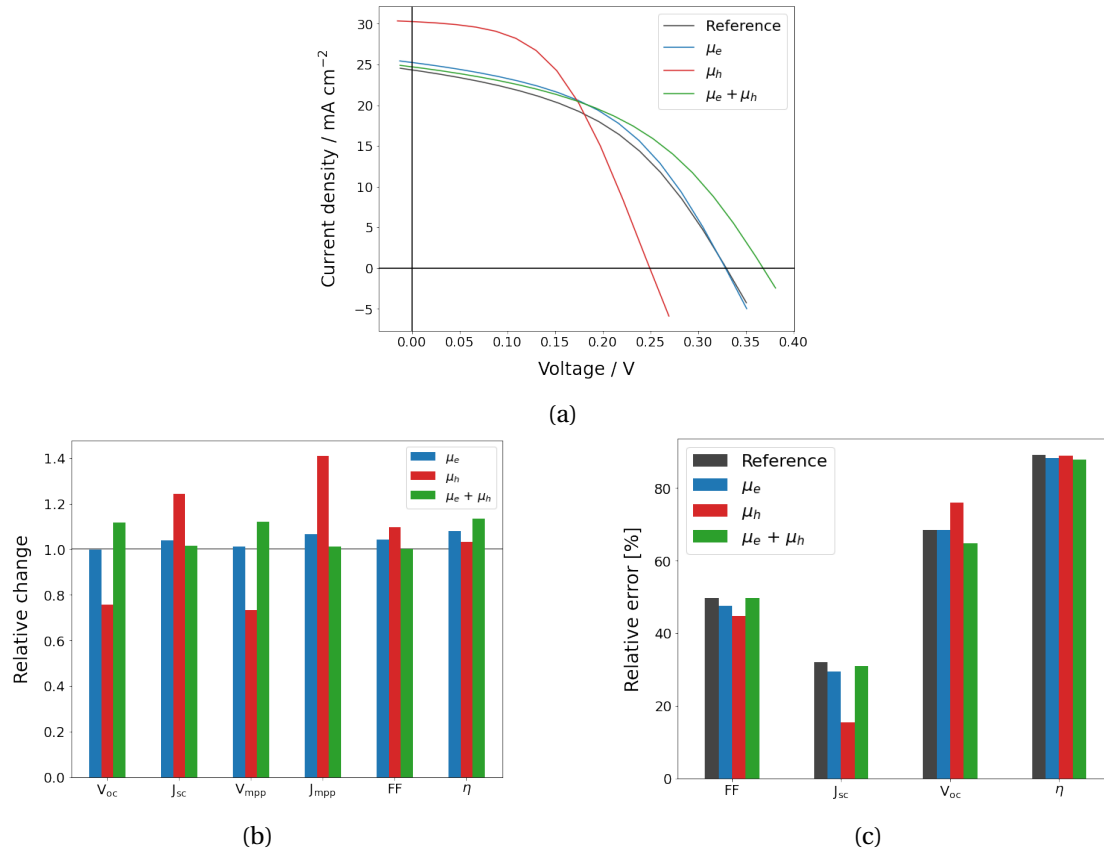


Figure 2.13 – The effect of charge mobilities on JV characterization parameters. (a) JV plots of the different models. (b) The relative change in the JV characterization parameters of each of the optimized models compared to the base model. (c) Comparison of all the models to the Shockley-Queisser limit JV characterization parameters of the base model. All errors are negative.

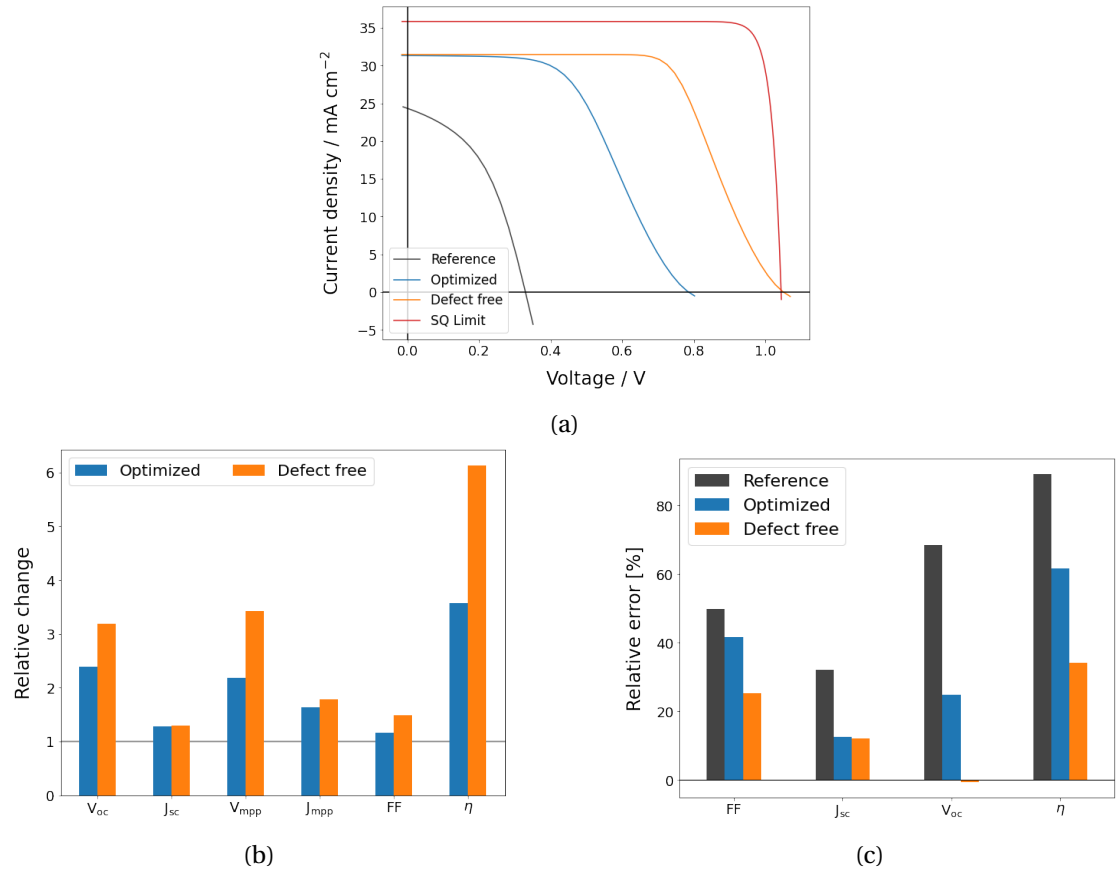


Figure 2.14 – The effect of applying all previously discussed optimizations to the base model. (a) JV plots of the different models. (b) The relative change in the JV characterization parameters of each of the optimized models compared to the base model. (c) Comparison of all the models to the Shockley-Queisser limit JV characterization parameters of the base model. All errors are negative.

limit. The effect of varying the radiative recombination rate is seen in Fig. 2.15. The variation of the radiative recombination rate, however, does not have any impact on the other explored models as non-radiative recombination is so dominant.

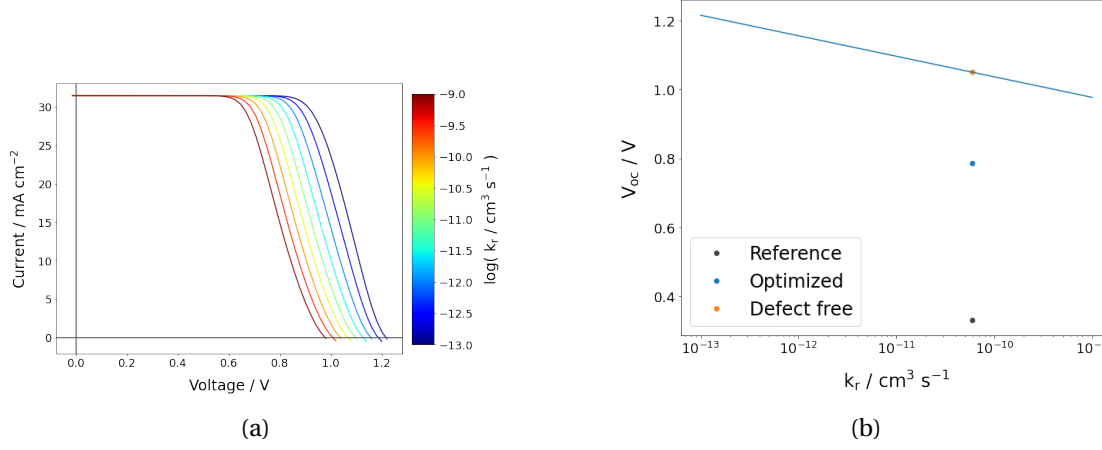


Figure 2.15 – The effect of the radiative recombination rate  $k_r$  on the (a) JV curves and (b)  $V_{oc}$ .

In examining this model of a current-optimized tin-based perovskite solar cell, we have seen the dominance of electron based parameters. The alignment of the ETL, the interface defect concentration at the ETL, and  $\mu_e$  all dominate the corresponding properties compared to those of the holes in the material.

Many studies similar to this have been performed. Abdelaziz *et. al.* modeled a FASnI<sub>3</sub> with TiO<sub>2</sub> ETL and spiro-OMeTAD HTL [122]. The simulation parameters are similar to the ones presented here with the exception of the replacement of P3HT with spiro-OMeTAD and the inclusion of an FTO layer between TiO<sub>2</sub> and the contact. The inclusion of an FTO layer in the model presented here has no significant effect, so the main differences between the results arise from the HTL. Abdelaziz *et. al.* arrived at the same conclusion as we did – that ETL alignment is the major hindrance in cell performance – with the second most important being doping of the perovskite layer. Because doping of the perovskite is difficult to control, as discussed earlier, they present ZnO and ZnSe as alternative ETL layers. While the band alignment of both these alternatives is similar to that of TiO<sub>2</sub>, they have an order of magnitude increase in the electron mobility accounting for their improved performance [122]. ZnO with an optional SnO<sub>2</sub> interlayer has shown promise as an ETL with lead-based perovskites, pointing towards its possible viability as an ETL with tin-based perovskites as well [129, 130]. The SnO<sub>2</sub> interlayer may also act to passivate the perovskite-ETL interface. And, indeed these predictions have been confirmed in real-world experiments. Using material such as SnO<sub>2</sub>, ZnS, and Nb<sub>2</sub>O<sub>5</sub> as interlayers between the perovskite layer and TiO<sub>2</sub> layers shows a significant improvement in open-circuit voltage due significantly in part by the better alignment of these materials with the perovskite conduction band [131, 132].

Through the exploration of the various properties of this n-i-p tin-based solar cell we have seen

that there are two important properties to focus on immediately. The first is the alignment of the ETL with perovskite conduction band. We saw that by optimizing this alignment alone we can move from an efficiency of 3.5% to over 8.0%. In conjunction with optimizing the alignment of the ETL, a significant focus should be turned towards passivating defects at the ETL interface. Both of these shortfalls already garner much attention. While conduction band alignment for n-i-p tin perovskites has not found so much focused research, a significant amount has been done for p-i-n architectures. And the efforts focused on defect passivation have yielded strong efficiency gains of several percentage points [88].



### 3 Double perovskite

Double perovskites offer another route towards lead-free perovskites. By replacing the B-site metal cation in the standard perovskite  $ABX_3$  with two metals we can create a perovskite like structure with a unit cell edge length twice that of the standard one. In this structure the metal cations alternate to create the crystal lattice. This results in a chemical formula of  $A_2BB'X_6$ , an image of which can be seen in Fig. 3.1. While having the option to choose two metals instead of one opens up more design choices, these choices are limited because the electronic charge of the unit cell must remain neutral. So far  $Cs_2AgBiBr_6$  has become the most popular of these formulations.

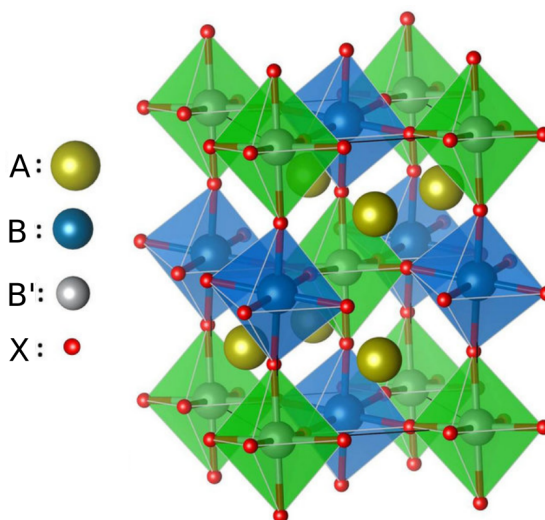


Figure 3.1 – Structure of the double perovskite  $A_2BB'X_6$  [133].

Although double perovskites have shown great promise for replacing lead and increasing environmental stability, they still have a long ways to go. Typical efficiencies for these perovskites are less than 5%. A large contributor to this low efficiency is their large band gap of around 2 eV. This places an upper bound of 23% efficiency in the Shockley-Queisser limit, a significant step down from the 33% efficiency of tin-based cells and 32% efficiency of lead-based cells. By

introducing additional metals to fill the B-site, such as antimony, this band gap can be reduced but these materials have not yet gained the popularity of their pure two metal counterparts due to an even further reduced efficiency [134].

The significant gap between the efficiencies that these perovskites currently obtain and their limiting efficiencies elicits need for an investigation into the loss mechanisms. One of the most significant differences between double perovskites and traditional perovskites is that double perovskites have an indirect band gap while traditional perovskites have a direct band gap [135]. This causes a large reduction in the absorptance of the double perovskite compared to the single perovskite. Thus, to absorb the same fraction of incident light a much thicker layer must be used. If we take these two factors – the absorption, and thickness – when computing the theoretical efficiencies we arrive at a maximum efficiency of 8% [136]. This modification, in addition to non-radiative recombination, of the Shockley-Queisser limit is called the *spectroscopic limited maximum efficiency* (SLME) [137].

This leads to the second major cause of this material's low efficiency – defects. Pure double perovskites have two things working against them. First, owing to having two metals, there is an inherent disorder present in the crystal when the metals do not perfectly alternate. This is shown in Figs 3.2a and 3.2b. This disorder modifies the band gap. For  $\text{Cs}_2\text{AgBiBr}_6$  a reduction of 1.9 to 0.44 eV occurs when moving from a fully ordered crystal to a fully disordered one [135]. Using two different metal cations can also lead to another intrinsic defect because they are coordinated by the same halide atom. If this halide is missing, leaving behind a positively charged vacancy defect, the two metals can form a covalent bond. A visualization of this is shown in Figs 3.2c and 3.2d. This creates a deep energy defect and results in a high non-radiative recombination rate [138]. Finally, defects may be introduced extrinsically. Double perovskites often require high fabrication temperatures and are very sensitive to any contaminants. This makes it difficult to fabricate pure double perovskites in the first place [136]. Combined, these defects result in a low carrier lifetime [139].

The final cause of these materials' low efficiencies is their somewhat poor electronic properties. The main culprit behind this is their poor charge mobility.  $\text{Cs}_2\text{AgBiBr}_6$  has charge mobilities that are an order of magnitude lower than those found in standard  $\text{MAPbI}_3$  perovskites. This is caused by a heavy carrier mass induced by strong charge coupling to the lattice via polar phonons [140]. This compounds the effect of the reduced absorption from the indirect band gap and the low carrier lifetimes from the defects. Because the absorption coefficient of the material is low one would like to have a thick absorber layer. Counter to this though, the short charge diffusion lengths drive one to have a thin layer to increase charge extraction. Thus, a balance of these two competing drives must be acquired to maximize efficiency.

To better understand the internal charge dynamics of these materials we can measure their radiative recombination properties. This gives an insight into the strength of the recombination mechanisms at work. To measure this photoluminescent quantum yield (PLQY) is used. PLQY is an experiment that reveals directly the radiative recombination occurring in a



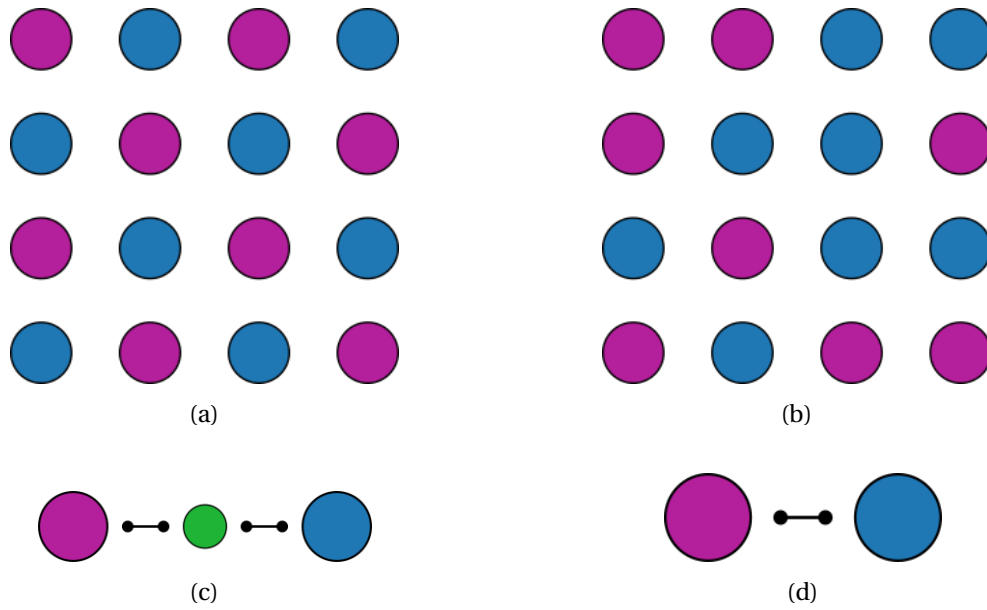


Figure 3.2 – (a, b) Demonstration (a) order and (b) disorder with the alternating B cation metals. (c, d) (c) Because both metals are coordinated with the same halide atom (green), if (d) the halide is not present the metals can form a covalent bond with each other.

material. Indirectly, then, it also reveals the amount of non-radiative recombination. Using this information can tell us about the quasi-Fermi level splitting in the material which then gives information about the voltage loss. By varying the cell parameters, such as known concentrations of defects, transport layers, or composition, we can also deduce the properties of the interaction between the perovskite and these different parameters. This yields information about interface recombination, charge transfer into the transport layers, and photon recycling [141].

Ultimately, PLQY requires only two measurements to calculate: the photon flux of the excitation source and of the photoluminescent (PL) spectra. However, many steps must be carried out before this final calculation in order to calibrate the raw signal. First, seven measurements are taken. There are two relevant types of measurements, those of the laser, indicated with an  $L$ , and those of the sample, indicated with a  $P$ . To take these measurements a band pass filter is used for the laser, and a long pass filter is used for the sample. In an integrating sphere two "no sample" measurements are taken, one  $L$  and one  $P$  indicated by a subscript  $a$ , to determine background signal. Then a "free space" measurement of the sample is taken outside of the integrating sphere to be used as a reference. Finally, four measurements are taken with the sample in the integrating sphere. Two with the sample out of the beam path, called out-of-beam and indicated by a subscript  $b$ , are taken, one  $L$  and one  $P$ . And similarly with the sample in the beam path, called in-beam and indicated by a subscript  $c$ .

From this raw data, the initial signals are calibrated to account for the spectrometer's sensitivity. Then a background correction is made using the no sample signals,  $P'_{b,c} = P_{b,c} - P_a$ . Using

the calibrated and corrected data, the absolute photon flux is calculated for each signal using a known absolute spectrum as a reference. Finally the PLQY is calculated by integrating the spectra [142].

$$A = 1 - L_c/L_b$$

$$\text{PLQY} = \frac{P'_c - (1 - A)P'_b}{L_a \cdot A}$$

where  $A$  is the absorption, taken by comparing the in-beam and out-of-beam laser signals, and each variable represents the integrated spectra of the corresponding measurement. For these samples  $P'_b$  is negligible compared to  $P'_c$ , and the absorption values are relatively high, hence the correction factor given by the absorption term is negligible. This will come into play later because this makes the PLQY calculation linear in  $P'_c$ , the in-beam sample signal.

The samples under our investigation are  $\text{Cs}_2\text{AgBiBr}_6$  double perovskites with varying transport layers in an n-i-p architecture. For ETLs either no ETL or  $\text{TiO}_2$  was used. For HTLs, no HTL, spiro-OMeTAD, or P3HT was used. For convenience I will refer to these as (ETL, HTL) from here on out – e.g. the sample with  $\text{TiO}_2$  as the ETL and P3HT as the HTL would be ( $\text{TiO}_2$ , P3HT). An example of the PLQY spectra can be seen in Fig. 3.3. The PLQYs for each combination of ETL/HTL were then computed as described above both before (pre) temperature cycling and after (post). The results of these calculations for illumination at 9.6 suns are seen in Fig. 3.4. The results for 3.8 and 19.2 suns are similar to those for 9.6.

While we would expect the PLQY of the sample with no transport layers to be the highest, due to reduced non-radiative recombination pathways introduced by the transport layers, we instead see that the sample with  $\text{TiO}_2$  as the ETL and no HTL shows the highest PLQY by a significant amount. This inconsistency may arise from two sources. First, from previous experiments these samples have shown to have a large inter-sample variability. Therefore it could be that the ( $\text{TiO}_2$ , None) sample was simply "better" than the (None, None) sample. Second, due to the low PLQY of the samples, valid PLQY measurements could not be measured below 3.8 suns. Due to how the calculations of the PLQY are done, the ratio of the integrated laser signal to the integrated PL signal of the sample introduces some error into the calculation. This error is proportional to  $L_c/P_c$ . Because the  $P_c$  values are small for these samples compared to the  $L_c$  values, this error is large, which could also affect the results. Regardless of the cause of this inconsistency, it points towards us not being able to compare between samples in a valid way. However, we can still examine the trends within each sample.

After characterizing each sample's PLQY, we ran a temperature dependent PL experiment. Samples were placed in a cryostat and the temperature was cycled from low to high stopping at constant temperature intervals for measurements. Unfortunately, poor thermal coupling between the sample holder and the sample led to a large temperature difference between those recorded and the actual sample temperature. To compensate for this the measured temperatures were calibrated as discussed in Appendix A. At each set temperature the system

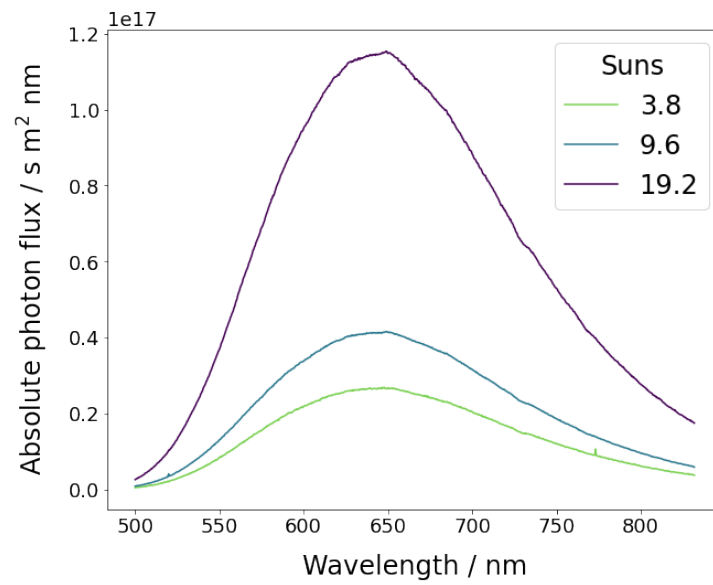


Figure 3.3 – Example spectra used in the PLQY calculations.

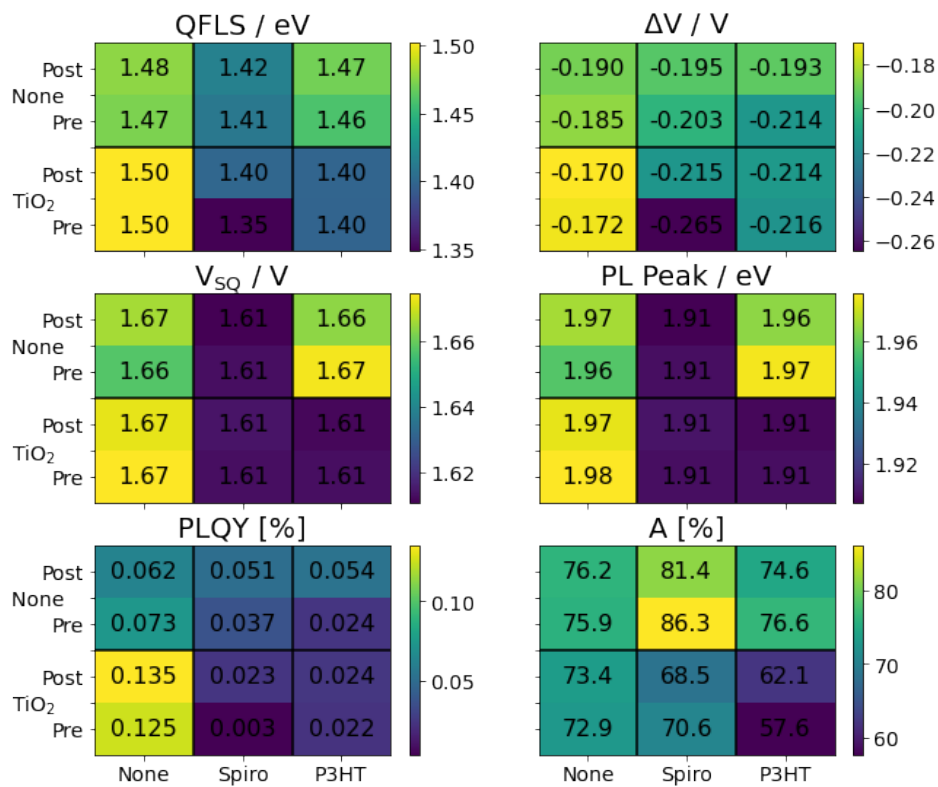


Figure 3.4 – PLQY parameters for each combination of ETL and HTL, split by pre and post temperature cycling. QFLS is quasi-Fermi level splitting,  $\Delta V$  is the calculated voltage loss,  $V_{SQ}$  is the Shockley-Queisser limit assuming the PL Peak represents the band gap, PL Peak is the peak position of the PL spectra, PLQY is the photoluminescence quantum yield, and A is absorption.

stabilized for 30 minutes after which multiple PL spectra were taken at different incident powers. Between each PL measurement the sample was allowed to rest in dark for 30 seconds, turning the laser off before the next measurement.

Examples of the raw PL spectra are seen in Fig. 3.5. In Fig. 3.5b, notice the shift of the double peak as the temperature changes, with the suppression of the low energy peak as the temperature cools. Fig. 3.5c shows the normalized PL spectra of all of the samples before cooling, and at the lowest temperature. The similarity between the spectra before cooling is an indication that the differing ETLs and HTLs have not affected the perovskite bulk. However the shape of the spectra differ greatly at 107 K, which is unexpected. Because the HTL was in contact with the thermal couple, this could be partly caused by the different thermal transport properties of the HTLs.

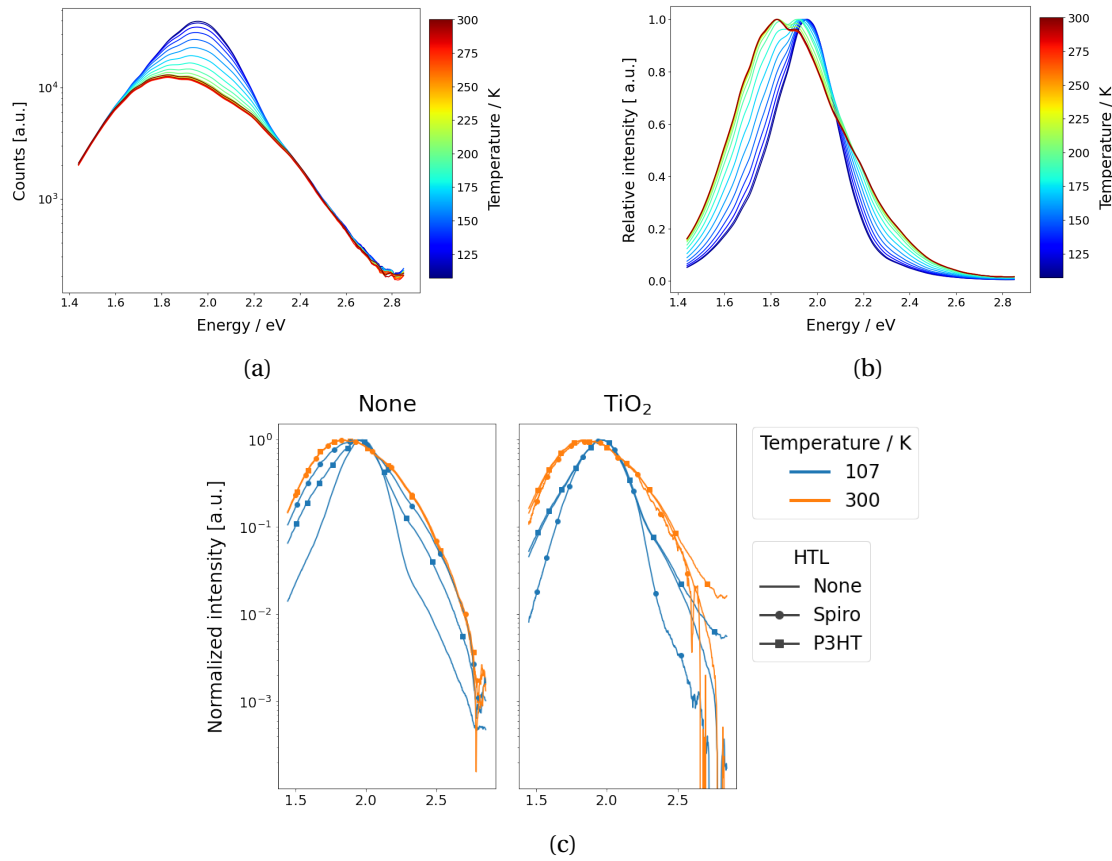


Figure 3.5 – Example of the (a) raw and (b) normalized PL spectra at various temperatures. (c) Comparison of the normalized PL spectra for all the samples.

Fig. 3.6 shows an example of two of the reference PL - PLQY plots. Here we see that the two PLQY spectra do not show a consistent trend as the power varies. i.e. Fig. 3.6a shows a negative correlation of PLQY with power while Fig. 3.6b shows a positive correlation, and other samples show no correlation. This could again be a result of the issues previously discussed with measuring the PLQY of these samples.

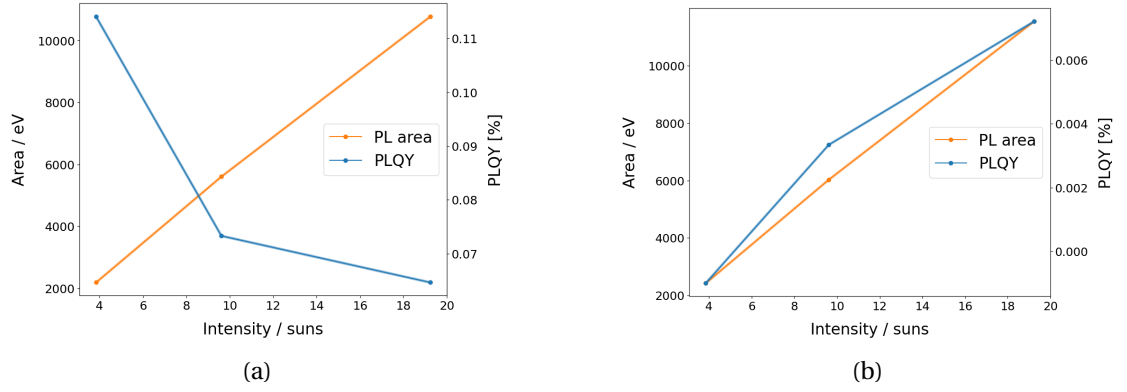


Figure 3.6 – Example of two reference PL and PLQY calculations used to calculate the PLQY at various temperatures. While the integrated area showed consistent trends of growing with the incident power as expected, the PLQY showed no such trend with respect to incident power.

To calculate the temperature dependent PLQY we used the PLQY measurements taken before the cycling as a reference. As mentioned previously, because the absorption factor in the PLQY calculation for these samples is negligible, the PLQY is linear with the in-beam sample spectra. Thus, to find the temperature dependent PLQY we can take an initial PL spectra of the sample in the cryostat and equate it to the calculated PLQY. Then as the temperature changes we can scale the PLQY by the same factor as the integrated spectrum compared to the reference. We assume that other parameters, such as the band gap and absorption of the material, do not change significantly with temperature and therefore do not affect the PLQY calculation by influencing, for instance, the sample's absorption spectrum.

$$\text{PLQY}_{\text{ref}} \propto \int I_{\text{ref}}(\epsilon) d\epsilon$$

$$\text{PLQY}(T) = \text{PLQY}_{\text{ref}} \frac{\int I_T(\epsilon) d\epsilon}{\int I_{\text{ref}}(\epsilon) d\epsilon}$$

where  $\text{PLQY}_{\text{ref}}$  and  $I_{\text{ref}}$  are the reference spectra taken before the temperature cycling,  $T$  is the temperature,  $I_T$  is the PL spectra taken at temperature  $T$ , and integrals are taken over the entirety of the spectrum. An example of the results from this calculation are shown in Fig. 3.7.

Fig. 3.7 shows the results for a single sample, and Fig. 3.8 shows the results for all the samples from this PLQY calculation. While the general shape of the curves appears sigmoidal, they are not. Fig. 3.9 shows an example sigmoid curve viewed in both linear and log scales for comparison. Comparing the log scale plot of the actual sigmoid in Fig. 3.9 to those in Fig. 3.8b it becomes clear that the calculated data is not a true sigmoid. However, fitting a sigmoid to the curves does yield an accurate fit, even in the log scale, as seen in Fig. 3.7b.

$$\text{PLQY}(T; a, T_0, T_a, b) = \frac{a}{1 + \exp\left(\frac{T - T_0}{T_a}\right)} + b$$

for fit parameters  $a$ ,  $T_0$ ,  $T_a$ , and  $b$  at temperature  $T$ .  $a$  represents the magnitude of the change,  $T_0$  the center point,  $T_a$  the slowness of the transition, and  $b$  the vertical translation.

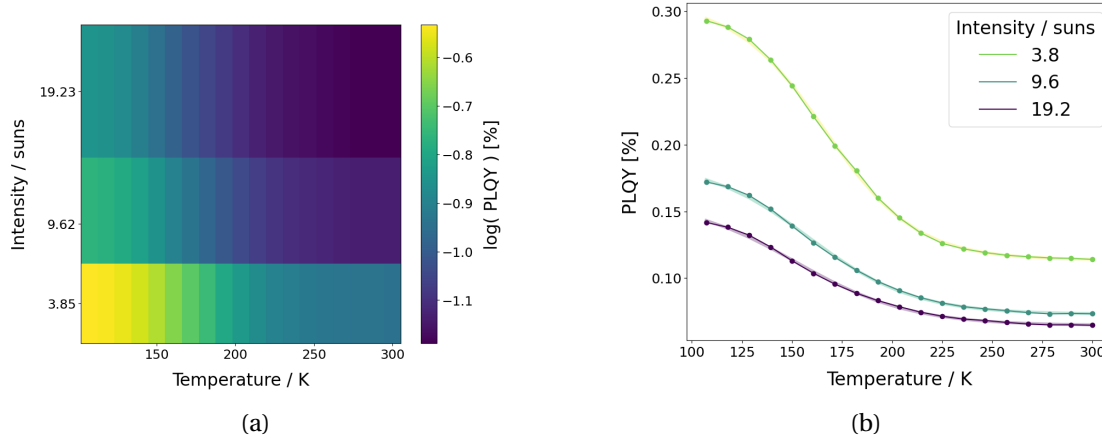


Figure 3.7 – Plots showing the calculated PLQY at various temperatures and incident powers. (a) Shows the PLQY against both temperature and incident power. (b) Shows the same data sliced along the incident power axis. The thin opaque lines are the measured data and the broader transparent lines are the sigmoid fits.

Figs 3.11 and 3.10 show the fit values for  $T_0$  and  $T_a$  for each sample. In Fig. 3.11, you'll notice that the Spiro column is an outlier for every value, thus Fig. 3.10 shows the same data with the Spiro data removed for easier comparison. However, even with the Spiro data removed, there is still not a consistent trend in any of the fit parameters.

By adding the transport layers we would have expected the PLQY to decrease with the efficacy of the transport layer as the transport layer provides mechanisms for non-radiative recombination. These mechanisms consist of charge transport into the transport layer, as well as through non-radiative recombination facilitated by the interfacial defects [139]. As discussed before, we would have expected to have seen this effect in the original PLQY measurements, but did not. We also would have expected to see this show up in the temperature dependent PLQY trends. The energy levels of  $\text{Cs}_2\text{AgBiBr}_6$ ,  $\text{TiO}_2$ , spiro-OMeTAD, and P3HT are shown in Fig. 3.12. The precise values for each of these varies slightly in literature, however those shown are a valid representation [143, 144, 145].

A cause of the sigmoid shape for the PLQY curves could be due to some saturation effect. Zelewski *et. al.* have proposed that the broad emission spectra of  $\text{Cs}_2\text{AgBiBr}_6$  is caused by a combination of the Franck-Condon effect and color centers [146]. If this is the case then it could be that these effects lose their dominance at low temperatures to other mechanisms.

What is interesting though, is that it is not only the PLQY that shows a sigmoid shape with temperature. Fig. 3.13 shows the sigmoid fits for the peak position, center of mass, and full width at half maximum (FWHM) for one of the samples, but all the samples show similar trends. These characterization parameters represent the shape of the PL spectrum, as opposed

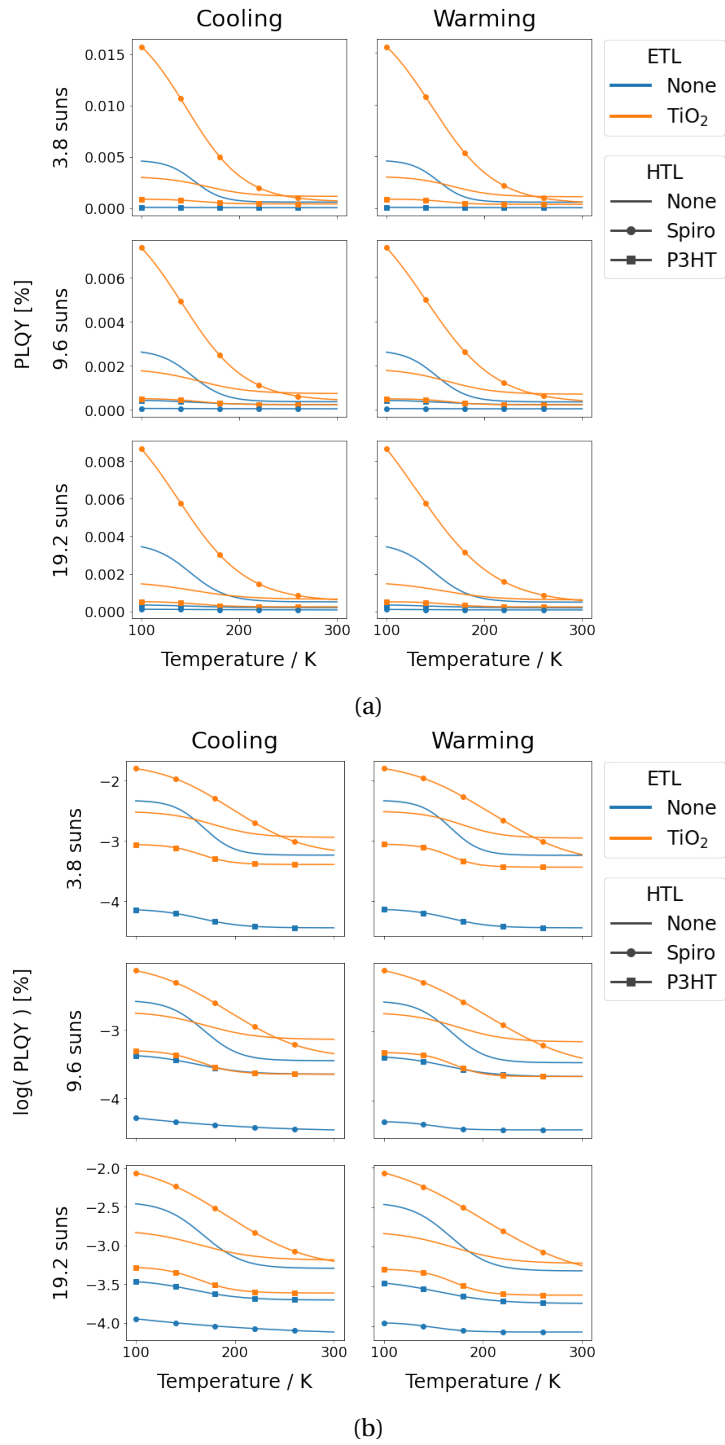


Figure 3.8 – Calculated PLQY for all samples, at all incident powers, both warming and cooling in (a) linear and (b) log scale.

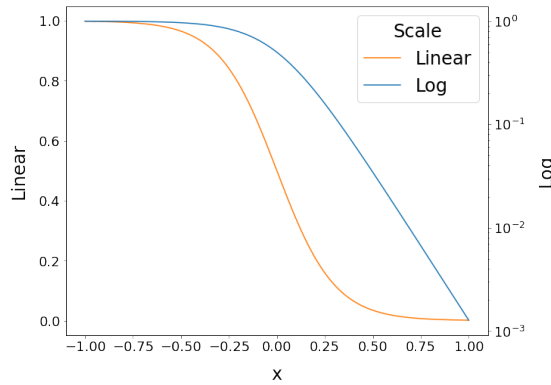


Figure 3.9 – Example of a sigmoid curve in linear and log scales.

to the PLQY which only represents the intensity of the spectrum. So, while we can explain the saturation of the PLQY with the competition between different recombination mechanisms, these parameters can not be explained in this way. An explanation for this may again trace its origin to the thermal conductivity between the sample holder and the sample.

Schade *et. al.* performed a similar experiment, finding that the integrated PL forms a Gaussian like shape, with mean  $\sim 140$  K and standard deviation  $\sim 20$  K [147]. They attribute this phenomenon to the combination of reduced non-radiative recombination and a phase transition that occurs at 122 K. As the temperature decreases, non-radiative trapping decreases as well, increasing the integrated intensity. Then, the phase transition causes a significant increase in the band gap and crystal strain. The strain introduces electronic defects within the crystal which again reduces the PL yield. If we view our results as the high temperature half of the Gaussian observed by Schade, then we can also attribute the increase in PLQY to a reduction in non-radiative recombination. However, the observed shape of the curve in our measurements would have a mean at  $\sim 100$  K and a standard deviation of  $\sim 75$  K, a significant difference from the findings of Schade. It is likely that these differences stem from the difficulties of measuring the cell's temperature.

In this study, an attempt to measure the mechanisms of various ETL and HTL materials was made. By scaling temperature dependent PL measurements to match a room temperature PLQY measurement, we were able to calculate the temperature dependent PLQY. However, no trends appeared across the sample variations as would have been expected. It is hypothesized that this is caused by a large inter-sample variability. A trend did appear within each sample though, a sigmoidal shape appeared for the standard PL characteristics. This trend was also observed by Schade *et. al.* however the parameters of their measurements differ significantly from the ones obtained here. This was likely caused by inaccuracies in the temperature measurements of our samples.



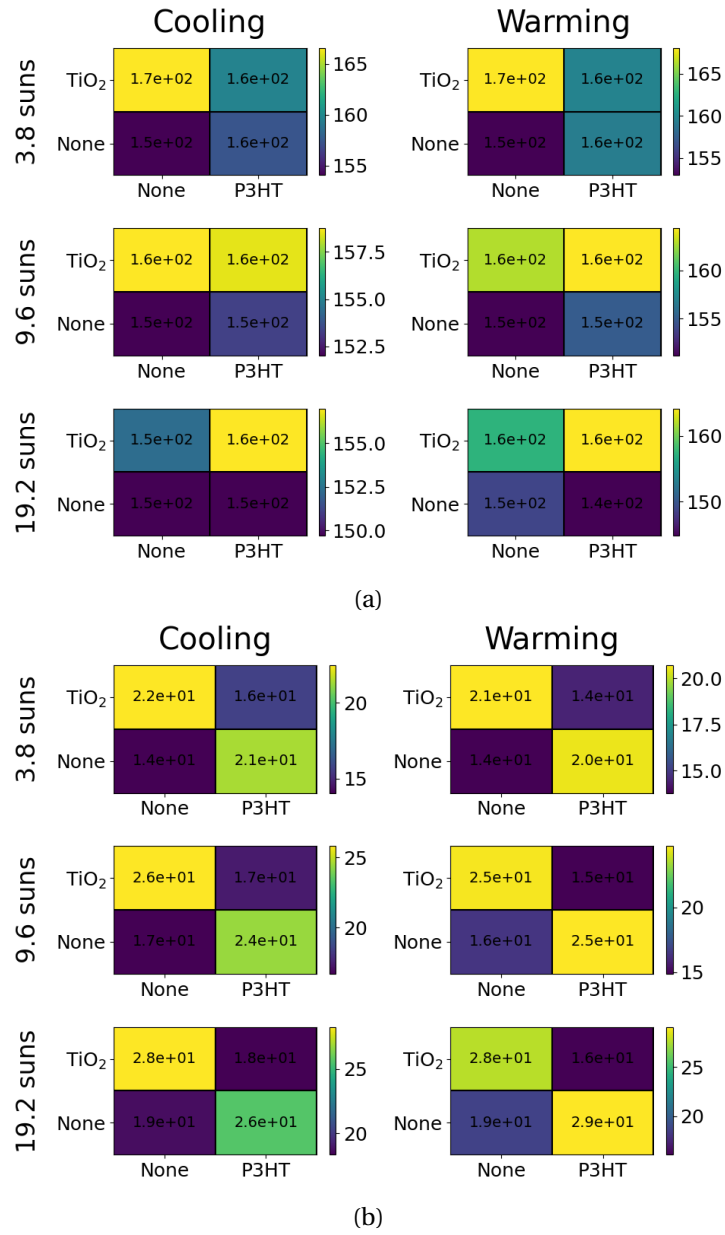


Figure 3.10 – Sigmoid fit parameters for samples without spiro-OMeTAD. (a) Shows  $T_0$ , and (b) shows  $T_a$ .

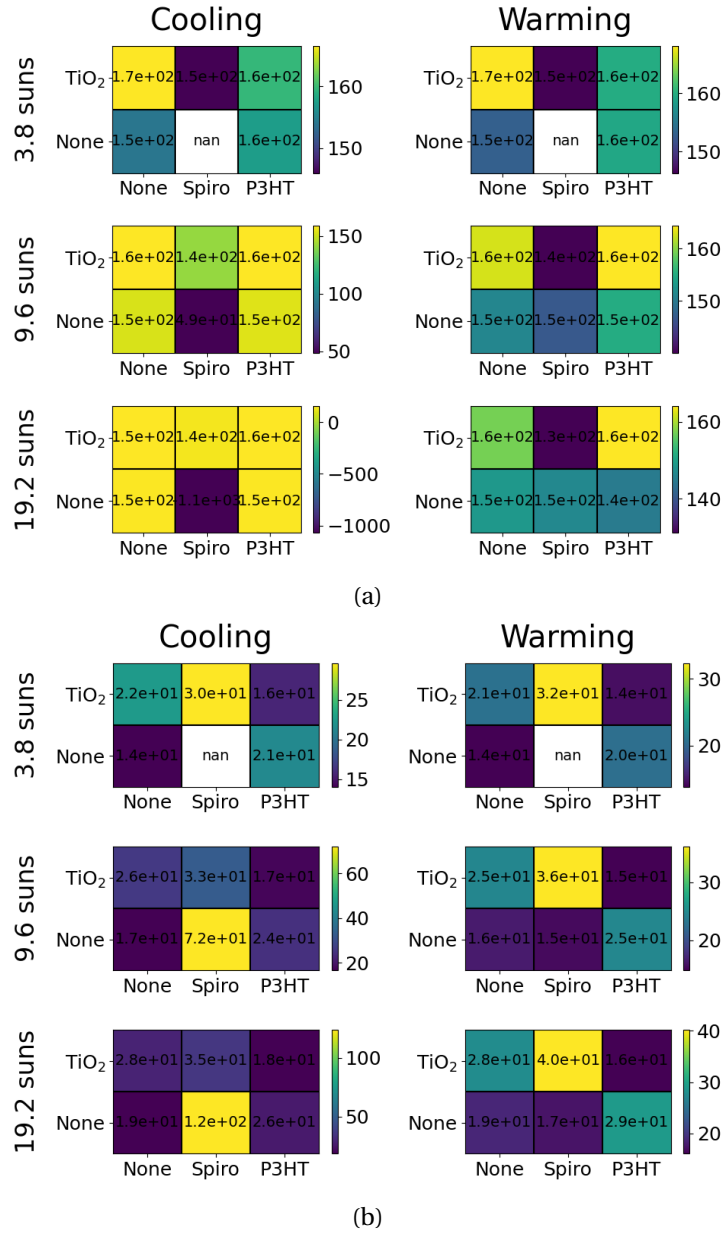


Figure 3.11 – Sigmoid fit parameters for each sample. (a) Shows  $T_0$ , and (b) shows  $T_a$ .

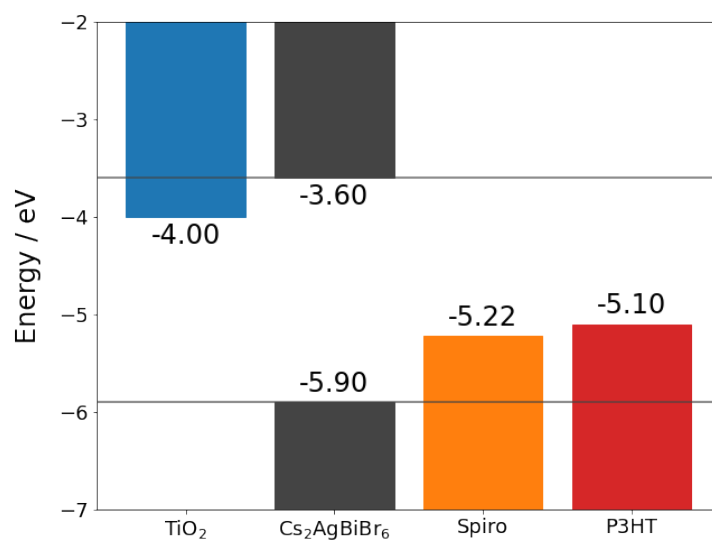


Figure 3.12 – Energy levels of Cs<sub>2</sub>AgBiBr<sub>6</sub>, TiO<sub>2</sub>, spiro-OMeTAD, and P3HT, showing their alignment.

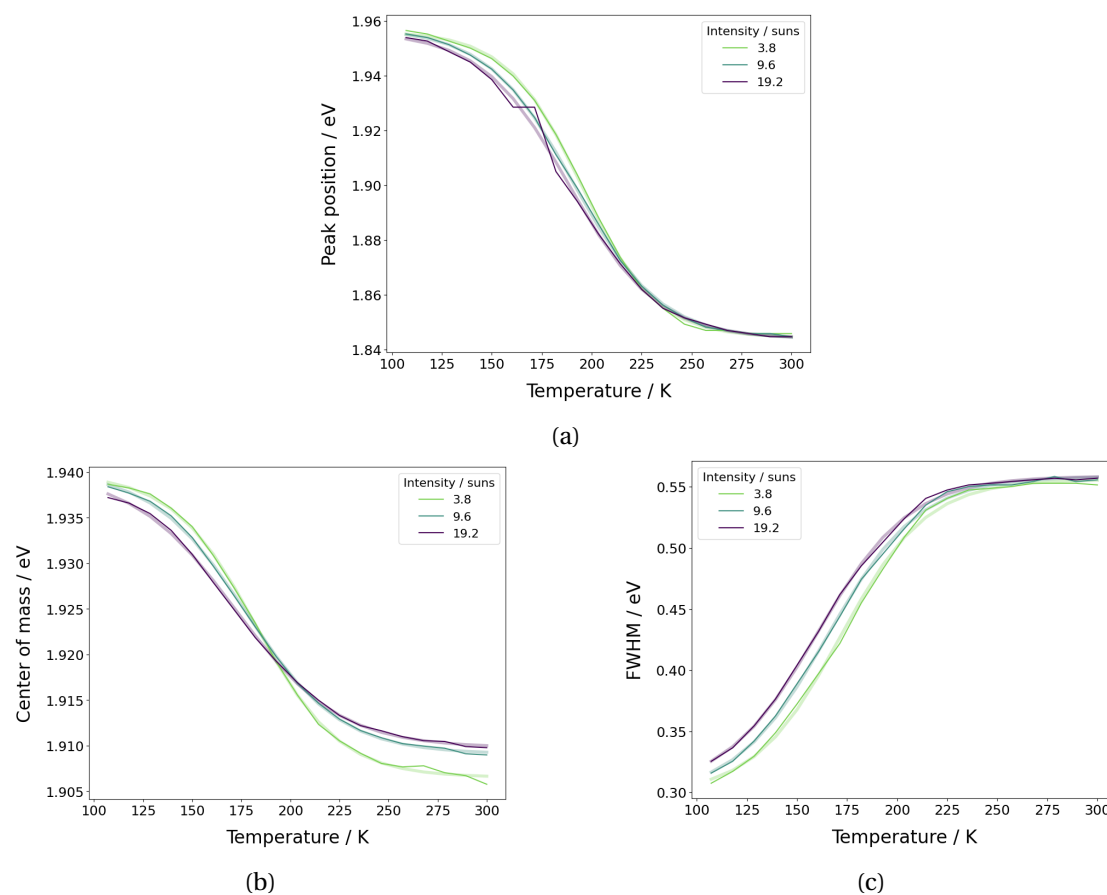


Figure 3.13 – Example sigmoid fits for the (a) peak position, (b) center of mass, and (c) full width at half maximum. The thin opaque lines are the measured data and the broader transparent lines are the sigmoid fits.

# Physics Part II



While significant progress has been made towards bringing perovskite solar cells to market, there is still a long way to go. In order to bridge this gap we must continue to improve our knowledge on the fundamental processes at work in these materials. By doing so we can engineer solutions to those effects that are detrimental and enhance those that are beneficial.

In particular, perovskites have proven to be an incredibly complex physical system to understand. This is partly due to the wide range of materials the term *perovskite* covers, but there are also more fundamental reasons this has been a challenge. During the modern boom of the semiconductor industry, heavily centered around Bell labs in the 1950's, fairly simple materials were used. Silicon, being the most popular semiconductor still to this date, proved to be governed, at a high level at least, by fairly simple equations. In many ways, silicon and other traditional semiconductors, such as gallium arsenide, are fairly near an ideal material when compared to modern organic and hybrid semiconductors, perovskites includes. This new generation of materials offers many promising functions to move technology forward, however disentangling the underlying mechanisms and physics that govern their behavior has proven quite the difficult task.





## 4 Reversible degradation and ionic movement

The complex behavior of perovskite solar cells (PSCs) is one of the largest barriers towards their commercialization. One of these limiting behaviors is the dynamic nature of their efficiency. The most apparent form this shows up in is reversible degradation. After a cell degrades it can be left to rest in the dark and recover a significant amount of its efficiency [105]. Investigations into the cause of this reversible degradation have revealed several mechanisms that may be at work.

The first of these mechanisms is the formation of meta-stable deep energy traps under illumination [148]. These traps are induced by a strong coupling between the free charges and the crystal via polarons facilitated by the ionic nature of the crystal. Because these polarons are created by free carriers excited by photoillumination, when the light source is removed the polarons relax, removing the additional trap states in the material, returning it to its original state. This mechanism operates on the time-scale of seconds and accounts for a large portion of the reversible degradation.

A second mechanism that could cause this reversible behavior is light induced phase segregation [149]. When exposed to light, the halides in mixed halide perovskites –  $\text{MAPbI}_{(1-x)}\text{Br}_x$ , for instance – become mobile due to a photo-weakening of the hydrogen bonds that stabilize them in the structure. During their migration iodide is able to stabilize the photogenerated holes, resulting in the formation of iodide rich nanocrystals. However, when left in the dark the photogenerated holes are no longer present, and the enthalpy driven phase segregation becomes dominated by entropic forces, remixing the crystal to its original state. This mechanism operates on the time-scale of minutes.

Finally, another long time-scale mechanism contributing to the reversible nature of perovskite degradation could be ion migration [150]. As we have seen, the halide X-site ion is mobile in the perovskite crystal, which can lead to phase segregation. These ions and their vacancy defects can also be driven by electric fields though [105, 151]. This creates an accumulation of the ions at the opposing transport layers – i.e. negative ions migrate towards the hole transport layer, and vice versa – creating a Debye layer. This results in increased charge recombination

at these interfaces. When the electric field is removed, these ions are able to resettle into the crystal structure, dissipating the Debye layers. This happens on the time-scale of several minutes, and does not capture the long-term degradation behavior observed in measured devices. To account for this, we consider that it is not only the halides that are mobile, but that the A-site cations are as well. The cations moves 100 times more slowly than the halides, which can account for the long-term reversible degradation that occurs on the time-scale of an hour.

## 4.1 Ionic movement and reversible degradation

As we have seen, it is known that both halide and A-site ion migration plays a role in reversible degradation of perovskites, however the full extent of this effect has not yet been fully investigated. The cycling experiments performed by Domanski *et. al.* showed that the degradation caused by these mobile ions can be almost fully reversed by allowing the device to rest in the dark at open circuit voltage [105]. This leaves open the question, though, of whether the device's recovery is due to the the absence of illumination or the applied voltage. By controlling the voltage at which the devices rest we were able to provide more direct evidence that the applied voltage is indeed responsible for the ion migration causing reversible degradation. By varying both the cation and anion composition of the cells, we have also been able to observe the magnitude and sensitivity of this effect.

Similar to Domanski's experiment, our cells are held at a constant temperature in an inert atmosphere, and undergo multiple cycles of maximum power point (MPP) tracking. Unlike Domanski's experiment, though, we hold our cells at a fixed applied voltage between each MPP tracking period. The hold voltages are calculated from the  $V_{mpp}$  and  $V_{oc}$  of the initial JV scan. This is visualized in Fig. 4.1. The order in which the ten hold voltages were applied was randomized as to not introduce a systematic bias. Each MPP tracking period lasted for 30 minutes followed by a 30 minutes hold voltage period. Because the initial MPP tracking period for each voltage, i.e. cycle 0, does not have a hold voltage period preceding it the data is disregarded. After completing five cycles at the given hold voltage, the cell is allowed to rest in the dark with no applied bias for twice the time the experiment took, 12 hours. In addition to the MPP and hold voltage cycles, JV scans were taken before and after each hold voltage experiment. In order to try to separate the effect of applied voltage and illumination on cell recovery, two kinds of experiments were performed within this experimental structure. The first turned the illumination off during the hold voltage period, while the second kept the illumination on throughout the entire hold voltage experiment. During the rest period, though, the light was still turned off.

An example of the full data collected from a single device is shown in Fig. 4.2. There are several things to notice here. The first is that as the voltage increases from  $-0.5 V_{mpp}$  to  $V_{oc}$ , the characteristic of the curve during the MPP tracking periods changes. This transition is highlighted in Fig. 4.3, and an example of these two types of characteristics is shown in Fig.

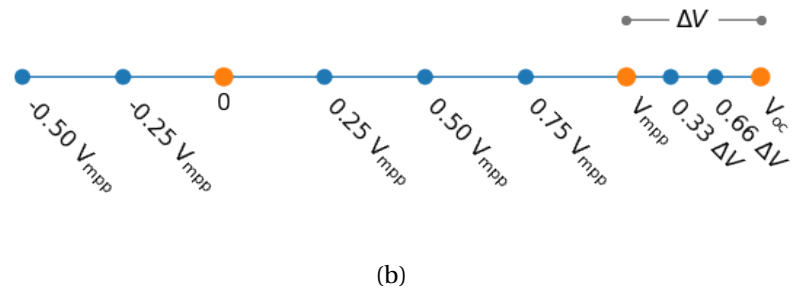
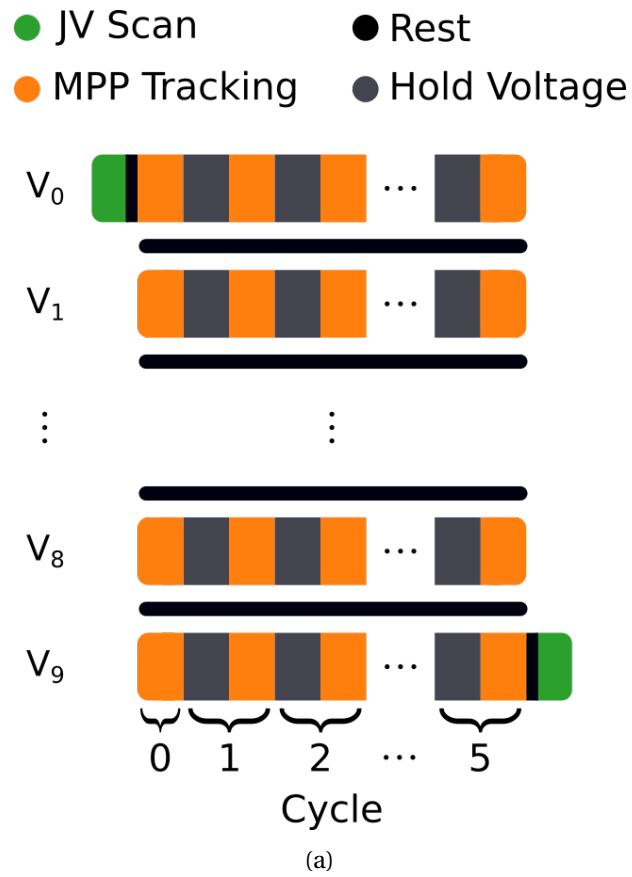


Figure 4.1 – Design of the experiment. (a) Visualization of the MPP tracking and hold voltage cycling. (b) The hold voltages.

4.3. The type of characteristic at  $-0.5 V_{\text{mpp}}$  will be called *amelioration* and the characteristic at  $V_{\text{oc}}$  will be called *degradation*. A clear example of each of these is seen in Fig. 4.4 The second thing to notice is that at hold voltage  $V_{\text{oc}}$  the cell consumes power during the hold voltage periods even though the light is turned off. The main source of this is because the values of the hold voltage are set from the initial JV scan in light. Because the dark  $V_{\text{oc}}$  is less than the light  $V_{\text{oc}}$  this hold voltage drives the cell as a diode in forward bias. Also, as the experiment proceeds, the cell's JV characteristic changes and the original  $V_{\text{oc}}$  may no longer align with the cell's actual  $V_{\text{oc}}$ . The final thing to note is that the cells' performance does not show significant degradation throughout the experiment. This is verified through the JV scans before and after each hold voltage experiment. An example of these scans is shown in Fig. 4.5.

We have seen that there are multiple degradation mechanisms at play which act at varying time scales. To capture these different time scales we use a two-term exponential function

$$P(t) = P_0 + P_1(1 - e^{-t/\tau_1}) + P_2(1 - e^{-t/\tau_2}) \quad (4.1)$$

where the first exponential term models the fast dynamics of the system and the second exponential models the slow dynamics. An example of these fits is seen in Fig. 4.6.

Fig. 4.7 shows an example of how the hold voltage affects the fit parameters. Cycle 0 is not evaluated because there is no hold voltage period that precedes it. There are several things to notice here. The first is that the characteristic of the curves is consistent throughout the cycles, again indicating that no irreversible degradation is occurring throughout the experiment. This means that we do not have to evaluate the parameters on a cycle-by-cycle basis for this data. For other data we will encounter later this will not be the case, and the cycle will have to be taken into account. Next, we can see that the characteristic times match well with the degradation mechanisms discussed before, with a fast dynamic on the time scale of seconds, and a slow dynamic on the time-scale of hours. Looking at the correlation of the parameters with hold voltage we notice that there is a high correlation for  $P_0$  and  $P_1$ , and a low correlation for  $P_2$ ,  $\tau_1$ , and  $\tau_2$ . The typical values for these correlations are given in Table 4.1 and visualized in Fig. 4.8. The values of  $r^2$  indicate that only the initial power and the magnitude of the fast degradation mechanism are affected by the hold voltage. It makes sense that the magnitude of the slow degradation component is not as correlated with the hold voltage as its dynamics are not transient. Therefore, they should be more affected by the voltage of the cell during MPP tracking than what happened to the cell during the hold period. It also makes sense that the  $\tau$  parameters are not affected by the hold voltage because when switching from the hold voltage to the MPP tracking the voltage is returned to the previous  $V_{\text{mpp}}$  which remains roughly constant. This means the electric field across the cell is roughly the same, and the dynamics of the charge movement should be the same, resulting in a low correlation between the two.

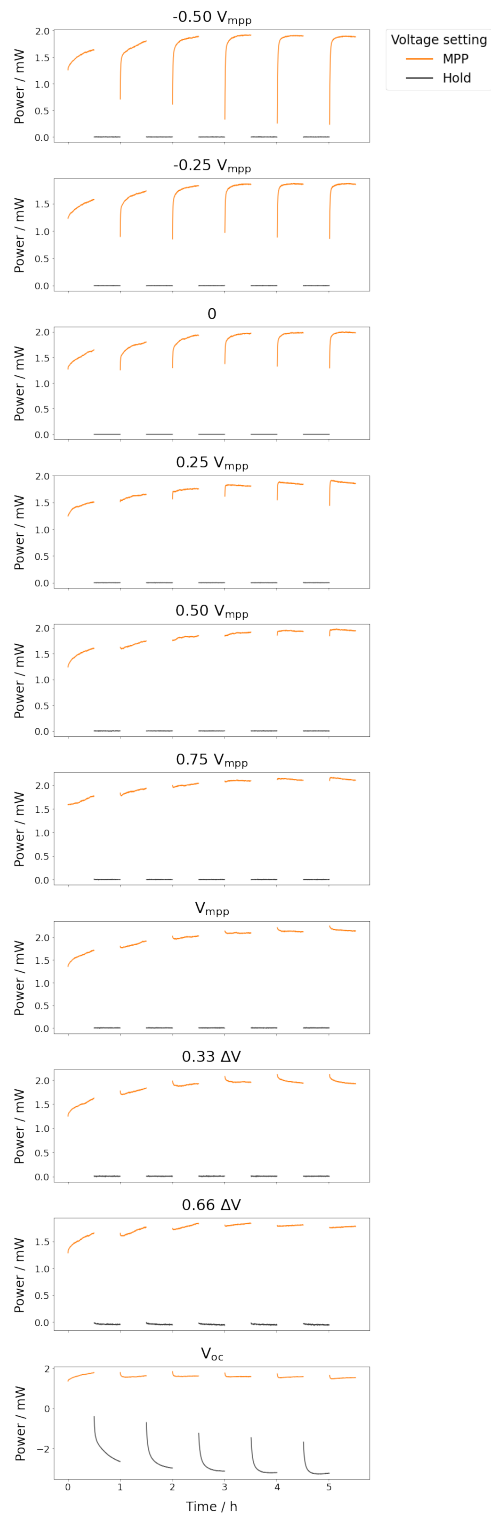


Figure 4.2 – Example of all the data from a single device during the experiment. This device had the lights turned off during the hold voltage periods.

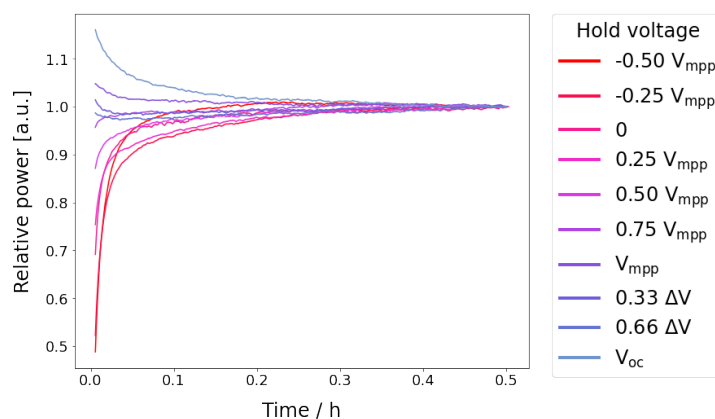


Figure 4.3 – Example of the effect of the hold voltage on the power characteristic during MPP tracking. The data shown is for a single device during a single cycle. The power of each is normalized to the final power to accentuate the different shapes.

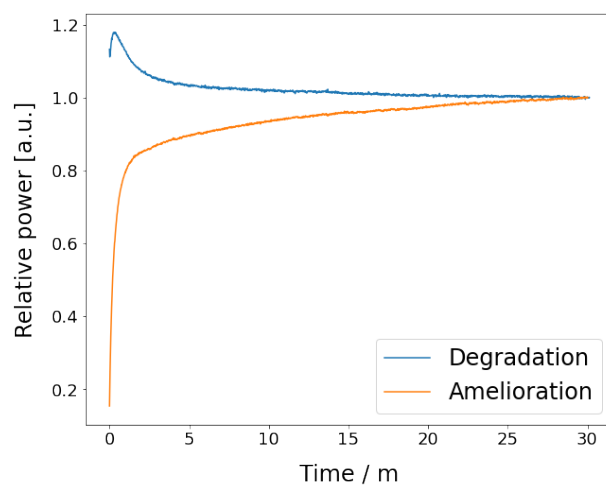


Figure 4.4 – Example of opposing settling behavior showing degradation and amelioration. The power of each is normalized to the final power to accentuate the different shapes.

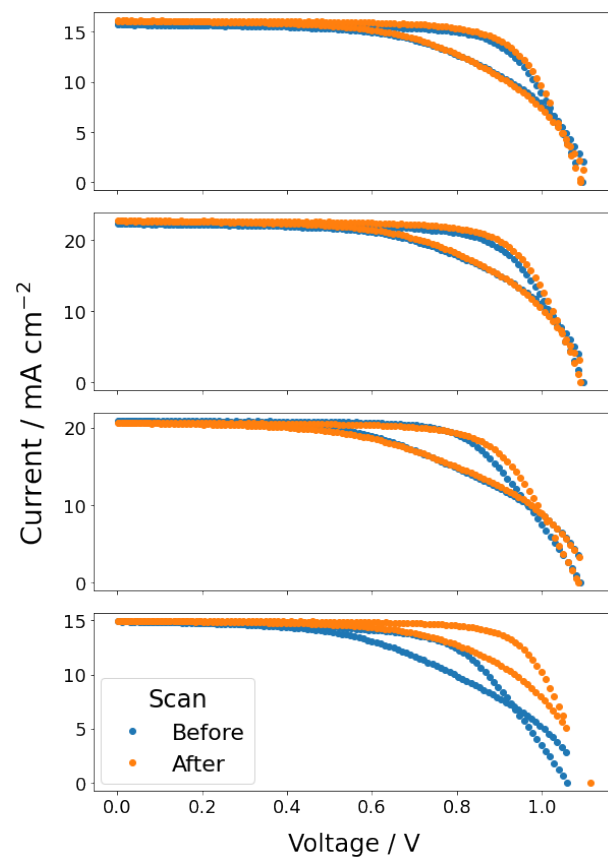


Figure 4.5 – Comparison of JV scans for multiple devices before and after the experiment.

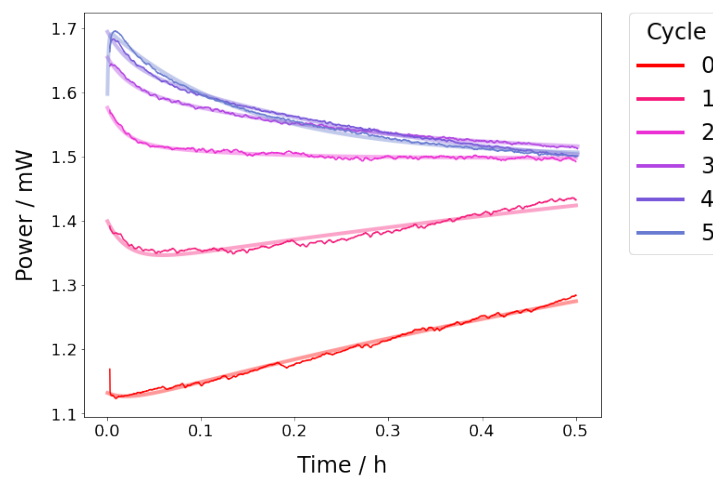


Figure 4.6 – Example of the fits for a single sample at a single hold voltage. The thin opaque lines are the measured data and the thick transparent lines are the fits of the corresponding data.

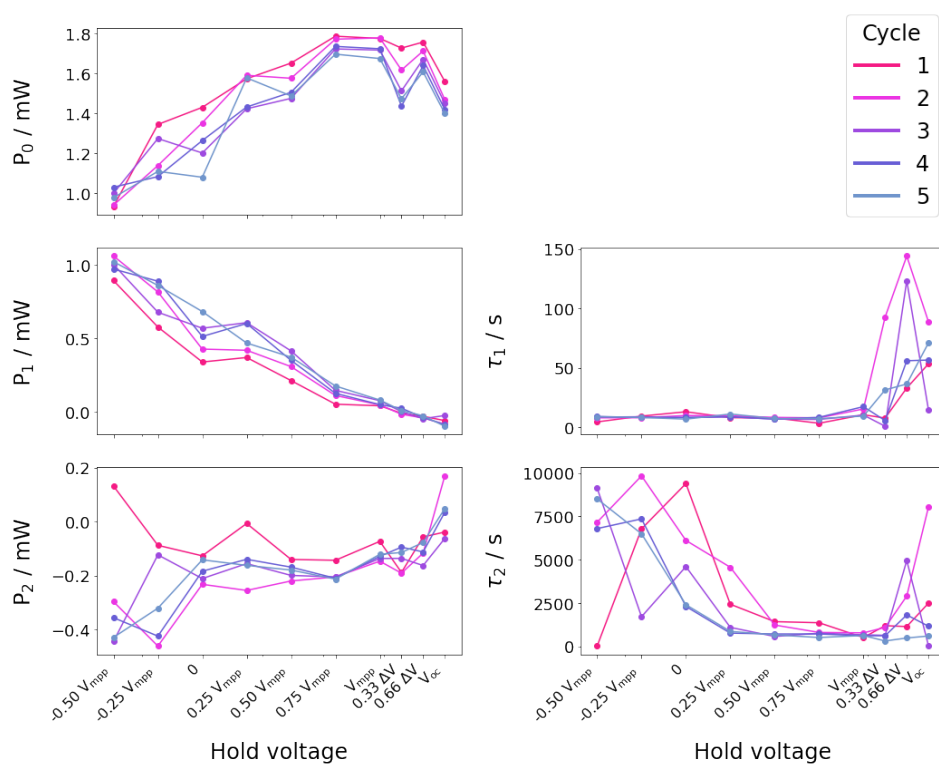
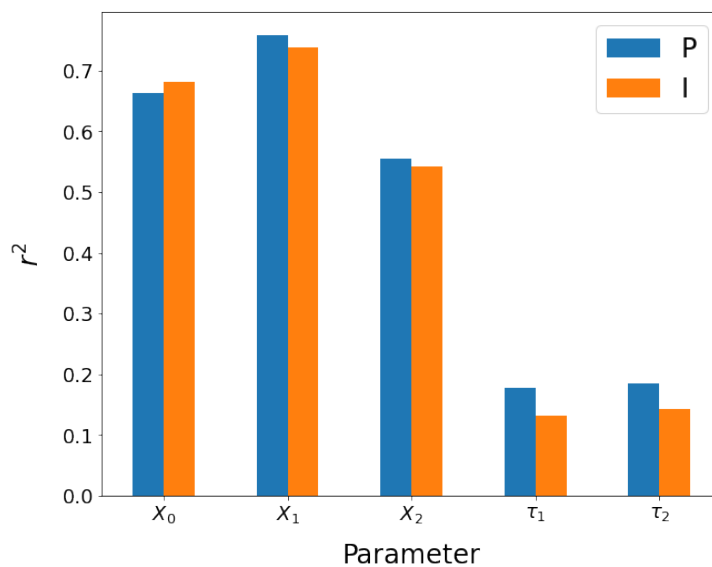


Figure 4.7 – Fit parameters versus hold voltage for a single sample.

Figure 4.8 – Fit parameters versus hold voltage correlation for all samples.  $X$  represents either  $P$  or  $I$ .



A similar process can be carried out for the current instead of the power. This may reveal different trends because the hold voltage is an exogenous variable.

$$I(t) = I_0 + I_1(1 - e^{-t/\tau_1}) + I_2(1 - e^{-t/\tau_2})$$

with the variables and interpretations corresponding one-to-one with those for the power given in Eq. 4.1. Fig. 4.8 reveals that the correlation trends for the current fits match those of the power fits.

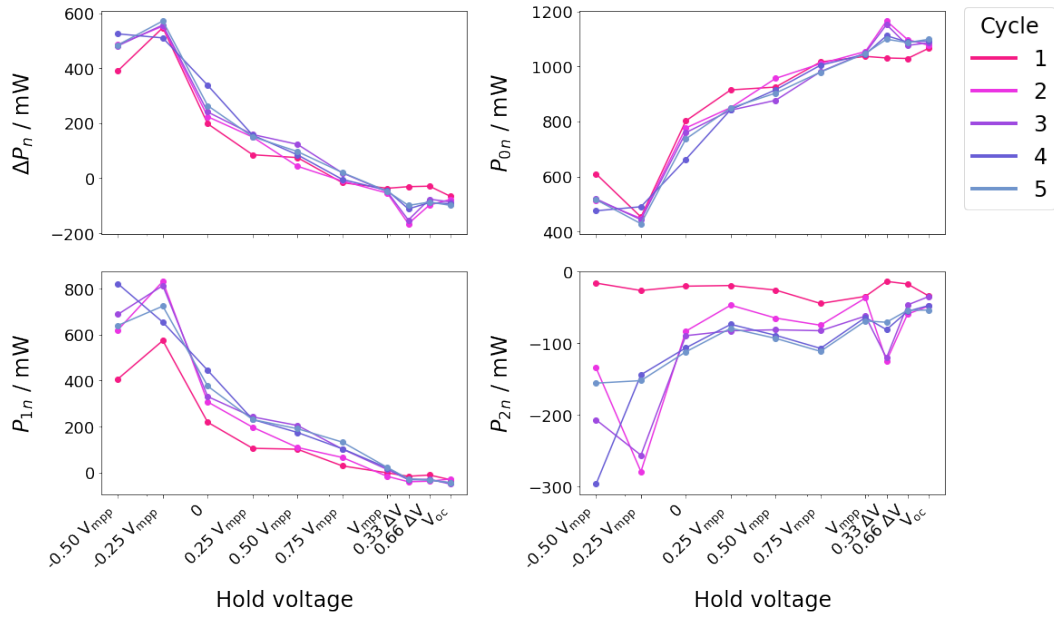
	$X_0$	$X_1$	$X_2$	$\tau_1$	$\tau_2$
P	$0.66 \pm 0.3$	$0.76 \pm 0.3$	$0.55 \pm 0.3$	$0.17 \pm 0.2$	$0.2 \pm 0.2$
I	$0.68 \pm 0.3$	$0.73 \pm 0.3$	$0.54 \pm 0.3$	$0.13 \pm 0.1$	$0.14 \pm 0.2$

Table 4.1 – Average correlation coefficient  $r^2$  of each of the two-term exponential parameters across all samples.  $X$  represents  $P$  or  $I$  in their respective rows.

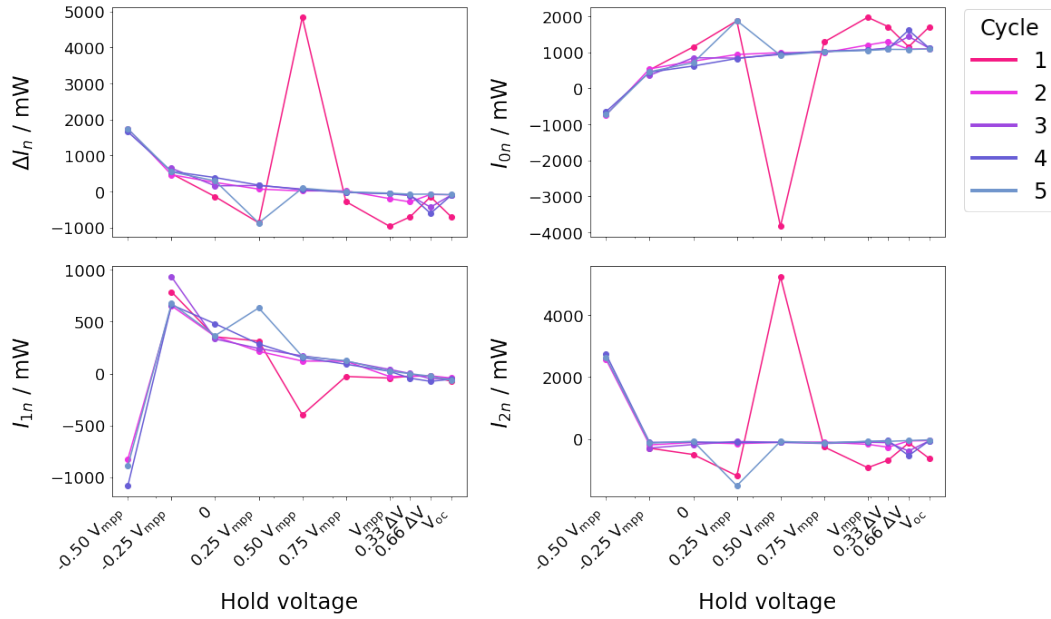
Returning to the two-term exponential we see that  $P(0) = P_0$ , and as  $t \rightarrow \infty$ ,  $P(t) \rightarrow P_0 + P_1 + P_2$ , which we will call  $P(\infty)$ . The difference between the initial and settled power  $\Delta P = P(\infty) - P(0) = P_1 + P_2$ . Because there appears to be no significant irreversible degradation,  $\Delta P$  is an indication of the reversible degradation that occurred. The magnitude of  $(P_1 + P_2)$  indicates the difference between the original power output and the settled power output, and its sign indicates whether degradation is occurring –  $\Delta P < 0$  – or amelioration is occurring –  $\Delta P > 0$ . To compare between devices  $\Delta P$  was normalized to  $\Delta P_n = \Delta P / P(\infty)$  and similarly for  $P_{0n}$ ,  $P_{1n}$ , and  $P_{2n}$ . Fig. 4.9 shows the normalized fit parameters and  $\Delta X$  values plotted against the hold voltage.

We can also examine the correlation between the fit parameters which would point to a common underlying mechanism. Fig. 4.10 shows the correlation for  $P_1$  and  $P_2$  for all the devices across all cycles with the reference composition, MAPbI<sub>3</sub>. In this case  $P_1$  is correlated with  $P_2$  indicating that the stronger the fast degradation mechanism is, the stronger the slow mechanism is as well. However, when varying the perovskite composition, which is discussed shortly, this correlation is only seen in the reference device and the devices varying the cation. Devices in which the halogen was varied did not show any correlation between parameters. As both the fast and slow mechanisms are likely caused by ion migration, albeit of different species, we would expect to see this correlation between  $P_1$  and  $P_2$ . One could postulate that the mechanism enabling easier or harder ion migration for one species would do the same for all migrating species. We hypothesize that this correlation is not seen in the halogen-varying devices due to differences in fabrication, which are detailed in Sec. E2.

In an attempt to understand the ionic motion better, devices of varying composition were used for the experiment. The anion and cation of the devices were changed independently resulting in devices with compositions of the form MA<sub>0.3</sub>FA<sub>0.7</sub>PbI<sub>(1-x)</sub>Br<sub>x</sub> and MA<sub>(1-x)</sub>FA<sub>x</sub>PbI<sub>3</sub>, respectively. When varying the anion we used  $x \in \{0, 0.10, 0.20, 0.30\}$  and for the cation we used  $x \in \{0, 0.125, 0.250\}$ . To see if the composition has an effect of the ionic motion we first



(a)



(b)

Figure 4.9 – Example of normalized fit parameters with delta values versus hold voltage for the (a) power and (b) current. Outlying data points with an absolute standard score greater than 2 were removed.

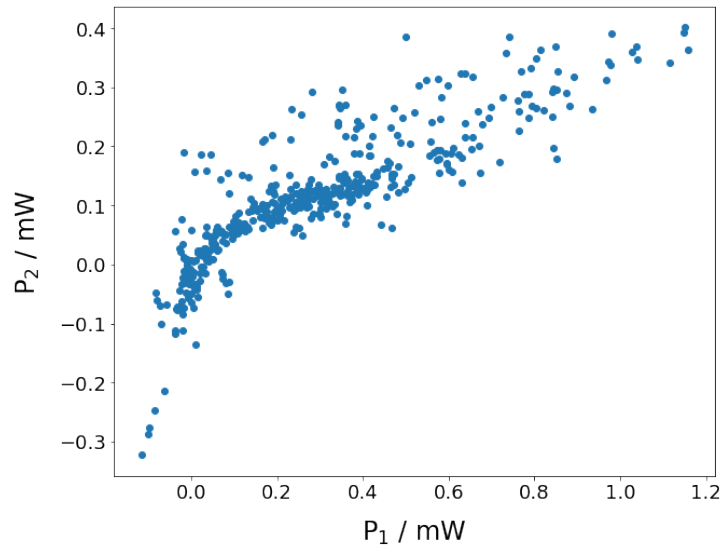


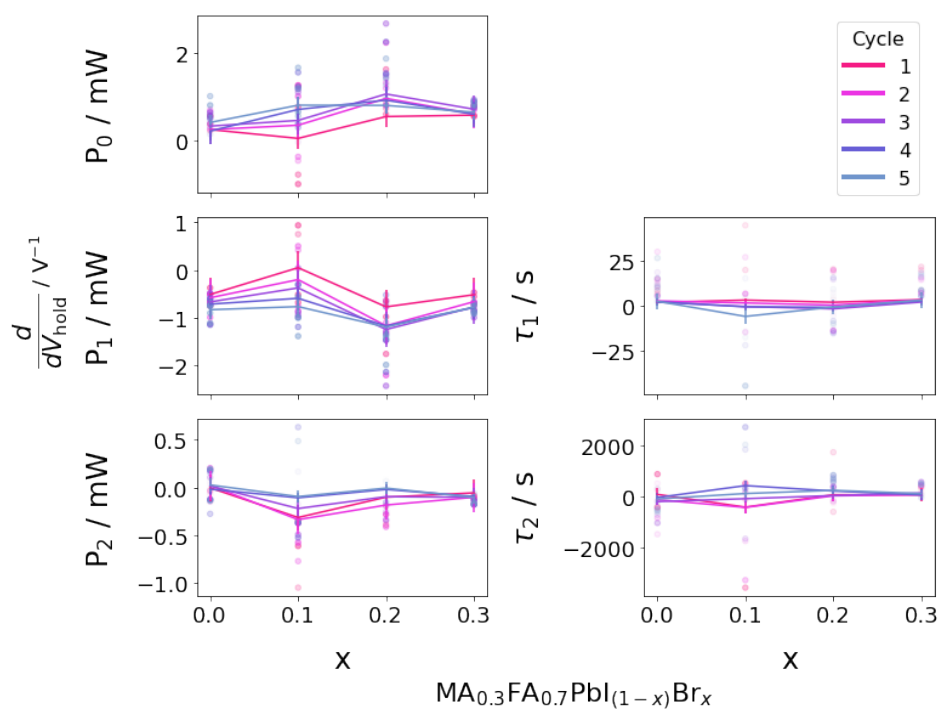
Figure 4.10 – Example of correlation between  $P_1$  and  $P_2$ .

examine the relation between the fit parameters and hold voltage as previously discussed. In general the relationships for  $X_0$  and  $X_1$  were linear as indicated by their high correlation with the hold voltage, as was also discussed before. The  $X_2$  values were also somewhat linear, but the  $\tau$ 's showed very little correlation with the hold voltage. For each of the parameter-versus-hold voltage relationships we performed a linear fit. This gives us the relation between each parameter and the hold voltage as a slope of the form  $dX_i/dV_{\text{hold}}$ . A larger slope indicates that parameter was more sensitive to the hold voltage than a smaller one. We can then plot each of these slopes as a function of the device's composition. This is shown in Figs 4.11 and 4.12 for the power and current fit parameters respectively.

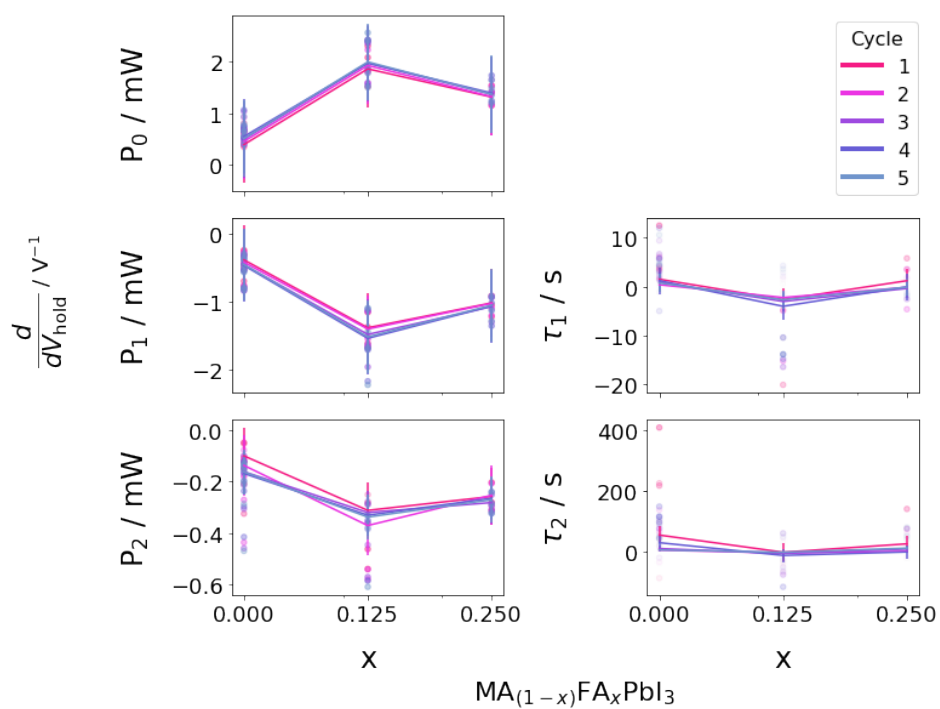
When varying the anion composition the  $r^2$  values for all the parameter sensitivities are exceedingly small, with the largest having an order of magnitude of 0.01. This is visible in Figs 4.11a and 4.12a by noticing that the sensitivity does not vary consistently with the change in composition. While varying the cation, however, we do see a significant variation in the parameter sensitivities. The  $r^2$  values for the cation parameters are mostly around 0.25.

Both Domanski's and our experiment allowed the cells to rest during the experiment. However this confounds the influence of illumination and voltage on the recovery of the devices. To address this another set of experiments was performed without turning the light source off so the cells were illuminated during the hold voltage periods as well as the MPP tracking periods. A comparison of the power and current data for two experiments are shown in Fig. 4.13. The "Rest" referred to in the legend is that of the hold voltage periods, and should not be confused with the rest between voltage experiments as denoted in Fig. 4.1a. The comparison was performed with the compositions  $\text{MA}_{0.3}\text{FA}_{0.7}\text{PbI}_{(1-x)}\text{Br}_x$  for  $x \in \{0.1, 0.2\}$ .

By performing the same fit analysis on this data as we did when the cells were allowed to rest

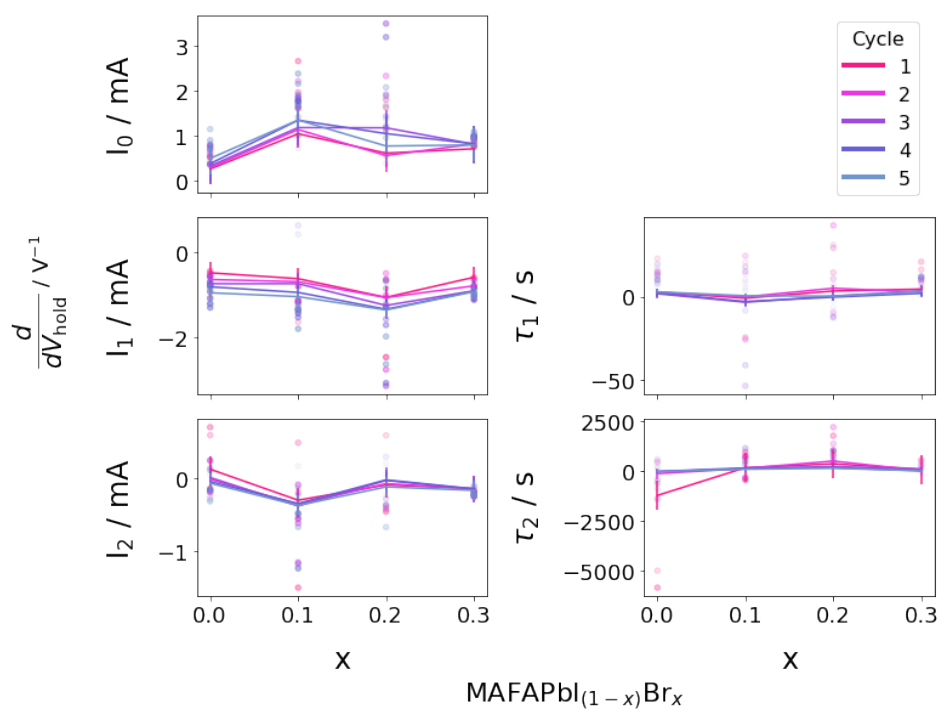


(a)

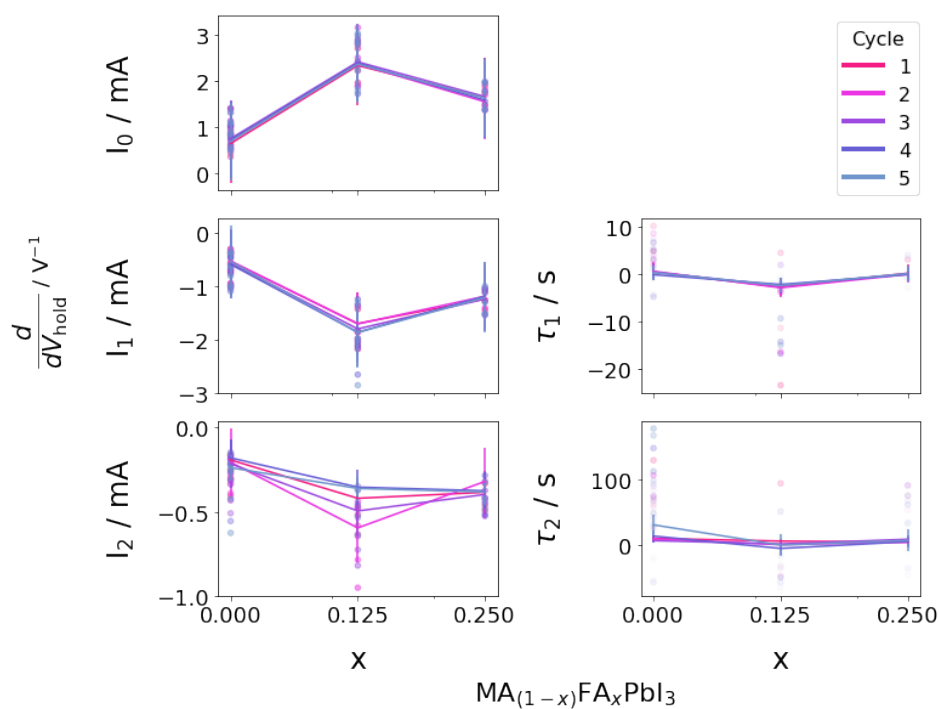


(b)

Figure 4.11 – The effect of composition on the power fit parameters in relation to the hold voltage. The composition of the (a) X-site anion and (b) A-site cation is varied.



(a)



(b)

Figure 4.12 – The effect of composition on the current fit parameters in relation to the hold voltage. The composition of the (a) X-site anion and (b) A-site cation is varied.



Figure 4.13 – Example comparison of (a) power and (b) current when allowing the light to turn off (with rest) during the hold voltage, or keeping it on (without rest). The grey shaded regions indicate periods of hold voltage, while the unshaded regions are periods of MPP tracking. The respective power and current traces are from the same devices, while the devices for with and without rest have the same composition.

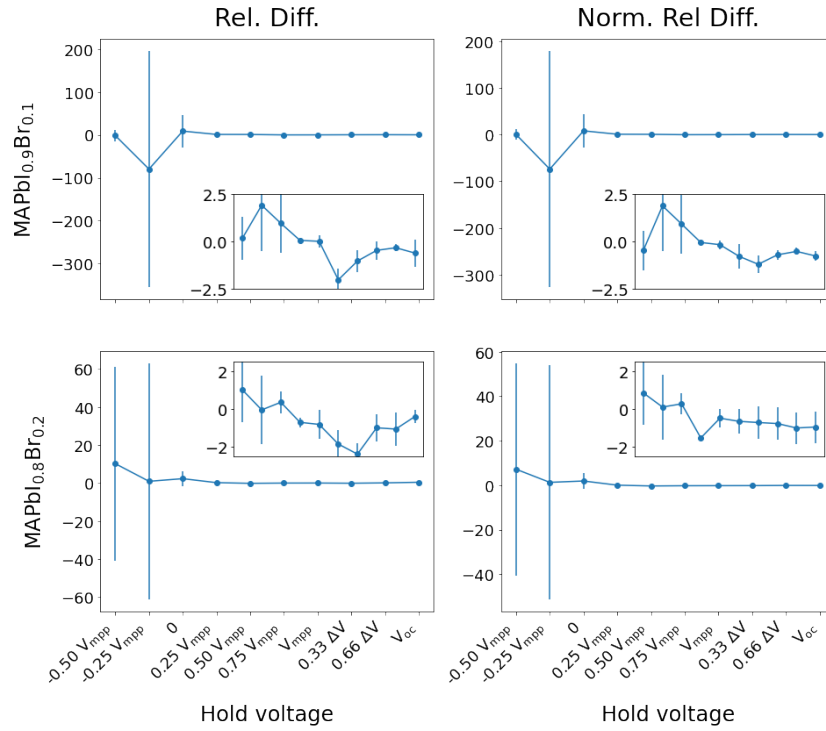


Figure 4.14 – Example of the relative difference between the  $I_0$  fit parameter and its normalized version  $I_{0n}$  for cells with and without rest during the hold voltage periods. The value of the fit parameter when rest was allowed is used as the base value. Inset axes are of the log of the absolute value of the same data. The error bars represent the magnitude of the original error for reference, not the error of the log values.

in the dark, we can compare the transient behavior of the two conditions. In general, the cells without rest show the same characteristic patterns as those allowed to rest: the  $X_i$  fit parameters show somewhat linear trends with the hold voltage with similar  $r^2$  values, and in the same direction. The mean of the relative difference for each of the  $X_i$  parameters and its normalized version  $X_{in}$  across all hold voltages are listed in Table 4.2. The cells with rest allowed were used as the base value and values were weighted inversely to their standard deviation.

$$\Delta X_i = \frac{X_{i, \text{no rest}} - X_{i, \text{rest}}}{X_{i, \text{rest}}}, \quad \overline{\Delta X_i} = \frac{1}{n_{\text{samples}}} \sum \frac{\Delta X_i}{\sigma_{\Delta X_i}}$$

where  $n$  was the number of samples. An example of the relative differences versus hold voltage is shown in Fig. 4.14. Because only two composition variations were used we can not draw any conclusions about the compositional sensitivities when comparing the parameters with and without rest allowed.

The relatively small changes for these values, especially when compared to their errors, is an indication that illumination does not affect these transient behaviors. This points to the

possibility of restoring cell efficiencies under lit conditions, which could be useful in real-world applications.

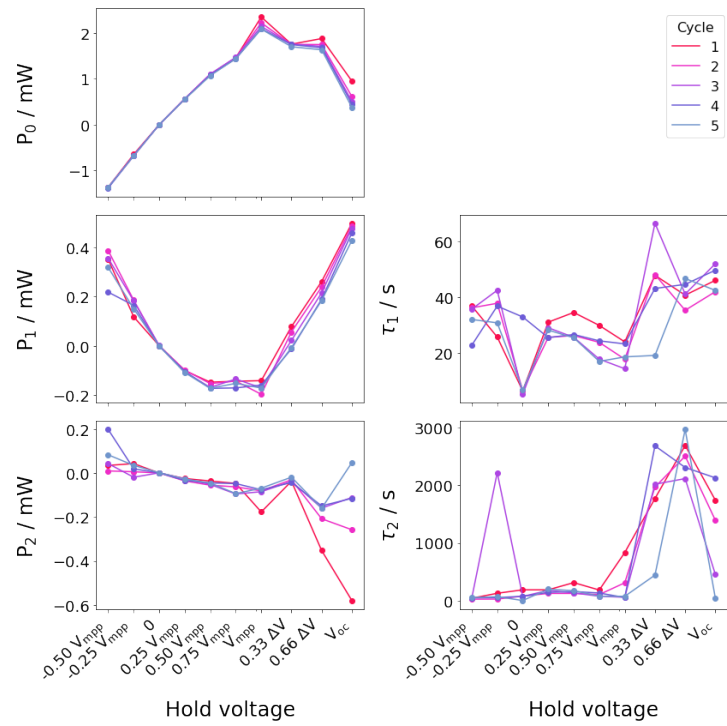
		MA <sub>0.3</sub> FA <sub>0.7</sub> PbI <sub>0.9</sub> Br <sub>0.1</sub>	MA <sub>0.3</sub> FA <sub>0.7</sub> PbI <sub>0.8</sub> Br <sub>0.2</sub>
$P_0$	Rel. Diff.	0.52	0.03
	Norm. Rel. Diff.	0.74	0.01
$P_1$	Rel. Diff.	-0.29	0.05
	Norm. Rel. Diff.	-0.19	0.01
$P_2$	Rel. Diff.	-0.30	-0.72
	Norm. Rel. Diff.	-0.32	-0.71
$I_0$	Rel. Diff.	0.24	0.04
	Norm. Rel. Diff.	0.10	-0.14
$I_1$	Rel. Diff.	-0.11	-0.20
	Norm. Rel. Diff.	-0.33	-0.32
$I_2$	Rel. Diff.	-0.41	-0.96
	Norm. Rel. Diff.	-0.48	-0.93

Table 4.2 – Relative error between the mean of the fit parameters and their normalized counter parts for cells without rest and with rest across all hold voltages. The rest cells were used as the base value, so the values represent the change of the cells without rest relative to those with rest. Values were weighted inversely to their standard deviation.

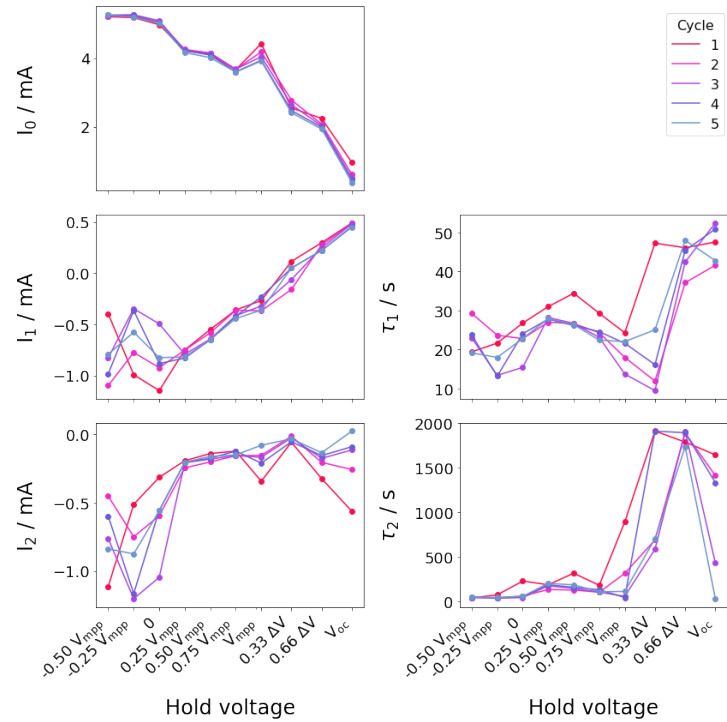
Because the cells remain illuminated during the hold voltage period, we can perform a two-term exponential fit of the same type on the data from hold voltage periods as well. To get a sense of what this data looks like you can refer to Fig. 4.13. An example of the "fit parameters during the hold voltage period" versus the hold voltage for a single device composition is seen in Fig. 4.15. Notice that roughly the same trends are present here as during the MPP tracking periods in regards to the correlation of each parameter with hold voltage. i.e.  $X_0$  and  $X_1$  are highly correlated with the hold voltage, while  $X_2$  is less so, and  $\tau_1$  and  $\tau_2$  show little correlation. Of specific interest is that the relations of the  $\tau$  values with hold voltage still do not show a significant correlation. As discussed earlier, we would not expect the  $\tau$  values to show a correlation with the hold voltage when fitting the MPP period data because the applied voltage during this period is always roughly the same, being the current  $V_{mpp}$ . However this is not the case during the hold voltage periods, when the applied voltage is the hold voltage. Thus we would expect to see a correlation between the hold voltage and the  $\tau$  parameters as the driving force of the suspected mechanism – that of ionic movement – is being directly controlled.

In this study we continued the research presented by Domanski *et. al.* by varying the hold voltage and lighting condition during the cells' rest time, as well as the composition of the perovskite. Through this we found that reversible degradation can be directly controlled through the application of voltage, with illumination showing no significant impact on the transient behavior of the cell. This further supports the theory that the reversible degradation is caused by mobile ions in the perovskite [105]. We also found that the transient behavior of the cell is significantly effected by the composition of the cell, with the hypothesis that





(a)



(b)

Figure 4.15 – Example of fit parameters of during the hold voltage intervals when no rest is allowed.

this could be caused by a balance between disorder within the cell caused by the various components, and the mobility of those components through the perovskite bulk.

## 4.2 Degradation in the real world

The reversible nature of perovskite degradation has been fairly thoroughly explored under controlled laboratory conditions. These solar cells, though, must operate under real-world conditions. The varied combination of temperature and intensity that these cells will be subjected to may create problems that have not been observed under lab conditions. To explore how these real-world conditions effect the nature of reversible degradation, real-world weather data was used to stress the cells. Two days from each month were taken from a weather station in Lausanne, Switzerland. After the main run of the experiment, the conditions from the first three days (0, 1, and 2) were repeated (day 24, 25, and 26) to use as a comparison. To reduce other known degradation mechanisms such as those caused by interaction with atmospheric oxygen and water, the cells were placed in a custom-built setup that provides temperature and light intensity control and is flushed with nitrogen to provide an inert atmosphere.

Two perovskite and two silicon cells were measured over the course of the experiment. Then one of each was used as a representative sample. Before subjecting the cells to the real-world conditions, the characterization parameters of the cells –  $V_{oc}$ ,  $J_{sc}$ , and efficiency (PCE,  $\eta$ ) – were measured by taking a JV scan across a matrix of light intensity and temperature values. The results of these measurements are seen in Fig. 4.16. These values were used as a reference to determine the amount of degradation that occurs throughout the experiment.

To ensure the cells' efficiency could be calculated, the correlation between the produced and incident power was calculated for each day. All correlation coefficients were above 0.99, meaning that the efficiency of the cells could be calculated by taking the ratio of produced versus incident power. The instantaneous power conversion efficiency (PCE) of each cell was also compared to the incident power, finding no correlation between the two. This is beneficial because the temperature and incident power are correlated, i.e. there is likely more illumination from the sun on a hotter day, but because the PCE is independent of the incident power we can focus on the temperature dependence. In the calibration data there does appear to be a slight dependence of the PCE on intensity, however this is absorbed by the error because at lower intensities the error in PCE is larger.

The plots for PCE versus temperature and illumination intensity for each cell are seen in Fig. 4.17. The silicon cell shows a clear temperature dependence with slope  $-0.04\% \text{ K}^{-1}$ . The perovskite cell, however, does not show such a clear linear trend. While the silicon cell has Pearson  $r^2 = 0.27$ , the perovskite has  $r^2 = 0.07$ , almost four times lower indicating a linear model is not a good fit for the perovskite's PCE dependence on temperature. A similar theme is seen with the illumination intensity. The silicon has a fairly strong correlation with intensity with  $r^2 = 0.13$ , whereas the perovskite cell has  $r^2 = 0.00$  – essentially no dependence. We may expect that the temperature and illumination are correlated, and indeed they are, which is explored more later. This confounding explains why the similar trend appears when comparing the effect of temperature and illumination. The low correlation of the perovskite

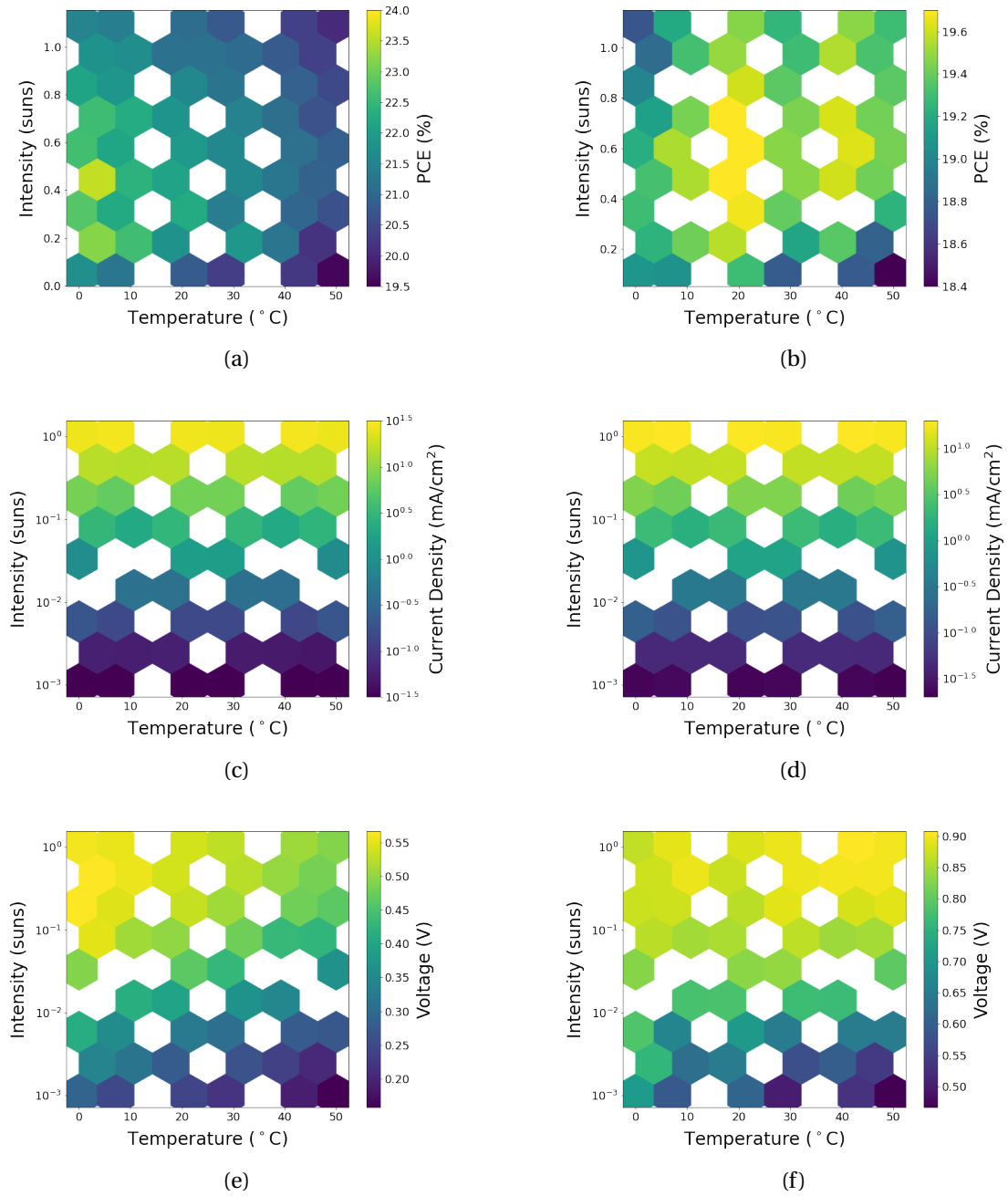


Figure 4.16 – Initial cell parameters of the silicon (a, c, e) and perovskite (b, d, f) solar cells. JV scans were performed over a matrix of light intensities and temperature, and the (a, b) PCE, (c, d)  $J_{sc}$ , (e, f)  $V_{oc}$  were measured.

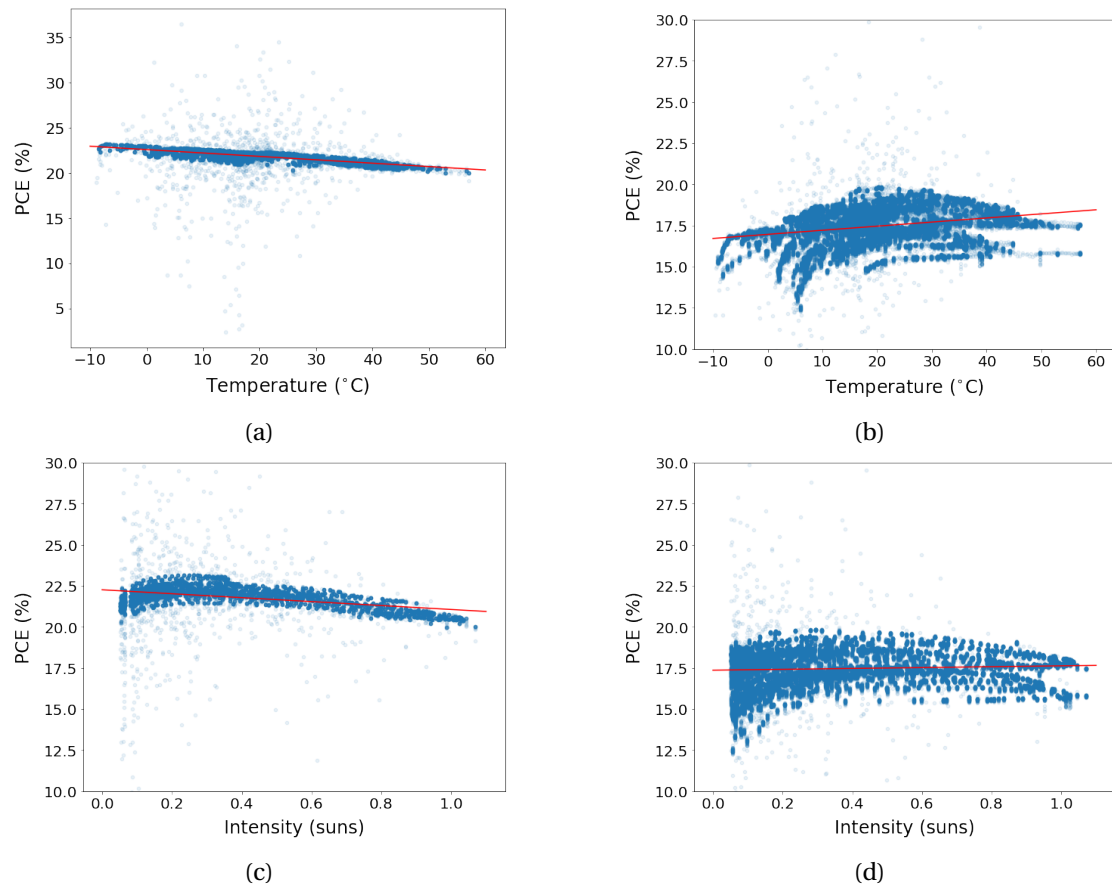


Figure 4.17 – (a, b) PCE versus temperature for the (a) silicon and (b) perovskite cell. (c, d) PCE versus illumination intensity for the (c) silicon and (d) perovskite cell.

cell's efficiency to both temperature and efficiency are anomalous as other literature has indicated that there is a dependence [152, 153, 154, 155]. However, as this is not the main focus of this study, we will just note it as an interesting observation.

Over the course of the experiment, the accumulated energy and average efficiency were calculated for each temperature-intensity interval. i.e. For a given area in the temperature-intensity space, the total energy produced was calculated by integrating the energy produced while the temperature and intensity fell within those bounds throughout the course of the experiment. This was done similarly for the PCE by taking the average of the PCE when the temperature and intensity fell within those bounds over the entirety of the experiment. These

are shown in Fig. 4.18 and described in Eqs 4.2.

$$f_{i,j}(t) = \begin{cases} 1; & T(t) \in T_i \text{ and } I(t) \in I_j \\ 0; & \text{otherwise} \end{cases} \quad (4.2a)$$

$$u_{i,j} = \int f_{i,j}(t) P(t) dt \quad (4.2b)$$

$$PCE_{i,j} = \frac{\int f_{i,j}(t) PCE(t) dt}{\int f_{i,j}(t) dt} \quad (4.2c)$$

where  $i$  and  $j$  index the temperature and intensity bins respectively,  $f$  acts as a selective function,  $u$  is the energy density,  $P$  is the power density,  $t$  is time, and the integration is over the span of the experiment.

Taking the difference of the integrated energy between the silicon and perovskite cells for each temperature-intensity bin shows that the silicon cell outperforms the perovskite cell across the range of conditions, summing to a total difference of  $301.5 \text{ mWh cm}^{-2}$  throughout the course of the experiment. This is visualized in Fig. 4.18e, and the total energy densities throughout the experiment are listed in Table 4.3.

	Total energy density / $\text{mWh cm}^{-2}$
Silicon	1777.6
Perovskite	1476.0

Table 4.3 – Total energy density produced by each cell throughout the entirety of the experiment.

The day-by-day plot for the silicon and perovskite cell are seen in Fig. 4.19 and a summary is seen in Fig. 4.20. This shows a clear degradation in the perovskite cell, while the silicon cell is stable. By comparing the collected data to the characterization data we can analyze the degradation of the cell. We can then categorize the degradation with the temperature-intensity context and analyze how the cells are effected differently. Fig. 4.21 shows this comparison for a single day. The solid lines are the measured PCE, while the dotted lines are the PCEs obtained from the initial calibration at the same temperature and intensity the cell experienced. We can see quite clearly here the effect that temperature has on the silicon cell, with the PCE dropping as the temperature rises. More strikingly is the difference in degradation between the two cells. While the measured and predicted PCE of the silicon cell match almost exactly, even at the abrupt dip around hour 20, the perovskite cell shows a much weaker correlation with its predicted PCE. While the PCE of the perovskite differs significantly from its calibration values, interestingly, the high frequency components for both cells remain

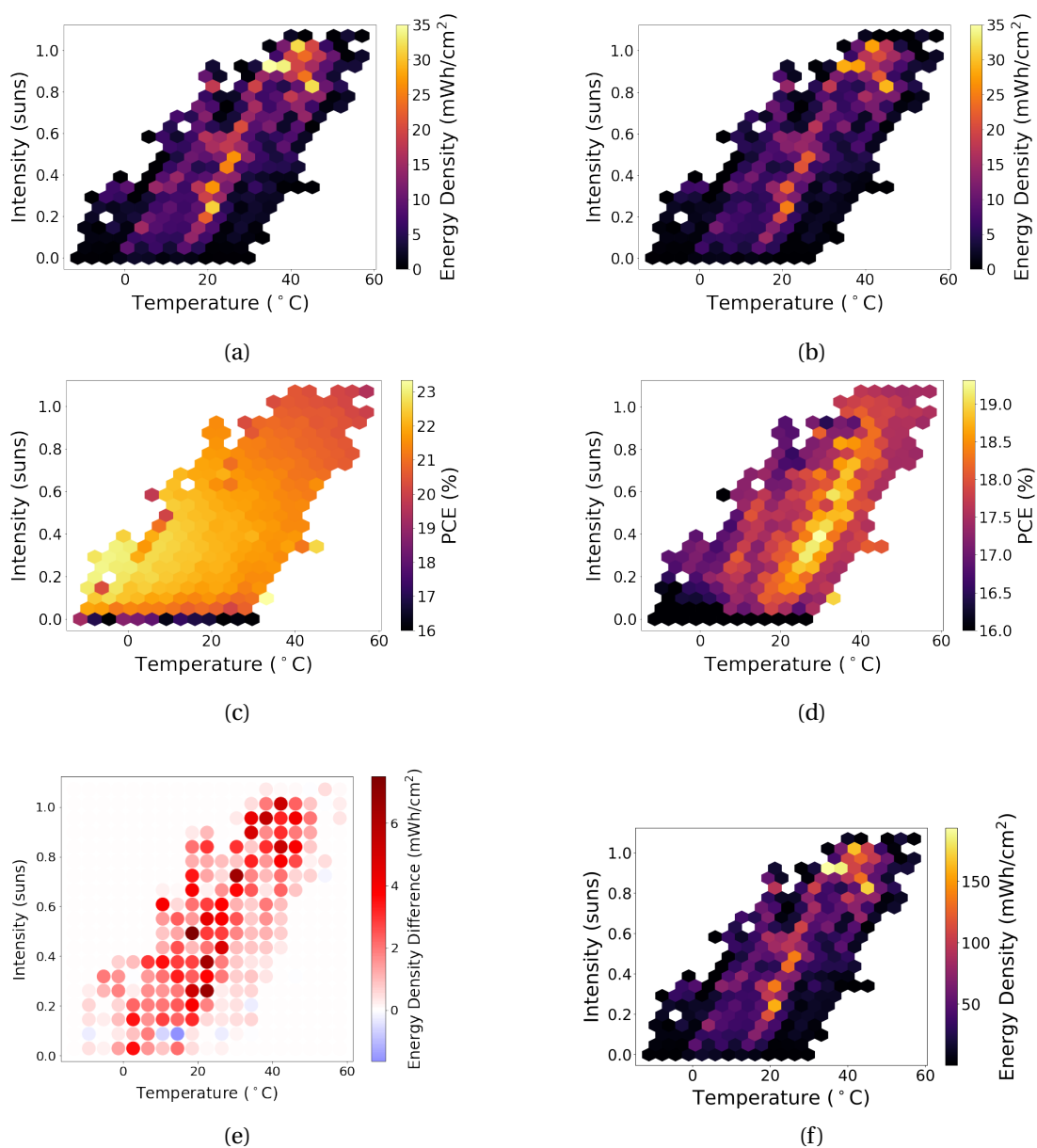


Figure 4.18 – (a, b) Integrated energy density over the course of the experiment of the (a) silicon and (b) perovskite cell. (c, d) Average PCE over the experiment for the (c) silicon and (d) perovskite cell. (e) Difference in energy density between the silicon and perovskite cell for each temperature-intensity bin. Positive values indicate the silicon cell had a higher energy density. (f) Total incident energy density.

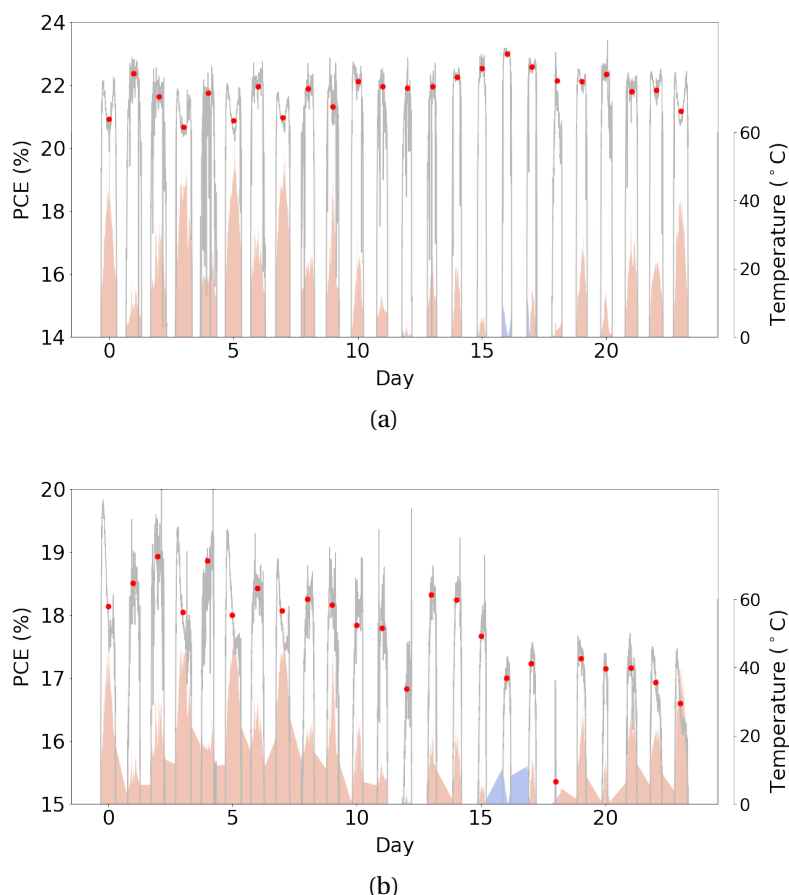


Figure 4.19 – Daily PCE for the (a) silicon and (b) perovskite cells. The grey lines indicate the instantaneous PCE, the red dots are the daily average PCE when the light intensity was greater than 0.075 sun, and the red and blue area is the temperature. Red indicates temperatures above 0 °C and blue is temperatures below 0 °C. While the temperatures appear different in the plots, they are actually the same. This is an artifact of how the plotting was performed.

fairly true to their calibration. This can be seen by comparing the fast fluctuations in the PCE caused by temperature and illumination variations. Fig. 4.22 shows similar plots – comparing the measured and predicted PCE – for each day. Here again we see how closely the silicon cell matches the prediction for the duration of the experiment indicating its stability, while the perovskite cell drifts further and further from its predicted values due to degradation.

To quantify the degradation we split it into two categories. Reversible degradation indicates how much PCE would be regained by letting the cell rest for a sufficient amount of time, while irreversible degradation can not be recovered from rest. To calculate this, for each day we assume that the point when the difference between the predicted and measured PCE is minimized is caused completely by irreversible degradation. To remove the effect of this irreversible degradation, the PCE is scaled such that at the point of minimum difference



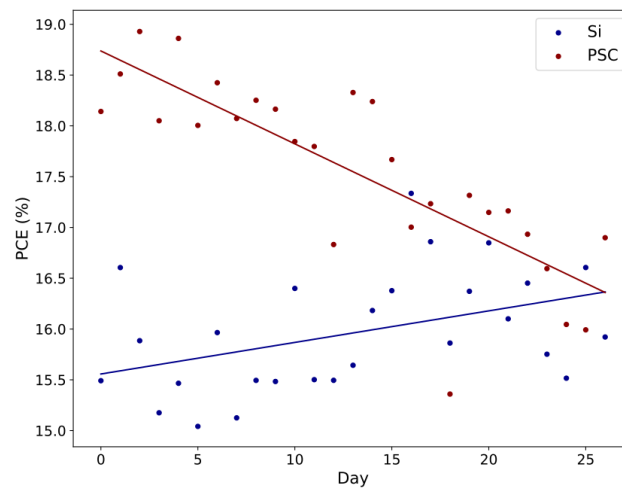


Figure 4.20 – Average daily PCE for the silicon (Si) and perovskite (PSC) solar cells with linear fits. Clear degradation is seen for the perovskite cell.

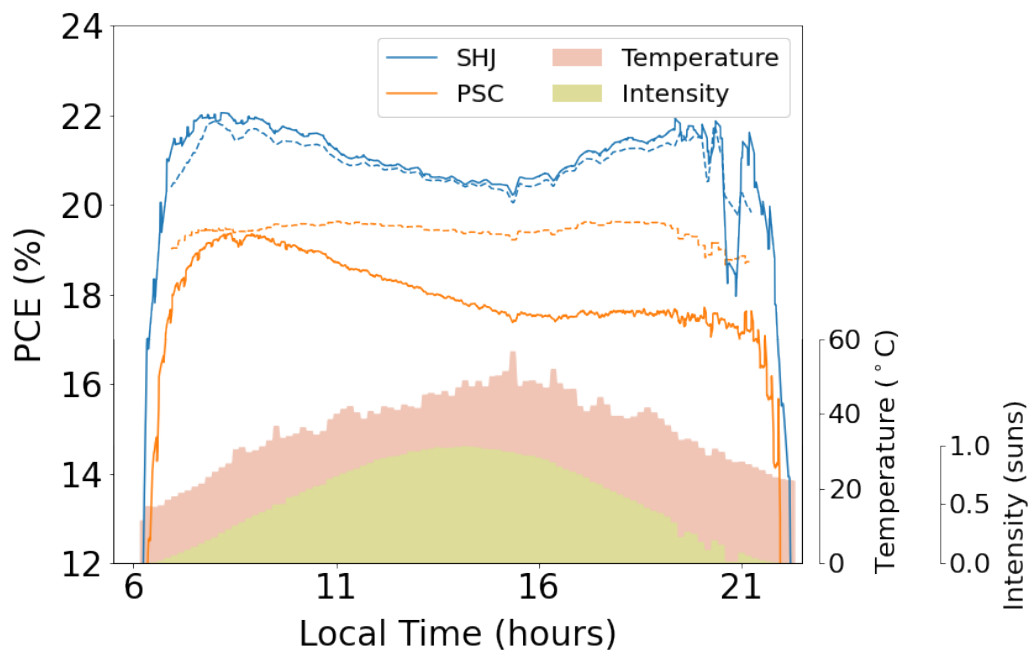
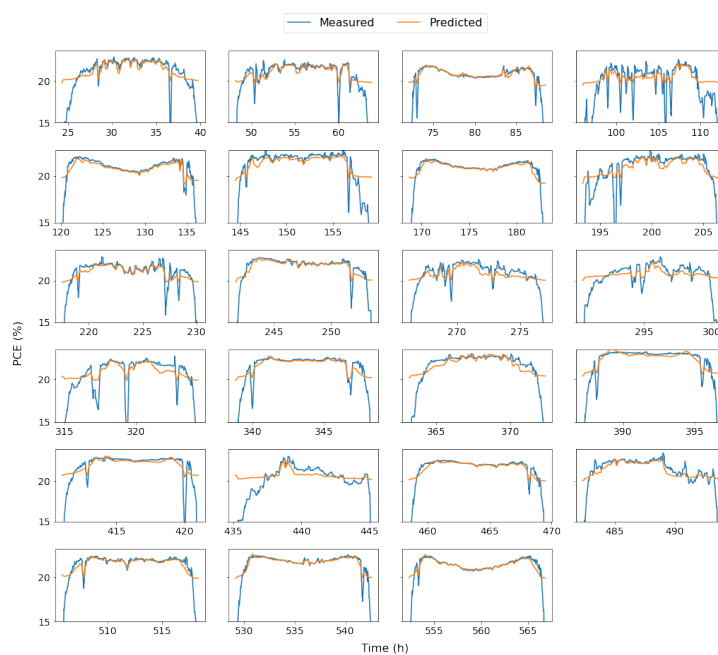
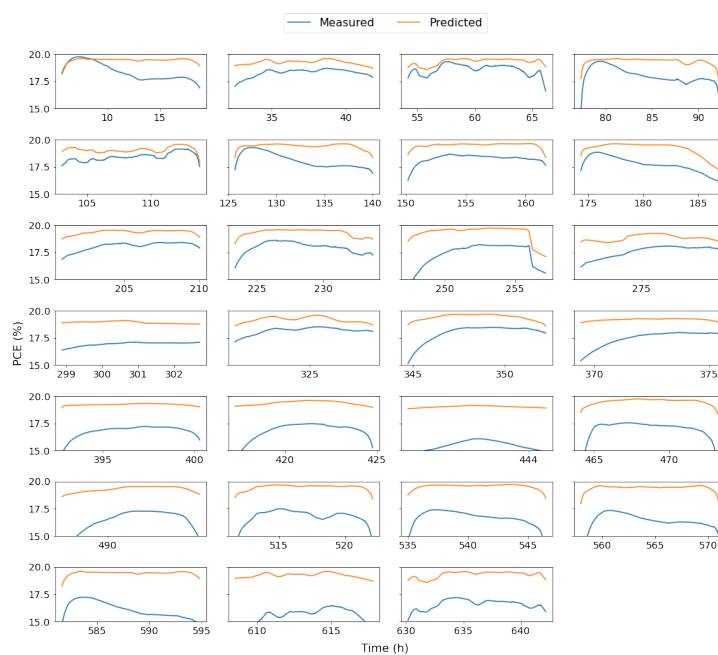


Figure 4.21 – The measured and predicted efficiency of the silicon (SHJ) and perovskite (PSC) cell, along with the temperature and intensity. The solid lines are the measured data, while the dotted lines are the predicted PCE calculated from the calibration data given current temperature and intensity the cell is experiencing.



(a)



(b)

Figure 4.22 – The measured and predicted efficiencies of the (a) silicon and (b) perovskite cell for each day. The predicted efficiencies are found by linearly interpolating the calibration data. The increasing separation between the measured and predicted PCE of the perovskite cell reveals the degradation occurring, while the measured PCE for the silicon cell shows no such trend, correlating closely with its predicted PCE.

the measured PCE equals the predicted PCE, as seen in Figs 4.23a and 4.23b. The energy collected with this adjusted PCE is then calculated. This represents the energy that would have been collected had these conditions been present when the cell was fresh. Thus any difference between this energy and the actual energy collected can be attributed to irreversible degradation. This is visualized in Fig. 4.23c. This calculation assumes that the degradation mechanisms operate in a linear way. i.e. If irreversible degradation occurs dropping the PCE from 20% to 18%, the degradation should not be considered as 2 percentage points, but rather as  $(1 - 18/20) = 10\%$  of the PCE. Thus, if the next day's undegraded PCE would have been 15%, given the conditions, then we expect its measured PCE to be  $13.5\% = 15(1 - 0.1)\%$ , not  $13\% = (15 - 2)\%$ . The need for this intraday measure of reversible and irreversible degradation arises because of the large day-to-day variation in the conditions the cells experience. Ideally one could measure the irreversible degradation between days, but this would require the same conditions to be present each day, which is not the case here.

Examining the day-by-day evolution of the reversible and irreversible degradation losses, seen in Fig. 4.24, reveals an interesting trend. While the losses from the irreversible degradation grows over time, the losses from reversible degradation remain essentially constant. This is a strong indication that the mechanisms underlying the reversible degradation do not change over time, and are neither impeded nor enhanced as the cell undergoes irreversible degradation.

To examine the contribution of temperature and intensity to degradation we can examine the change in efficiency as a function of them. There is a clear dependence of the reversible degradation on temperature with  $r = 0.68$ , as shown in Fig. 4.25a, however there is a strong correlation of  $r = 0.77$  between temperature and intensity as seen in Fig. 4.25b. This make disentangling the contributions difficult. Because the reversible and irreversible degradation are only analyzed on a day to day basis in our analysis we only have 24 data points to analyze. However, we can try to parse out the influence of each of these factors on degradation-as-a-whole more easily.

Fig. 4.26 shows the mean change in PCE when comparing the first three days to when the same temperature and intensity conditions were run again after the rest of the experiment. If we somewhat discount the low light intensity data due to the likely larger errors present in the PCE data, there seems to be an almost uniform change in the relative PCE change. This gives some support to the process used to calculate the reversible and irreversible degradation, which assumed that degradation was a relative phenomenon. However, some variation is clearly present which shows up for both the absolute and relative changes. If it were the case that the absolute PCE change was homogeneous across conditions, this would point to a mechanism that chops off some set amount of efficiency. A mechanism like this seems quite unlikely though. On the other hand if the relative efficiency change were homogeneous, this would point to the commonly known mechanisms for degradation being at play such as ionic migration or decomposition of the perovskite. The fact that both the absolute and relative PCE differences vary could point to different degradation mechanisms being active under different

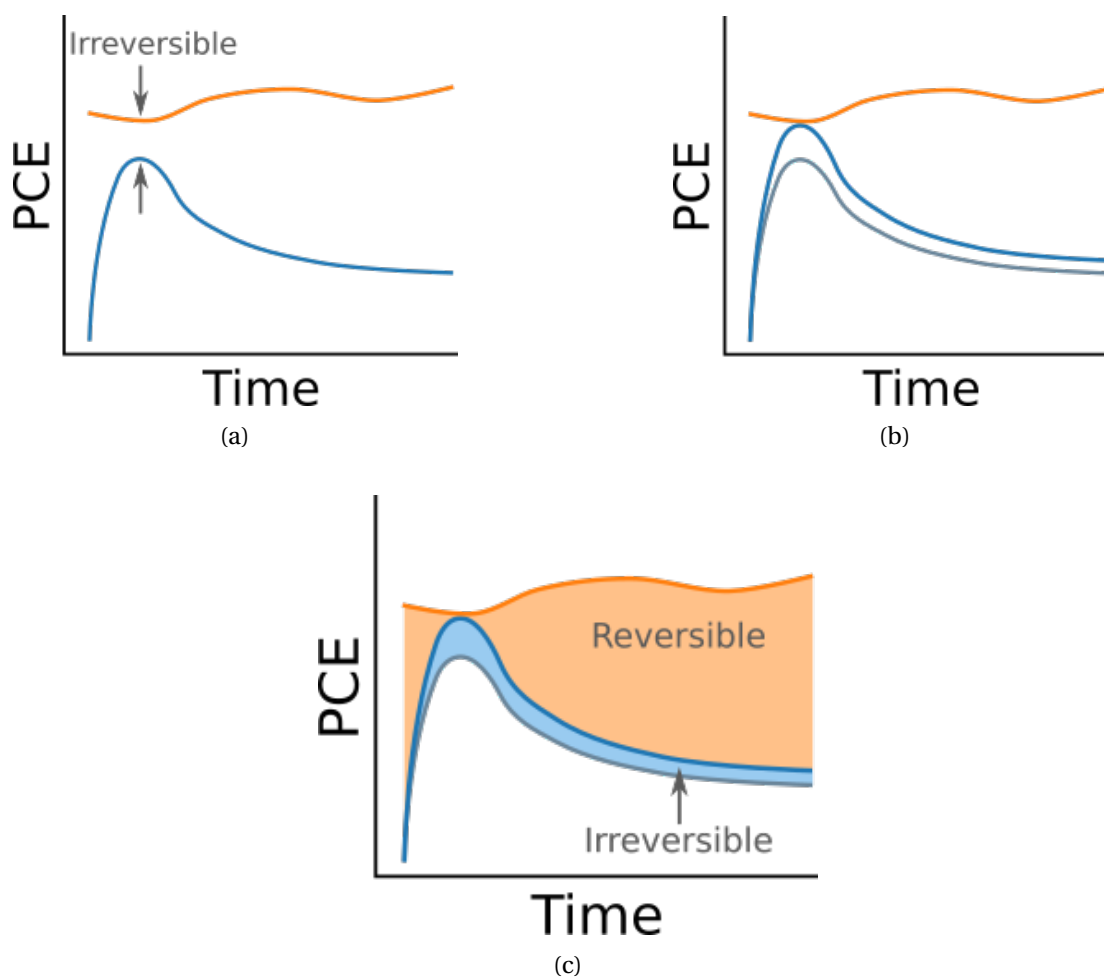


Figure 4.23 – Visualization of the steps taken to calculate the reversible and irreversible degradation. (a) We first locate the point at which the difference between the measured PCE and the PCE predicted from the calibration data is minimized. (b) We then scale the measured PCE such that the PCE at the point of minimum difference is equal to that of the calibration PCE. (c) The energy losses from reversible degradation are calculated as the difference in energy between the calibration PCE and the adjusted PCE (orange). Energy losses from irreversible degradation are the remaining losses between the adjusted PCE curve and the measured PCE curve (blue).

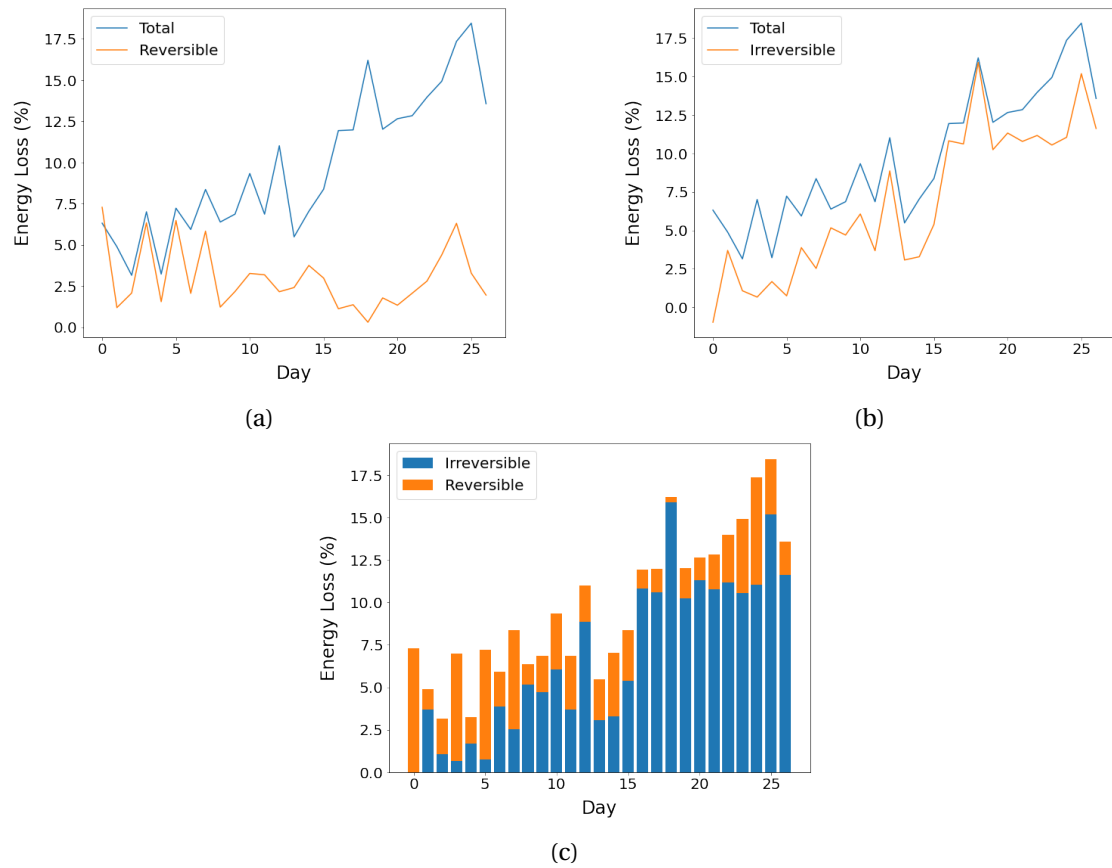


Figure 4.24 – Day by day plot of (a) reversible and (b) irreversible energy losses in comparison with the total energy loss. The values for day 0 are due to the measured PCE exceeding the calibration PCE. (c) Stacked plot of the reversible and irreversible degradation for each day. Energy losses are as a percentage of the possible energy as calculated from the calibration data.

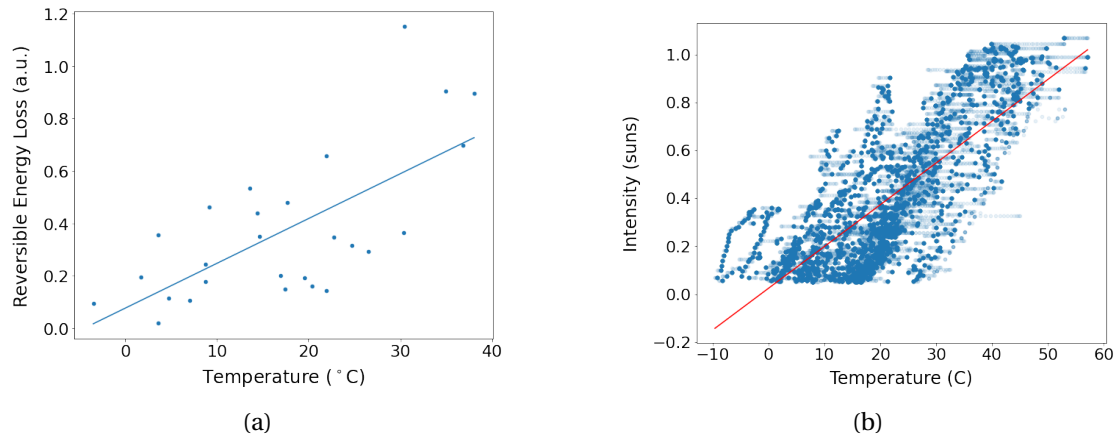


Figure 4.25 – (a) Dependence of energy losses caused by reversible degradation on temperature as a percentage of the total daily energy loss. The value above 1 is from day 0, when the measured PCE exceeded the calibration PCE. (b) Correlation between the temperature and intensity throughout the experiment. The red line is the linear fit.

conditions and warrants further investigation.

Fig. 4.27a shows the mean change in PCE from predicted over the space of temperature and intensity values encountered throughout the experiment. Examining each row individually we see that colder temperatures tend to show a larger decrease in PCE than warmer temperatures. Similarly, examining column by column reveals that higher intensities tend to show more degradation. We can quantify this by taking the time derivative of the PCE and correlating it to the temperature and intensity. Due to the correlation between the temperature and intensity we must condition on each of the variables. i.e. When calculating the dependence of the change in PCE on temperature, we will condition the fitting on intensity by breaking the data into intensity bins, linearly fitting the data within each bin, and then recombining the data. This is analogous to what we did visually by looking at each row-by-row and column-by-column in Fig. 4.27a.

Performing this analysis using the same bins as in Fig. 4.27a we find the values listed in Table 4.4. Looking at the  $r^2$  coefficients, temperature shows an orders of magnitude higher correlation with the change in PCE than does the intensity. This finding is in agreement with those previously reported in literature [156, 157]. Interestingly though, the change in PCE seems to be more sensitive to the intensity – i.e. has a steeper slope – as seen when comparing the slopes of the fits. An example of the PCE change as a function of temperature is seen in Fig. 4.28.

We can also take a more wholistic view of the data. Fig. 4.27b shows the total energy lost throughout the experiment in each region of the temperature-intensity space, Fig. 4.27c shows the total time spent in each of the regions, and Fig. 4.27d is a reprint of Fig. 4.18f showing the total incident energy density of each region throughout the experiment. By comparing these

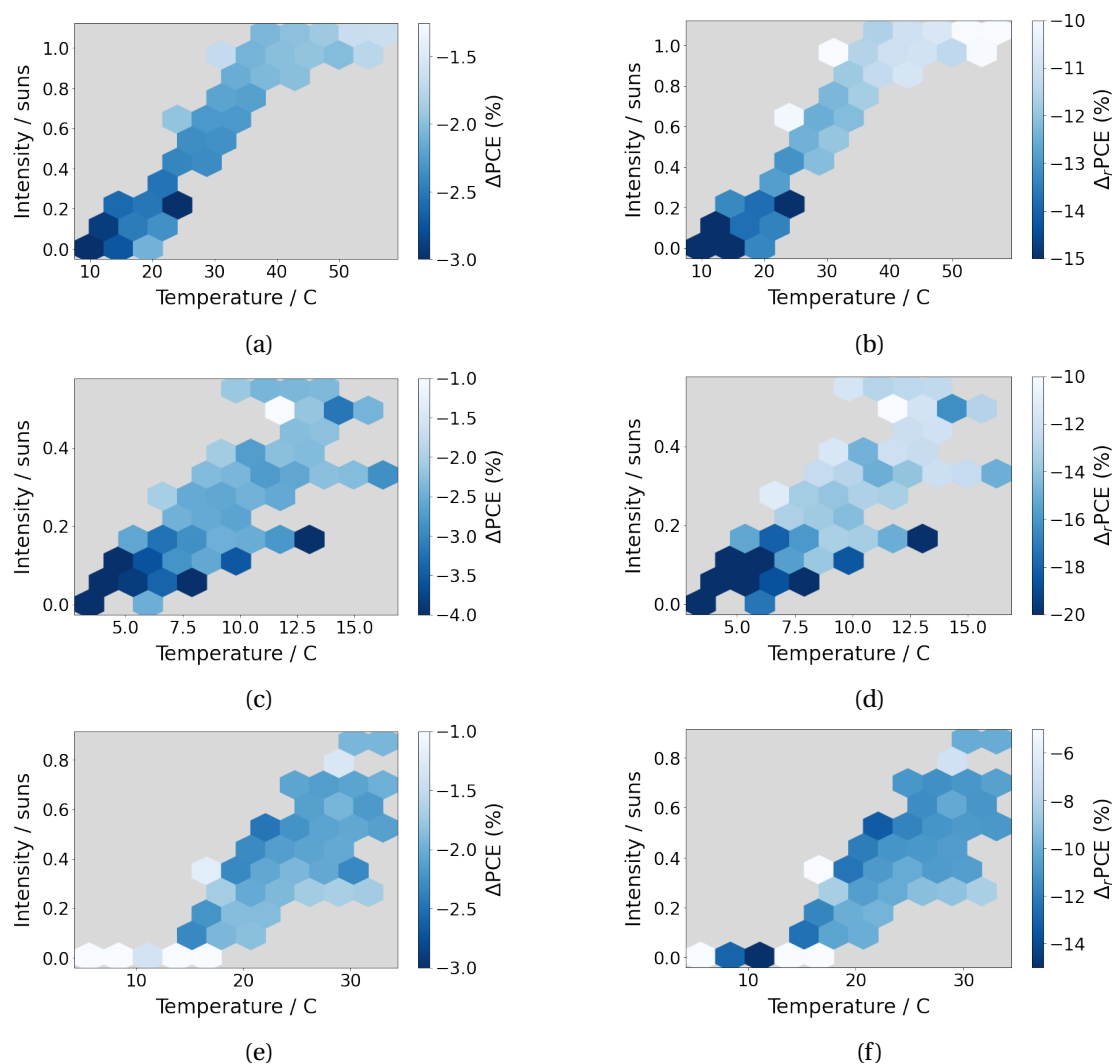


Figure 4.26 – Difference in PCE between the first three days – (a, b) day 0, (c, d) day 1, and (e, f) day 2 – of the experiment and after the experiment when those days were run again. (a, c, e) The absolute difference between PCEs. (b, d, f) The relative difference between the PCEs. The grey background indicates regions in the temperature-intensity space that did not occur during that day.

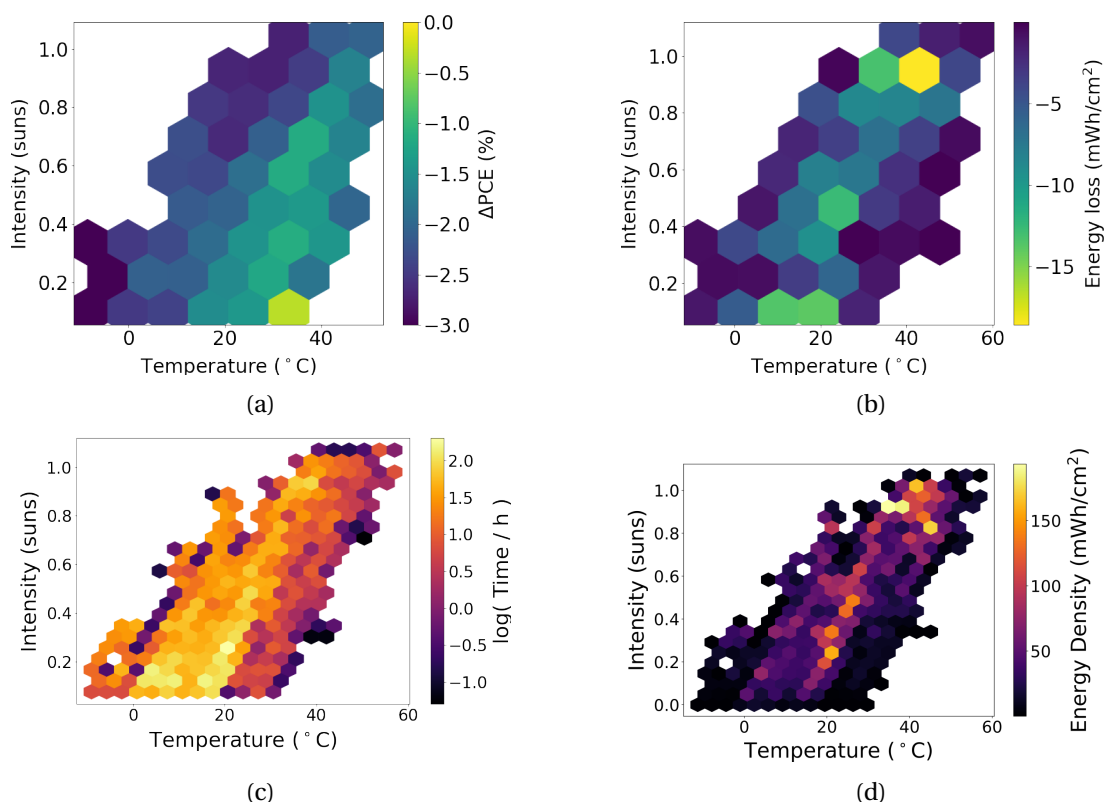


Figure 4.27 – (a) Mean of the difference between the predicted and measured PCE for each region in the temperature-intensity space over the course of the experiment. (b) Energy loss for each region in the temperature-intensity space throughout the experiment. In both plots, data with intensities lower than 0.1 sun were excluded due to large errors. (c) Total time spent in each region of the temperature-intensity space. Data with an intensity less than 0.075 sun was removed. (d) Total incident energy for each region in the temperature-intensity space over the course of the experiment. This is the same as Fig. 4.18f, reprinted here for convenience.



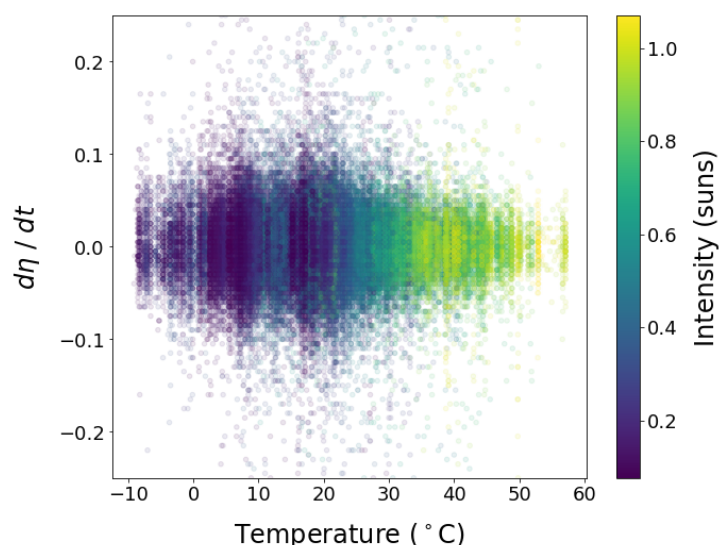


Figure 4.28 – Plot of the change in PCE with time as a function of temperature, colored by intensity.

we see that things are as we would expect. The most incident energy, and energy losses come from areas where more time is spent.

	Absolute		Relative	
	Slope	$r^2$	Slope	$r^2$
Temperature	-5.0 E-4	6.3 E-4	-3.1 E-5	6.2 E-4
Intensity	-2.2 E-3	5.4 E-7	-1.4 E-3	3.6 E-6

Table 4.4 – Fit parameter values of the instantaneous change in PCE as a function of temperature and intensity. Absolute values are the absolute change in the PCE, while Relative values are the relative change in PCE. Temperature values were computed conditioned on intensity, and vice versa.

In this study we explored the effects that real-world temperature and illumination conditions on the degradation of perovskite solar cells. By using calibration measurements taken before the application of the real-world conditions we were able to quantify the degradation on a day-to-day basis. An algorithm for separating reversible from irreversible degradation was proposed, and used to show that while irreversible degradation continuously increased, reversible degradation stayed constant across the course of the experiment. We were also able to quantify the correlation in the change in efficiency with the temperature and illumination conditions. Here we found that the correlation between temperature and the change in efficiency is roughly 100 times larger than that with illumination, which was inline with previous literature reports.



## 5 Temperature dependence of photoluminescent and electronic properties

When considering the behavior of a solar cell, one of the most fundamental mechanisms we can look at is the properties of the charges within the active material. How charges travel within the material, recombine radiatively and non-radiatively, and transfer into the transport layers all reveal information about what fundamental mechanisms are at work in the perovskite. By understanding these mechanisms and their effects we can attempt to engineer away those that are undesirable, and lift up those that are.

As was discussed in Ch. 3, photoluminescent quantum yield (PLQY) reveals a plethora of information about the charge carrier recombination occurring in a material. While PLQY reveals the absolute values of these values, we can use a relative measure of PLQY to understand the trends occurring in a material. By combining the results of PLQY with that of electronic characterization we can boost the efficacy of these findings superlinearly.

Using JV scans we can calculate the basic characterization parameters –  $V_{oc}$ ,  $J_{sc}$ , fill factor (FF), and efficiency – of a device. While the efficiency of a cell gives us a macroscopic view of its performance, it does not tell much about the actual mechanisms at play. The  $V_{oc}$ ,  $J_{sc}$ , and fill factor, though, do reveal what mechanisms could be at play. Because of the complex nature of perovskites, we do not have a one-to-one mapping of mechanism to property though. For instance, it could be the case that the only detrimental factor to the  $V_{oc}$  were Shockley-Read-Hall (SRH) recombination. Unfortunately in perovskites this is not the case, and not only will SRH recombination affect the  $V_{oc}$ , it may also lower the  $J_{sc}$  or fill factor. We already saw signs of this in Ch. 2. Because of the entanglement between these properties and their mechanisms, it is important to consider them in more detail.

Open-circuit voltage is a measure of the quasi-Fermi level splitting, just as the PLQY is. This points to a direct connection between the two that we should be able to see experimentally. The main suppression of the quasi-Fermi level splitting comes from non-radiative recombination. In perovskite cells this occurs both in the bulk via SRH recombination, as well as at the transport layer interfaces [158]. Perovskites offer a challenge when comparing the PLQY and  $V_{oc}$ , though. Due to the relatively low mobility in perovskites, the quasi-Fermi level for each

charge species may not be constant across the extent of the device. This leads to a decrease in the measured voltage across the cell, resulting in the quasi-Fermi level splitting that would be calculated from PLQY to be significantly larger than that measured from the  $V_{oc}$  [119, 159]. This is visualized in Fig. 5.1.

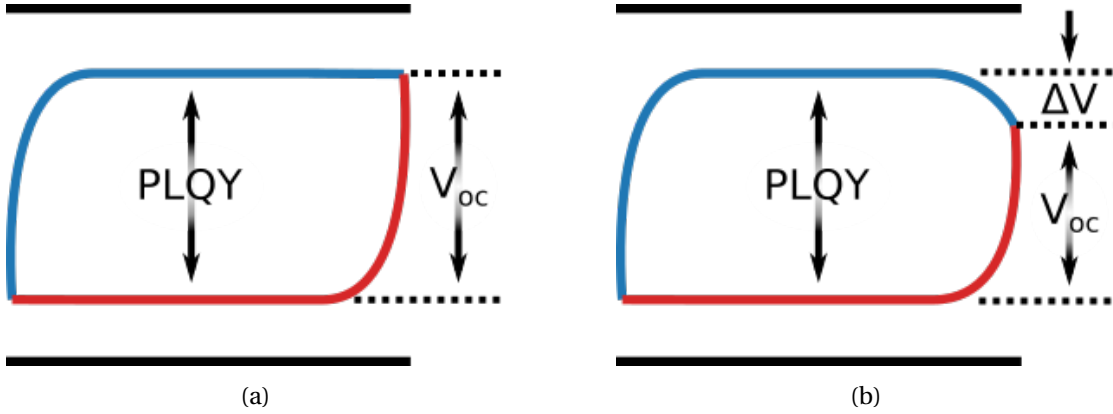


Figure 5.1 – Visualization of how PLQY and  $V_{oc}$  can diverge. (a) With flat quasi-Fermi levels the  $V_{oc}$  and quasi-Fermi level splitting are the same. (b) However, when the quasi-Fermi levels bend they differ.

The  $J_{sc}$  is a measure of the charge extraction. Again, this is partly determined by recombination in the cell, particularly that at the transport layer interfaces. The mobile ions that collect at the interfaces and add to the recombination there can also create a Debye layer that screens the potential across the cell, as was discussed in Ch. 4 [160]. Another significant cause of  $J_{sc}$  losses is if the transport layers are aligned outside the band gap, creating an energy barrier for charge extraction. Other factors can also play into  $J_{sc}$  losses. For instance, short diffusion lengths in a thick perovskite layer would prevent many charges from reaching the transport layers.

Finally, the fill factor gives a measure of the resistive characteristics of the cell. To understand this we can use a simple circuit model of a solar cell consisting of a current source, photodiode, shunt resistor, and series resistor. The diagram of this model is shown in Fig. 5.2a, where  $R_s$  is the series resistance and  $R_{sh}$  is the shunt resistance. If the series resistance increases a larger voltage drop appears across it, reducing the voltage drop across the diode. Thus for the same current moving through the system a lower voltage will be present across the diode. Conversely, if the shunt resistance decreases more current will flow through it. Thus for the same voltage across the diode, a lower current will be measured. The idealized effect of both of these variations is seen in Figs 5.2b and 5.2c. In modern perovskite cells low shunt resistances do not pose a significant issue compared to those created by high series resistances [161]. High series resistances can arise from poor charge transport in the perovskite layer itself, or from low charge mobilities or density of states in the organic charge transport layer. We saw that poor charge transport in the perovskite layer also affects both the  $V_{oc}$  and  $J_{sc}$ , showing the entanglement of the characterization parameters and their underlying mechanisms.

In addition to these three standard characterization parameters, we can also calculate the

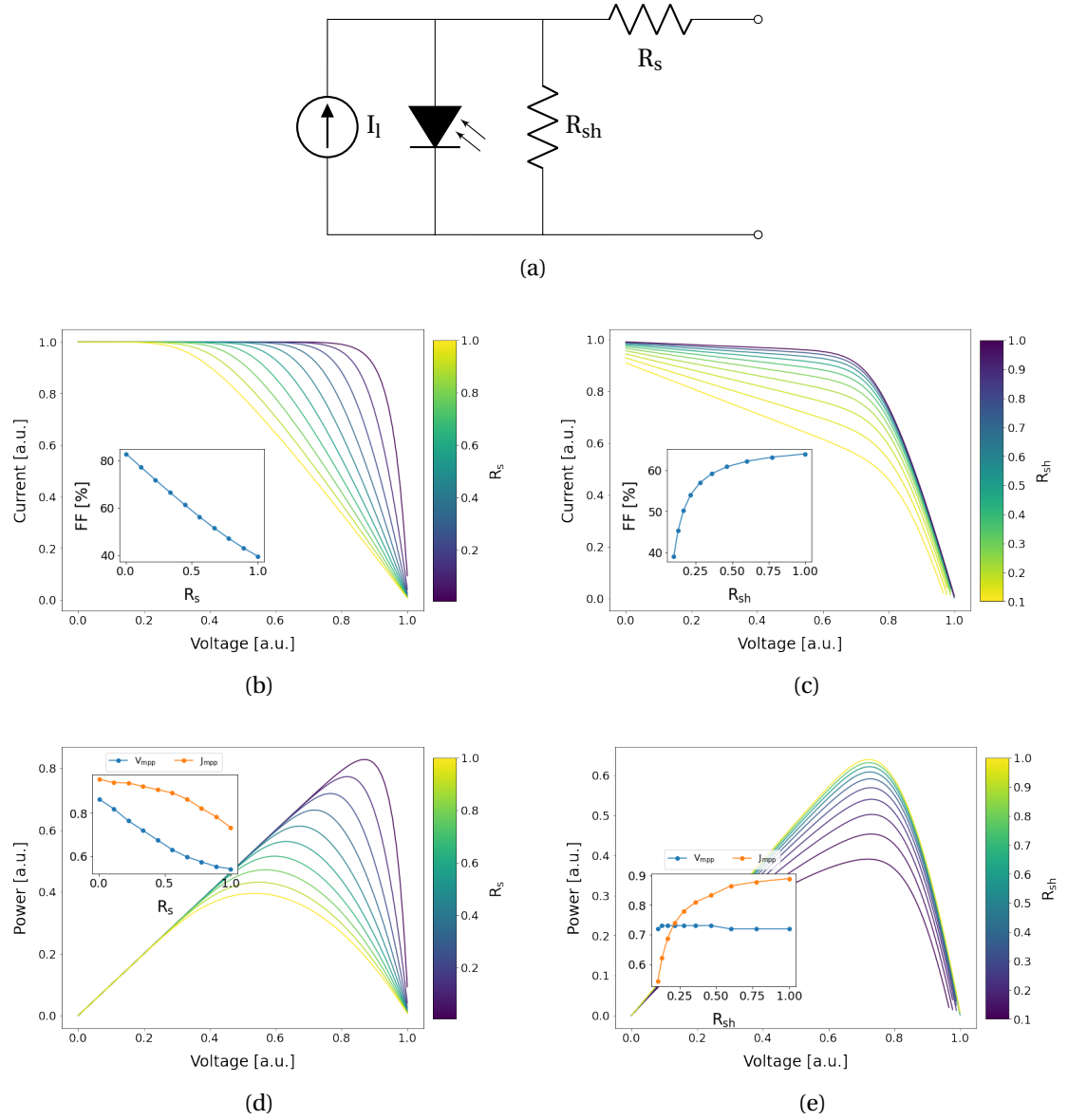


Figure 5.2 – (a) Circuit diagram of a basic solar cell model consisting of a current source  $I_l$ , photodiode, shunt resistor  $R_{sh}$ , and series resistor  $R_s$ . (b, c, d, e) Effect of varying the (b, d) series resistance  $R_s$  and (c, e) shunt resistance  $R_{sh}$  values on JV curves and their characteristic values. Insets show the effect on fill factor or  $V_{mpp}$  and  $J_{mpp}$ . Resistances have arbitrary units.

ideality factor  $n_{id}$ , which reveals information about the type of recombination taking place.

$$I = I_l - I_0 \left[ \exp \left( \frac{\beta e V}{n_{id}} \right) - 1 \right]$$

where  $I_l$  is the photocurrent,  $I_0$  is the diode saturation current,  $\beta = 1/k_B T$  is the coldness, and  $e$  is the electric charge. Measuring the ideality factor can be done in two ways. It can be measured directly by fitting the JV curve and using  $n_{id}$  as a fitting parameter. However this has the drawback that it is sensitive to poor charge transport that may exist in the cell stack [162]. The alternative way to measure it is to measure the  $V_{oc}$  at varying light intensities, which gets around the charge transport issue. In traditional semiconductors an ideality factor of 1 indicates bimolecular radiative recombination is occurring, while an ideality factor of 2 is indicative of monomolecular non-radiative recombination, usually dominated by SRH recombination at typical illumination intensities. A value between 1 and 2 indicates the relative strengths of each of these recombination mechanisms. However, perovskites, being the complex material they are, have a more complicated explanation of their ideality factor [162]. Because of the strong non-radiative interface recombination present in perovskites the assumptions that lead to these classic results are broken. Instead, the ideality in perovskites likely points to the type of recombination occurring at the point where it is most dominant which is typically the charge transport layer interfaces. All this being said, the actual meaning of the ideality factor in perovskite solar cells is a bit murky. Owing to their low charge mobilities but relatively high photocurrents the ideality factor begins to lose its physical meaning and an interpretation of its value can become quite convoluted [159].

Despite the complexity of interpreting both the PLQY and JV characterization parameters in any absolute way, the trends they present may still prove insightful. To explore this, high quality FAPbI<sub>3</sub> cells with OAI were prepared with varying HTLs [163]. temperature dependent JV and PL measurements were then performed at several light intensities.

An example of the JV plots is shown in Fig. 5.3. There are a few things to notice here immediately. The first is that there seems to be a quite abrupt change in the shape of the JV curve around 260 K. While the short-circuit current ( $J_{sc}$ ) and open-circuit voltage ( $V_{oc}$ ) remain relatively constant, the curve flattens sharply with temperature. This should be present when analyzing the fill factor. The traces for each of these characterization parameters versus temperature for every sample is seen in Fig 5.4 and shows that these are indeed general trends. Focusing on how the JV curve changes shape we can see that it begins to flatten, but quickly takes on an S-curve. Notice that the flattening occurs by the bend of the curve shifting towards  $V = 0$ . As discussed and demonstrated in Fig. 5.2b, this is caused by an increase in the series resistance. In Chapter 2 we saw a similar S-curve appear that was caused by band bending at the interface in the optimized model of the tin perovskite in Fig. 2.11a [127, 128]. Both of these pieces of evidence point to an increased resistance to charge transport at the charge transport layers. The two materials used for charge transport here are TiO<sub>2</sub> and Spiro-OMeTAD (spiro). Considering that spiro, given its organic nature, is likely more sensitive to changes in temperature than the inorganic TiO<sub>2</sub>, it is likely the culprit. We will consider this in further

detail later.

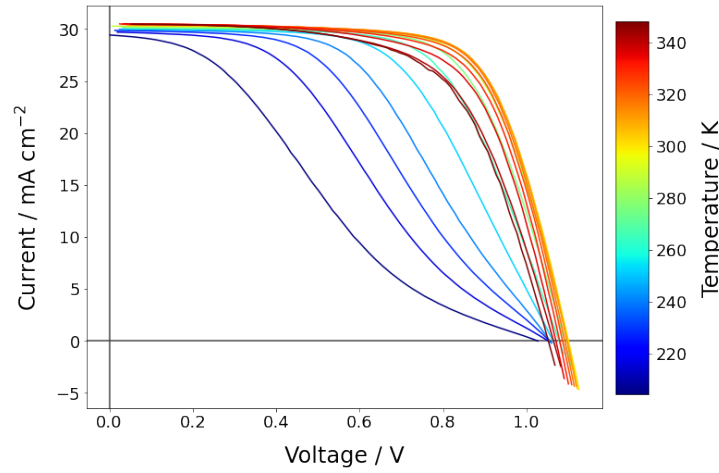


Figure 5.3 – Example of the JV curves as a function of temperature.

From the JV measurements the standard characteristic parameters at each temperature and intensity were calculated:  $J_{sc}$ ,  $V_{oc}$ ,  $J_{mpp}$ ,  $V_{mpp}$ , fill factor (FF), and efficiency (PCE,  $\eta$ ). An example of these is seen in Fig. 5.5. Note that for the current density, the exact size of the illumination area is not known, and so was approximated to calculate the current density from the measured current. In addition to the standard characterization parameters, the ideality factor  $n_{id}$  was calculated from the intensity dependence of the open circuit voltage as

$$n_{id} = e\beta \frac{dV_{oc}}{d(\ln I)}$$

where  $e$  is the electric charge and  $\beta = 1/k_B T$  is the coldness [164]. An example of this is seen in Fig. 5.6.

Examples of the PL measurements for a single device are seen in Fig. 5.7. These spectra were smoothed using a second order Savitzky-Golay filter, from which the peak position, full width at half maximum (FWHM) and integrated PL area were calculated. An example of these results is seen in Fig. 5.7b. These plots show essentially what we expect, with an interesting turning point in the integrated PL area around 310 K. This is an indication that some other recombination mechanism has come into play and could arise from the thermal instability of spiro [165]. Fig. 5.8 shows a comparison of the  $V_{oc}$  and integrated PL. As discussed before we would have hoped to have seen a linear correlation here, but we do not. This is caused by the nonlinear change in the  $V_{oc}$  combined with the two regimes of the PL area. In a simple ideal situation the  $V_{oc}$  would be proportional to temperature, and the integrated PL area would be exponential in temperature. This deviation, especially the non-linearity in the  $V_{oc}$ , further strengthens the claims made that the two may be uncoupled due to non-constant quasi-Fermi levels in the perovskite material.

In an attempt to separate the effects of the HTL from the bulk of the perovskite for the spiro

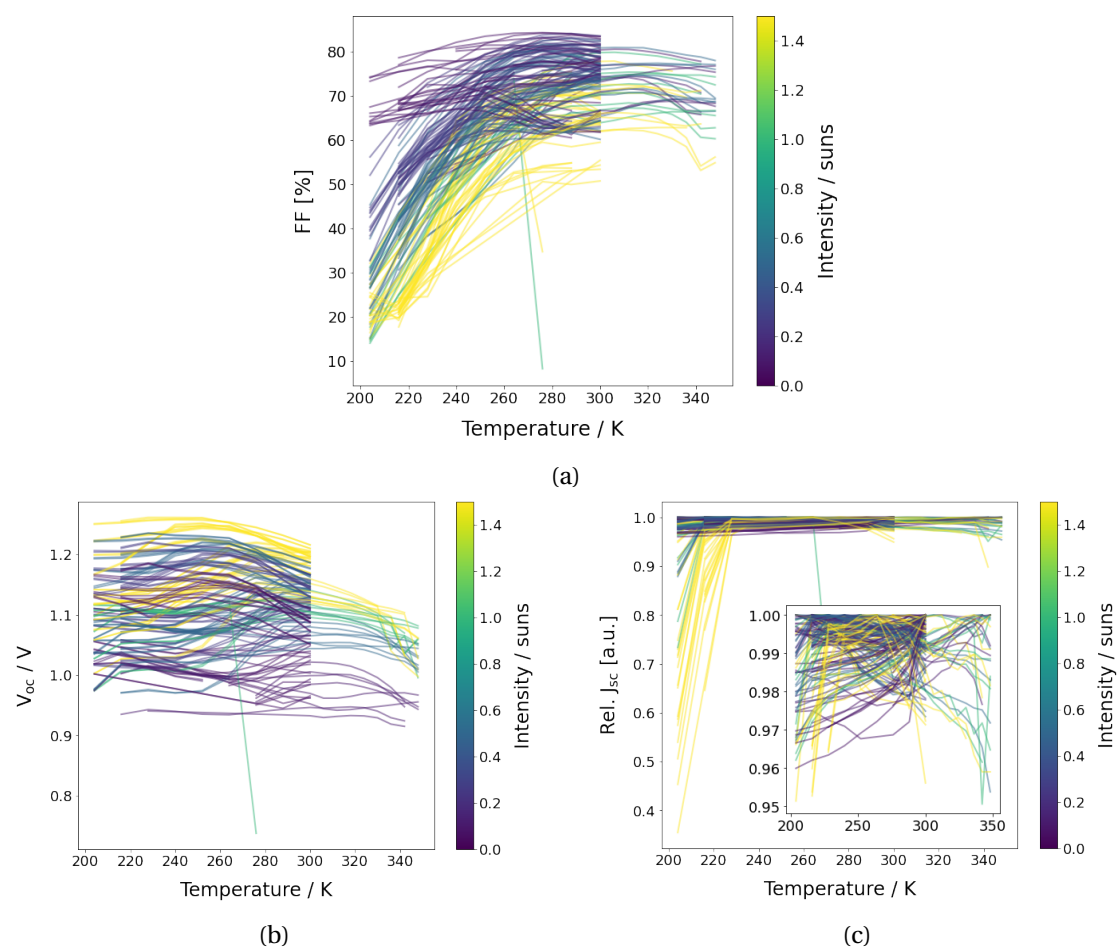


Figure 5.4 – The calculated (a) fill factor (FF), (b)  $V_{oc}$ , and (c) normalized  $J_{sc}$  vs temperature traces for every measurement with intensity larger than 0.5 sun illumination. The inset in (c) is a zoomed version of the same data.



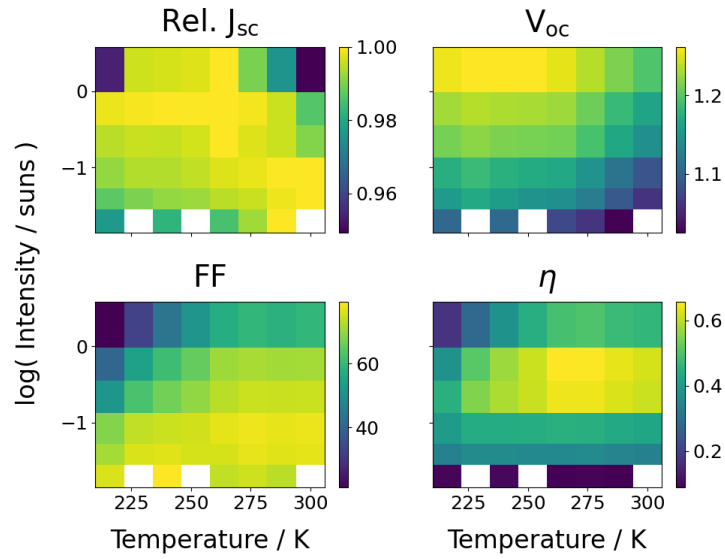


Figure 5.5 – Example of calculated JV parameters. The short-circuit current density is relative to better show the trends because the absolute values change linearly with intensity. Units of the plots are: Rel.  $J_{sc}$  has arbitrary units normalized to the maximum current for each level of illumination,  $V_{oc}$  is in Volts, FF is in percent, and the efficiency  $\eta$  is also in percent.

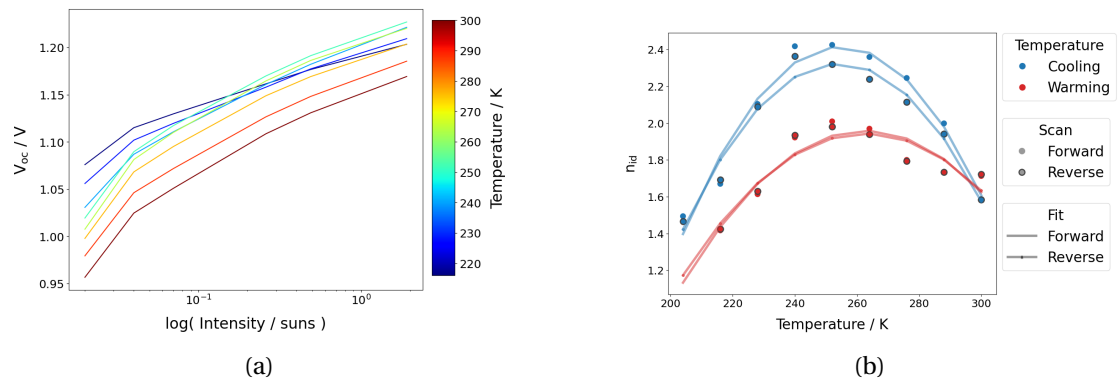
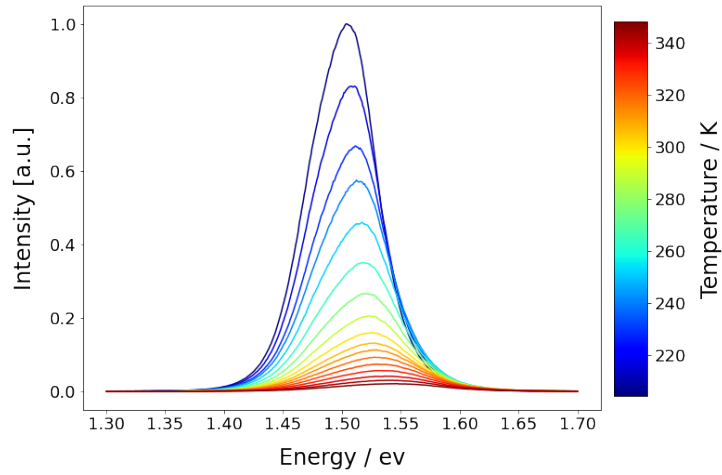
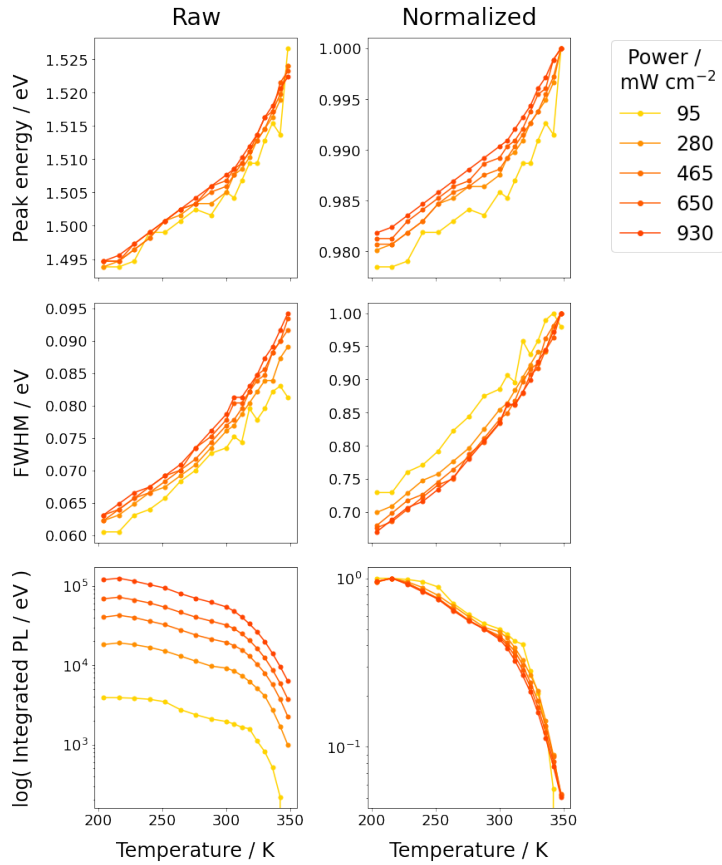


Figure 5.6 – (a) Example of open circuit voltage vs. intensity at various temperatures, used to calculate ideality factor. (b) The calculated ideality factors along with cubic fits. While this data looks quadratic, other data had a cubic shape.



(a)



(b)

Figure 5.7 – (a) Example of the raw PL spectra at various incident powers and temperatures. (b) The calculated PL parameters and the same data normalized to the maximum value for easier comparison.

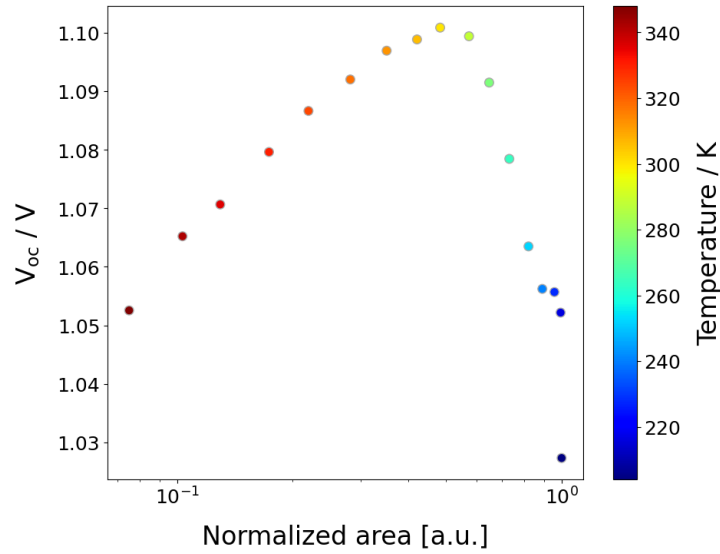


Figure 5.8 – Example of a correlation of the  $V_{oc}$  and integrated PL area.

samples, JV scans of spiro were taken at various temperatures. This allows us to calculate the conductivity, or conversely resistivity, of the spiro against temperature. An example of these scans and the resulting conductivity measurements are seen in Fig. 5.9. The resistance of each scan is calculated from  $R = V/I$ . The conductivity is then calculated by accounting for the geometric factor of the samples which had a cross section of (10 mm x 500 nm) and a length of 200  $\mu\text{m}$ .

$$\sigma = \frac{200\mu\text{m}}{10\text{mm} \times 500\text{nm}} \frac{1}{R}$$

In Fig. 5.2a we can take the resistance of the spiro layer into account by considering the series resistance  $R_s$ . Unfortunately, using the calculated values of the spiro conductance leads to voltage drops across it that are wildly out of proportion, greatly exceeding the applied voltage. The likely cause of this is that the conductivity measurements of the spiro were performed on a lateral sample across a 200  $\mu\text{m}$  distance, while the spiro thickness on the sample is around 150 nm. This thousand-fold difference between the layers thicknesses would also create a thousand-fold difference in the applied electric fields. This likely induces non-linear effects in the spiro layer, making the conductivity measurements invalid for use on the solar cell.

While we were able to see some qualitative trends appear when comparing JV and PL parameters, it is still difficult to draw solid conclusions from the results. In general, we saw how difficult it is to disentangle the meaning and causes of each of these parameters and how they correlate with each other. However, by trying to connect the phenomenon seen across these measurements we should be able to form a stronger idea of what is happening internally. This is especially true when performing temperature dependent measurements because the dominant mechanisms within the material change. Given the potential usefulness of this sort

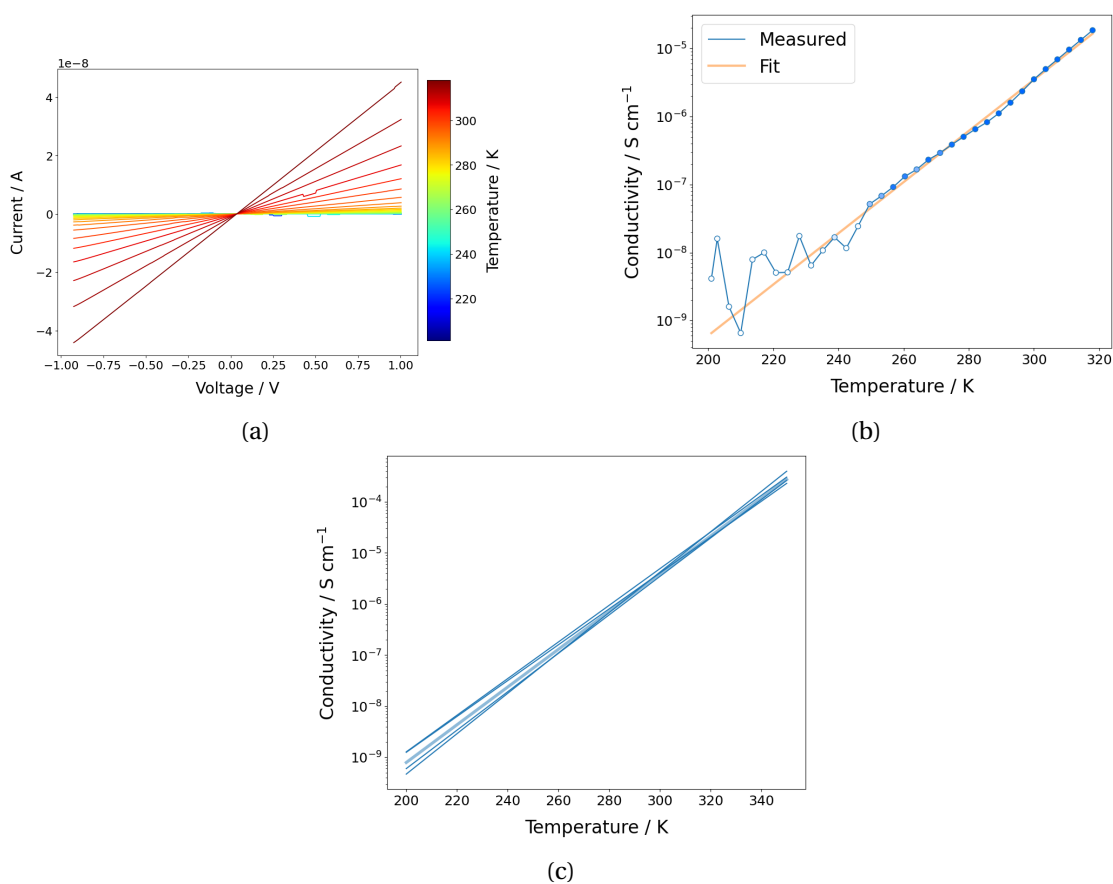


Figure 5.9 – (a) Raw JV scans of spiro-OMeTAD at various temperatures. (b) Calculated conductivity from the JV scans. The opacity of the points indicates their relative error, with more transparent having a larger error. (c) Exponential fits of all conductivity experiments, along with the mean fit.

of characterization, it seems worthwhile to continue investing time towards understanding the results it produces.

The goal of this study was to combine the results of JV scans with PL spectra to obtain additional information that would not be available from them individually. To do this we performed simultaneous temperature dependent JV and PL experiments. By comparing the JV results with a simple circuit model we found traces of both an increase in series resistance, and a decrease in shunt resistance. An S-curve also appeared at lower temperatures indicating an extraction barrier. When examining the PL area, two regimes appeared, with the boundary around room temperature. Finally, an attempt to combine information from the JV curve, namely the  $V_{oc}$ , and PL spectra, namely the integrated area, found that the two are related in a non-linear manner. This points to there being significant band bending in the material near the interfaces, causing this divergence of behavior.



## 6 Conclusion

While perovskite solar cells show promise to contribute towards sustainable energy, there are still many hurdles that need to be overcome before they can be commercialized. To overcome these hurdles it is important to understand their underlying causes so they can be addressed in a systematic way. Optical and electrical analysis give us a peek into these causes by providing us macroscopic information about these microscopic phenomenon. It is this change in abstraction level that makes it difficult to interpret the data resulting from these measurements.

Throughout this thesis an attempt has been made to attribute the phenomenon observed from these measurements. In Chapter 2 we explored the causes for the significant difference between the ideal and measured open-circuit voltage for a tin-based perovskite cell optimized for short-circuit current. Using numerical models we found that the main cause for this drop was due to the misalignment of the  $\text{TiO}_2$  electron transport layer (ETL) and the conduction band of the perovskite cell. In addition, the interface defects present at the ETL posed a significant hindrance to the cell. The impact of the misalignment has also been confirmed by others in real-world experiments, showing not only the validity of these somewhat basic modeling approaches, but also the need to focus on novel transport layers.

In Chapter 3 we examined another lead-free perovskite,  $\text{Cs}_2\text{AgBiBr}_6$  – a double perovskite. We began by measuring the PLQY at room temperature, then performed temperature dependent PL experiments. By scaling the temperature dependent PL we were able to calculate the temperature dependent PLQY. This revealed sigmoidal curves for each of the major PL characteristic properties – PLQY, full width at half max, and peak position. These trends were also reported in a study by Schade, however the key temperatures are significantly different [147]. This could have been caused by the difficulty obtaining the actual cell temperature during the experiments.

Chapter 4 examined the causes and effects of reversible degradation in two different scenarios. Section 4.1 elaborated on an experiment by Domanski *et. al.* [105] in which we varied the applied voltage across a cell during a rest period which separated MPP tracking periods. We

found that by varying this hold voltage we could directly control the transient behavior of the cell as it re-entered the MPP tracking phase. This further supports the finding that it is ionic movement causing this behavior. To further explore this space the composition of the material and illumination condition during the hold voltage periods were changed. Variations in the composition revealed a significant dependence of the transient behavior on the cation ratio of MA to FA while the halogen ratio of I to Br showed a much less certain effect. When varying the illumination condition during the hold period – either leaving the cells illuminated, or placing them in the dark – the cells showed essentially the same characteristics. This indicates that the mechanisms driving the recovery of the reversible degradation are voltage driven and not significantly influenced by illumination. We then turned our attention to how this reversible degradation plays out in real-world conditions by subjecting a perovskite cell to a representative sampling of temperature and illumination conditions from a weather station. Here a new method for separating reversible and irreversible degradation was proposed using only intraday measurements. Using this, we found that while the amount of irreversible degradation grows with the total degradation, the irreversible degradation remains constant. This points to two separate mechanisms being responsible for the two types of degradation. We were also able to confirm the previous findings that temperature has an orders of magnitude more significant effect on degradation than does the illumination intensity, within a 1 sun range.

Finally, an attempt to combine information from current-voltage (JV) scans and PL spectra was made. Performing temperature dependent measurements of both types allowed us to qualitatively pick out possible mechanisms at play. By comparing the changes in the JV curves to that of a simple circuit model, we found aspects of both series and shunt resistance changes. In addition, a significant S-curve became present, indicating a misalignment between the perovskite and transport layer. Examining the integrated PL spectra showed two regimes with the transition occurring around room temperature. By comparing the open-circuit voltage and integrated PL, a non-linear trend was found, pointing to significant band bending occurring at the interfaces.

Many of these experiments were performed over an extended time frame and required several pieces of hardware to be coordinated. This was facilitated by the design of the experimental setup in a modular way that allowed for automation. Many pieces of software were developed to perform these experiments. A listing of the developed libraries can be found in Appendix B. Many of these software are now also used in other labs.

While perovskite solar cells have made significant progress in the last 10 years, much of the initial focus was oriented towards increasing efficiency. Now that these solar cells are approaching their fundamental efficiency limits and have proven they have the potential to compete with traditional solar technologies, we have seen a diversification in research directions.

One of the major focuses has been to remove lead from the devices. Tin-based and double



perovskites have become staples in this field. Unfortunately, these technologies suffer from their own hindrances. The lack of stability of tin-based cells is currently their largest hurdle to overcome. The fragility of tin-cells, not only to the environment, but also due to self-doping, shows that significant progress must be made in order for these cells to reach a point of commercialization [115]. Self-doping may be aided with the advent of new transport layers or passivation techniques, however answers have not yet been quick to come. Improved encapsulation will also aid in this endeavor, however, without the intrinsic stability of the cell at a satisfactory level, encapsulation will likely not be enough on its own. Due to these issues, it may be a significant amount of time before tin-based cells reach the commercial market, if they ever do.

Double perovskites, on the other hand, I believe show more promise due to their intrinsic stability [166]. While they have significant drawbacks, including a larger band gap which decreases their efficiency, and require more expensive materials than other perovskite variations, I believe the benefits of high tunability and stability make up for this. Even if they only find niche applications, double perovskites show promise to become an important part of the commercial market. Research on these materials is still young though, leaving the road open for significant improvements.

Many strides have been made in understanding the fundamental mechanisms at play in the classic lead-based perovskite variations. However, a comprehensive and detailed theory accounting for the specifics of the mechanisms at play is still elusive. This comes from the intrinsically complex behavior exhibited by perovskites. As we chip away at these details the insights will help build more accurate models of the materials. With the rise of big data and artificial intelligence, these improved understandings could play an important role in modeling novel perovskite systems, allowing for high throughput predictions. Using these predictions to guide further research would accelerate the quest to find perovskites with suitable properties for a given application.

While perovskites could make a significant impact in the solar energy space, other applications may guide research along the way. Niche applications for the material – such as flexible electronics, scientific instruments, or as computational units – will pave the way for larger scale commercialization [167, 168]. It is also with these niche applications in mind that we will see continuing renewed interest in perovskites from a commercial point of view, helping drive further research.

While the history of perovskite solar cells is still young, rapid progress has been made. As the first hurdles of efficiency have been conquered, the more difficult task of understanding the material's dynamic behaviors have remained. It is here that the focus has shifted, and should remain for some time, until the material can be used in a more reliable manner. As we continue to make strides towards a fundamental understanding of perovskite's behaviors and their causes, a feedback loop into the applications of these theories will provide incremental improvements. This slow opening of the material to newer and broader commercial oppor-

tunities will surely drive it's adoption as we move into an age of more complex and dynamic technology.

## A Temperature calibration

Unfortunately the temperature measurements of the cryostat were incorrect due to poor thermal coupling between the sample holder and the sample, so the actual temperatures of the samples are unknown. To approximate the actual temperature of the perovskite a calibration experiment was performed, and the measured temperatures were calibrated using this data.

A high quality  $\text{FAPbI}_3$  with OAI perovskite was deposited on the two substrates used for experiments – microscope glass, and FTO glass – as well as an aluminum substrate [169]. The samples were then arranged in different orientations to calibrate the temperature for each that was used in an experiment. Fig. A.1 shows the different orientations.

To perform the calibration the photoluminescent (PL) spectra at various temperatures was taken. For each sample the peak position was then plotted, an example of which is seen in Fig. A.2. Notice that the perovskite on aluminum has a very distinct shape, with a change in peak position direction occurring at roughly 150 K. This is caused by a phase change in the perovskite from  $\alpha$  to  $\beta$  phase [170]. The peak position curves were then smoothed using a second degree Savitsky-Golay filter.

We assume that the measurement perovskite before any cooling has occurred is at 300 K. We then use the turning point of each spectra as marked by the vertical lines in Fig. A.2 as a reference point for the temperature, assuming it occurs at 150 K. Using a second order Savitsky-Golay filter the peak position curves were smoothed and the temperatures were calibrated using a linear transformation such that the 300 K remained fixed and the turning

point was scaled to 150 K.

$$C(T) = \frac{T - d_{\text{lower}}}{d_{\text{upper}} - d_{\text{lower}}} (r_{\text{upper}} - r_{\text{lower}}) + r_{\text{lower}}$$

$$\begin{aligned} C(T) &= (T - d_{\text{lower}}) \frac{d_{\text{upper}} - d_{\text{lower}}}{r_{\text{upper}} - r_{\text{lower}}} + r_{\text{lower}} \\ &= (T - d_{\text{lower}}) S + r_{\text{lower}} \end{aligned}$$

where  $C(T)$  is the calibration temperature and  $T$  is the measured temperature.  $d_{\text{lower}}$  and  $d_{\text{upper}}$  are the lower and upper set points of the input domain. In this case  $d_{\text{lower}}$  is the measured temperature of the turning point for each experiment, and  $d_{\text{upper}}$  is 300 K. Similarly  $r_{\text{lower}}$  and  $r_{\text{upper}}$  are the upper and lower set points of the desired range. In this case  $r_{\text{lower}}$  is 150 K, and  $r_{\text{upper}}$  is 300 K. The second version of the equation is regrouped in order to simplify the function where  $S = (d_{\text{upper}} - d_{\text{lower}}) / (r_{\text{upper}} - r_{\text{lower}})$  is the scaling factor. The results of this scaling for each substrate are seen in Fig. A.3. The marked turning points for the glass samples are offset from 150 K due to the smoothing of the curves.

The second form of  $C(T)$  was used as the calibration function parameterized by  $S$  and  $r_{\text{lower}}$  to correct the measured temperature.  $S$  and  $r_{\text{lower}}$  for the *perovskite on glass* and *perovskite on FTO* orientations are shown in Table A.1.

	$S$	$r_{\text{lower}}$
Glass	5/7	90
FTO	3/5	50

Table A.1 – Parameters for each substrate for the temperature calibration function.

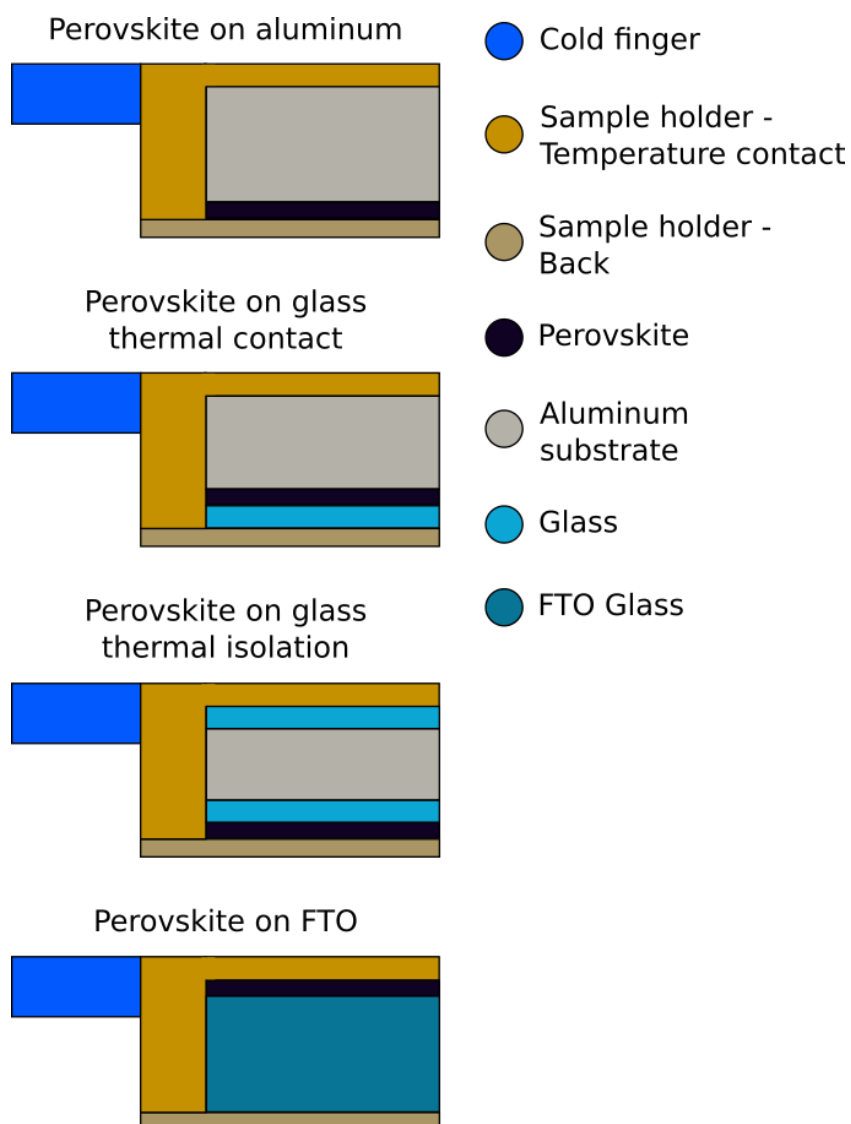


Figure A.1 – Schematic showing the different substrates and orientations used for the calibration experiments.

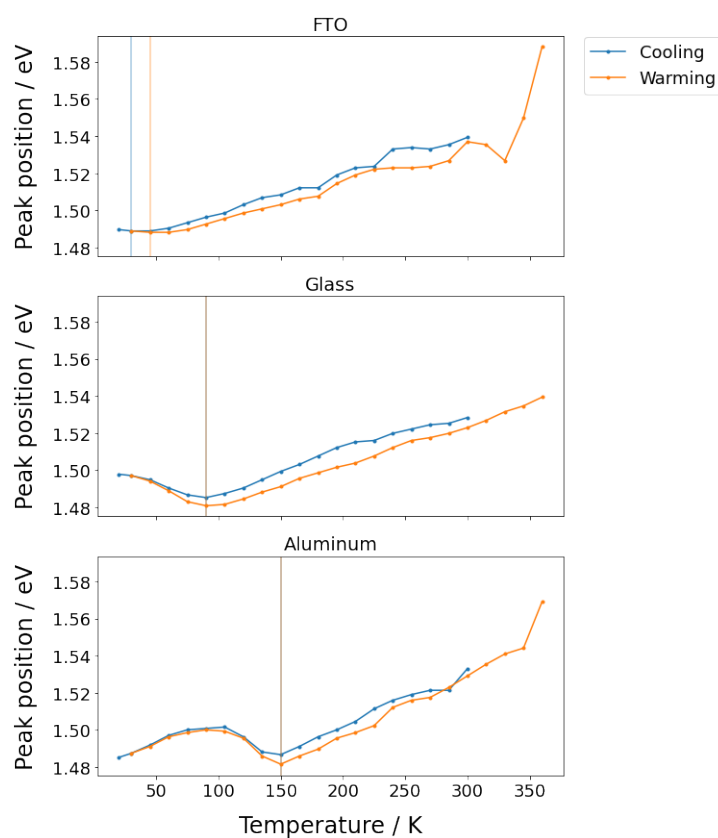


Figure A.2 – Peak position as a function of measured temperature for the perovskite on glass with thermal contact, FTO, and aluminum. The vertical lines show the turning point for each trace.

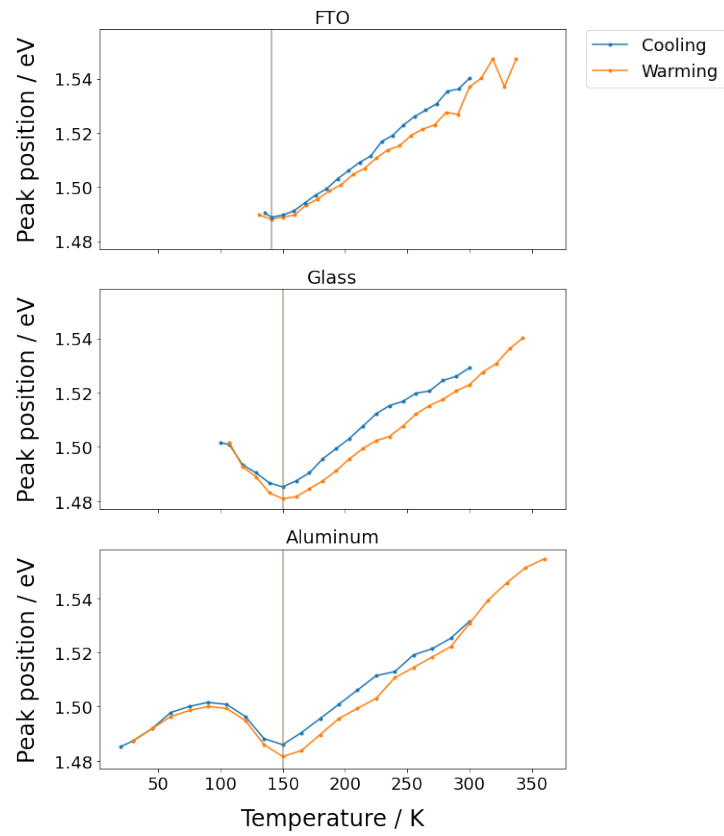


Figure A.3 – Peak positions after calibration using the method described.





## B Software listing

### Analysis Libraries

- **GitHub:** <https://github.com/bicarlsen/analysis-libraries>
- **PyPI:** <https://pypi.org/project/bric-analysis-libraries/>

A Python package of data analysis functions used throughout the course of my research. Functionality includes the ability to parse data from different hardware devices and software programs, and general analysis tools for PL and JV data.

### SCAPS-1D

- **GitHub:** <https://github.com/bicarlsen/pyscaps>
- **PyPI:** <https://pypi.org/project/pyscaps/>

A Python package for analyzing SCAPS-1D models and simulation results. This is part of the Analysis Libraries package as well, but was made independent for convenience.

### Biologic

- **GitHub:** <https://github.com/bicarlsen/easy-biologic>
- **PyPI:** <https://pypi.org/project/easy-biologic/>

Biologic create potentiostats and galvanostats, however their builtin functionality is quite limited. This Python package gives programmatic control over Biologic devices to create custom procedures.

## SCPI

- **GitHub:** <https://github.com/bicarlsen/easy-scp>
- **PyPI:** <https://pypi.org/project/easy-scp/>

A low level Python library for communication with hardware using the Standard Commands for Programmable Instruments (SCPI) protocol.

## Keithley 2400 MPP Tracking

- **GitHub:** [https://github.com/bicarlsen/keithley2400\\_mpp](https://github.com/bicarlsen/keithley2400_mpp)

A maximum power point tracking program for a Keithley 2400 Source Measure Unit (SMU). Uses a step and probe algorithm.

## Keithley 6485 Picoammeter

- **GitHub:** <https://github.com/bicarlsen/keithley-picoammeter-controller>

A Python package for controlling and communicating with a Keithley 6485 Picoammeter.

## Tektronix PWS4305

- **GitHub:** <https://github.com/bicarlsen/tektronix-pws4305-controller>

A Python package for programmatically controlling a Tektronix PWS4305 programmable DC power supply.

## Flare Pulsed Laser Controller

- **GitHub:** <https://github.com/bicarlsen/flare-laser-controller>

A Python package for controlling a Coherent Flare pulsed laser. Includes a controller and user interface.

## OBIS Laser Controller

- **GitHub:** [https://github.com/bicarlsen/obis\\_laser\\_controller](https://github.com/bicarlsen/obis_laser_controller)

- **PyPI:** <https://pypi.org/project/obis-laser-controller/>

A Python package for controlling OBIS LS/LX lasers.

## Oriel Cornerstone 260 Monochromator

- **GitHub:** <https://github.com/bicarlsen/oriel-cornerstone-260>
- **PyPI:** <https://pypi.org/project/oriel-cornerstone-260/>

A Python package for controlling an Oriel Cornerstone 260 monochromator.

## CryoCon Temperature Controller

- **GitHub:** <https://github.com/bicarlsen/cryocon-22c-controller>
- **GitHub:** <https://github.com/bicarlsen/cryocon-controller-interface>
- **PyPI:** <https://pypi.org/project/cryocon-22c-controller/>

A package for programmatically controlling a CryoCon 22C cryogenic temperature controller. Includes a programmatic and GUI interface.

## Andor PLQY

- **GitHub:** [https://github.com/bicarlsen/andor\\_plqy](https://github.com/bicarlsen/andor_plqy)

An Andor Basic (ABasic) program to automate PLQY measurements using an Andor Kymera 193i spectrometer.

## LED Array Controller

- **GitHub:** <https://github.com/bicarlsen/led-array-controller>

GUI interface for controlling a custom built LED array using a Tektronix PWS4305 as the power supply.

## LED Solar Simulator

- **GitHub:** <https://github.com/bicarlsen/solio-solar-simulator>

- **PyPI:** <https://pypi.org/project/bric-solar-simulator/>

Controller and interface for a custom solar simulator. The controller is a Python library and the GUI interface was built using PyQt5.

## Arduino Controllers

- **GitHub:** <https://github.com/bicarlsen/bric-arduino-controllers>
- **PyPI:** <https://pypi.org/project/bric-arduino-controllers/>

A variety of low and high level Arduino libraries used to control custom hardware and trigger standard hardware for synchronization.

## Sample Holder

- **GitHub:** <https://github.com/bicarlsen/rotary-sample-holder-controller>

A PyQt5 GUI used to control a custom built sample holder for high throughput photoluminescence measurements.

## C Thot: Data management and analysis

- <https://github.com/thot-data>
- <https://thot-data.com/>

Thot was born out of the need to better organize and analyze research data. Throughout my research, intersample variability created issues when analyzing data. This led me to take a statistical approach towards my experiments. Very quickly, however, the amount of data I was collecting became overwhelming to manage. Thus I began to automate the organization and analysis process.

Thot adheres to two fundamental principles:

- Data integrity, and
- Modular analysis

**Data integrity** means that data can never be modified or overwritten, it can only be read and created. This means that no original data is ever lost, and the analysis process can be traced from the original data to the final conclusion. **Modular analysis** combines the DRY (do not repeat yourself) coding principle with the separation of data and the analysis. Using Thot, each step of an analysis is broken into its own self contained module. These modules are then arranged to create an analysis pipeline. This allows analysis modules to be easily shared and re-used across projects. This also allows modules to be inserted or removed from the pipeline dynamically. Because the analysis modules are separate from the specific data, new data or analysis can be added to a project at any time.

To implement these principles Thot creates a structured database using a recursively defined tree structure. The root of each subtree has access to all the data in its subtree, but not to the data of any siblings or ancestors. This allows the same analysis modules to be applied to multiple subtrees without having data contamination between the subtrees.



## **D Instrument listing**

Throughout my research only three pieces of equipment were heavily used. The instrument details listed here are the ones used throughout the thesis.

### **Spectrometer**

The spectrometer used to acquire photoluminescent spectra was a Andor Kymera 193i with an open electrode iDus 420 (A-DU420A-OE) sensor.

### **Autolab**

To acquire JV curves a Metrohm Autolab PGSTAT302N potentiostat/galvanometer was used.

### **Cryostat**

The cryostat used for temperature control was a closed loop, helium ARS CS202-DMX-1AL cryostat with an ARS-4HW compressor, a Cryocon 22C PID temperature controller, and a custom sample holder.





# E Attributions

## **Tin perovskite (Ch. 2)**

Cells were prepared by Hong Zhang. Measurements were performed in collaboration with Felix Eickemeyer. All data analysis was performed by me.

## **Double perovskite (Ch. 3)**

Cells were prepared by Maximilian Sirtl . All experiments and data analysis was performed by me.

## **Reversible degradation and ionic movement (Sec. 4.1)**

Cells were prepared by Essa Alharbi and Viktor Škorjanc. Viktor's work was part of an MSc. project under my supervision. The experiments and data analysis were carried out in collaboration between myself and Viktor.

## **Degradation in the real world (Sec. 4.2)**

Main experimental work was carried out by Konrad Domanski and Wolfgang Tress. Data analysis was performed by me. Main results were published in the article *Performance of perovskite solar cells under simulated temperature-illumination real-world operating conditions* [171].

## **Temperature dependence of photoluminescent and electronic properties (Ch. 5)**

Cells were prepared by Haizhou Lu. All experiments and data analysis were performed by me.

## **Funding**

Financial support was provided by an Ambizione Energy fellowship (PZENP2\_173617) through the Swiss National Science Foundation.

## **F Fabrication methods**

### **F.1 Standard superstrate preparation**

Fluoride-doped tin oxide glass substrates (FTO, 4.0 mm-thick,  $10\ \Omega/\text{sq}$ , Nippon Sheet Glass) were patterned using zinc powder and diluted hydrochloric acid (1 - 4 M). The patterned FTO was sequentially cleaned in commercial detergent solution (Hellmanex, 2 vol% in water), deionized (DI) water, ethanol, and acetone baths together with ultrasonic for 15 min. Finally, the substrates were rinsed with DI water, followed by air drying. After ultraviolet (UV) ozone treatment for 15 min, a 20-40 nm-thick compact  $\text{TiO}_2$  (c- $\text{TiO}_2$ ) was deposited on the cleaned FTO substrate by spray pyrolysis at  $450\ ^\circ\text{C}$  using a precursor solution of titanium diisopropoxide bis(acetylacetonate) (75 wt.% in isopropanol), which was diluted in ethanol (volume ratio of 1:9) together with the addition of acetylacetone (4 vol%). The carrier gas for the spray pyrolysis was oxygen. After cooling down to room temperature and UV ozone treatment for 15 min, the mesoporous  $\text{TiO}_2$  (mp- $\text{TiO}_2$ ) was spin coated onto the c- $\text{TiO}_2$  coated FTO glass at 4000 rpm for 20 s. The mp- $\text{TiO}_2$  solution consisted of a commercial paste of  $\text{TiO}_2$  (Dyesol 30 NR-D) diluted in ethanol (1:6, weight ratio) in order to achieve 100-150 nm thick mp- $\text{TiO}_2$ . After application the sample was dried at  $80\ ^\circ\text{C}$  for 10 min.

### **F.2 Standard device contact deposition**

The perovskite covering the negative contact is removed by first using a razor to scratch it off and then cleaned using MeCN. Gold electrodes of  $\sim 80$  nm are then deposited by thermal evaporation.

### **Tin perovskite (Ch. 2)**

After the standard preparation described in Sec. F.1, the  $\text{TiO}_2$  films were gradually sintered at  $450\ ^\circ\text{C}$  for 30 min and cooled down to the room temperature. Before coating active layer, the films were treated with a solution of  $\text{SnCl}_4$  in DI water (40 mM) by chemical bath deposition

at 70 °C for 30 min. The substrates were then cleaned with DI water and ethanol, respectively. After, the treated mp–TiO<sub>2</sub> substrates were annealed at 180 °C for 60 min. After cooling down, the substrates were transferred into a nitrogen-filled glovebox (oxygen < 0.1 ppm) for deposition of perovskite films. The FA<sub>0.6</sub>MA<sub>0.4</sub>SnI<sub>3</sub> perovskite films were deposited onto mp–TiO<sub>2</sub> substrates from a precursor solution containing tin iodide (1 M), formamidinium iodide (0.6 M), methylammonium iodide (0.4 M), and SnF<sub>2</sub> (0.06 M) dissolved in 400  $\mu$ L dimethyl formamide (DMF) and 100  $\mu$ L dimethyl sulfoxide (DMSO). The perovskite precursors were spin coated onto the mp–TiO<sub>2</sub> substrate at 5000 rpm for 30 s. During the spin coating, 200  $\mu$ L of toluene was dropped onto the spinning substrates. The resulted perovskite films were then annealed at 100 °C for 10 min. A hole transport material (HTM) solution containing 10 mg mL<sup>-1</sup> poly(3-hexylthiophene) (P3HT) in chlorobenzene was spin coated on top of perovskite layers at 3000 rpm for 30 s, followed by annealing at 100 °C for 10 min. After the HTM deposition gold contacts were deposited on the device as describe in Sec. F2. The fabricated devices were encapsulated with commercial Butyl tape or UV glue (NOA 68, Norland products) before taking them out for IV measurements.

### Double perovskite (Ch. 3)

Cells were prepared as described in *The Bottlenecks of Cs<sub>2</sub>AgBiBr<sub>6</sub> Solar Cells: How Contacts and Slow Transients Limit the Performance* [172].

### Reversible degradation and ionic movement (Sec. 4.1)

After the standard preparation described in Sec. F1, the mp–TiO<sub>2</sub> was cleaned under ozone and UV light for 15 minutes. The standard MAPbI<sub>3</sub> perovskite solution was created from MAI and PbI<sub>2</sub> precursors with a 3% lead halide excess in DMSO to form a 1.2 M solution. The MA<sub>0.3</sub>FA<sub>0.7</sub>PbI<sub>(1-x)</sub>Br<sub>x</sub> and MA<sub>(1-x)</sub>FA<sub>x</sub>PbI<sub>3</sub> perovskites were created by mixing FAPbI<sub>3</sub>, MAPbI<sub>3</sub>, and MAPbBr<sub>3</sub> solutions in a DMF/DMSO solution to reach the desired stoichiometry with a 1.4 M solution. The solution was then heated at 60 °C until all precursors were completely dissolved.

The perovskite solution was spin coated onto the superstrate at 5000 rpm for 30 s. After roughly 20 s chlorobenzene was deposited on the film as an antisolvent. Li-doped spiro-OMeTAD is then spin coated on the perovskite at 4000 rpm for 20 s. Gold electrodes are then added to the sample using the method described in Sec. F2.

### Degradation in the real world (Sec. 4.2)

Cells were prepared as described in *Performance of perovskite solar cells under simulated temperature-illumination real-world operating conditions* [171].

## **Temperature dependence of photoluminescent and electronic properties (Ch. 5)**

Cells were prepared as described in *Vapor-assisted deposition of highly efficient, stable black-phase FAPbI<sub>3</sub> perovskite solar cells* [173].



# G Methods

## Tin perovskite (Ch. 2)

The JV scan was performed in a solar simulator using a 300 W Oriel Xenon lamp with an AM 1.5G spectral filter at 1 sun. The lamp was calibrated using a silicon reference diode certified by Newport Corporation's PV Lab. A Keithley 2400 was used for the current voltage scans at a rate of 50 mV/s. An (0.5 x 0.5) cm<sup>2</sup> mask was used over the active area of the cell. The cells were not preconditioned in any way.

Fitting the JV curve in SCAPS-1D was performed using the *curve fit* method in several rounds. In each round several parameters were allowed to vary until the model settled. Analysis of the model results was performed using the PySCAPS python library listed in Appendix B.

## Double perovskite (Ch. 3)

PLQY measurements were performed using a 422 nm OBIS LX laser inside an Gigahertz Optik UPB-150-ARTA integrating sphere. The absolute photon flux of the laser was calibrated to one sun illumination. Emitted light was collected using a 400  $\mu$ m multimodal fiber – a Thorlabs BFL44LS01. Measurements were taken using an Andor Kymera 193i spectrometer in the accumulation setting. 100 spectra were taken with each spectra integrating for 0.1 s.

During the temperature dependent PL samples were allowed to rest at each temperature for 30 minutes, starting from room temperature dropping to the lowest temperature, and then warming back up. Samples were illuminated at various powers by the same laser used for the PLQY measurements. For each spectral measurement the sample was illuminated for 15 s, then rested with the laser off for 30 s before changing the laser power. The spectrometer and its settings were the same used as with the PLQY.

### Reversible degradation and ionic movement (Sec. 4.1)

The same setup as was used in *Migration of cations induces reversible performance losses over day/night cycling in perovskite solar cells* was used, with the exception of the light source [105]. The light source was a custom built light source using various red, green, and blue Luxeon LEDs. The light source was calibrated using a spectrometer and silicon reference cell.

### Degradation in the real world (Sec. 4.2)

See *Performance of perovskite solar cells under simulated temperature-illumination real-world operating conditions* for details [171].

### Temperature dependence of photoluminescent and electronic properties (Ch. 5)

Cells were illuminated by a OBIS LX 660 nm continuous wave laser. The power of the laser was calibrated to one sun. Cells were allowed to rest at each temperature for 30 min before taking a measurement. During a PL measurement the cell was illuminated for 10 s, then rested with the laser off for 30 s before changing the laser power. After the PL measurements were complete at each temperature, JV scans were taken by a Metrohm Autolab at 100 mV/s from 0 V to  $V_{oc}$ . Illumination was provided by a custom built LED array using Luxeon LEDs and calibrated using a reference silicon cell to one sun.



# Bibliography

- [1] *Human Development Index (HDI)*. Tech. rep. United Nations Development Programme. URL: <http://hdr.undp.org/en/content/human-development-index-hdi>.
- [2] Ambuj D. Sagar and Adil Najam. “The human development index: a critical review”. In: *Ecological Economics* 25.3 (June 1998), pp. 249–264. ISSN: 0921-8009. DOI: 10.1016/S0921-8009(97)00168-7.
- [3] Julia K Steinberger. *Energising Human Development*. Tech. rep. United Nations Development Programme, 2016. URL: <https://hdr.undp.org/en/content/energising-human-development>.
- [4] Corina Pîrlogea. “The Human Development Relies on Energy. Panel Data Evidence”. In: *Procedia Economics and Finance* 3 (Jan. 2012), pp. 496–501. ISSN: 2212-5671. DOI: 10.1016/S2212-5671(12)00186-4.
- [5] F. Wagner. “EPS-SIF Energy Summer School 2019: Concluding remarks”. In: *EPJ Web of Conferences* 246 (2020), p. 00022. DOI: 10.1051/EPJCONF/202024600022.
- [6] *Energy use per person*. URL: <https://ourworldindata.org/grapher/per-capita-energy-use?tab=table>.
- [7] *Human Development Index*. Tech. rep. United nations Development Programme. URL: <http://hdr.undp.org/en/indicators/137506#>.
- [8] *Human Development Report 2020*. Tech. rep. United Nations Development Programme. URL: <http://hdr.undp.org/en/2020-report>.
- [9] Qin Li and Hongmin Chen. “The Relationship between Human Well-Being and Carbon Emissions”. In: *Sustainability 2021, Vol. 13, Page 547* 13.2 (Jan. 2021), p. 547. DOI: 10.3390/SU13020547. URL: <https://www.mdpi.com/2071-1050/13/2/547>.
- [10] Leonard Wantchekon. “Why do Resource Abundant Countries Have Authoritarian Governments?” In: *Journal of African Development* 5.2 (2002), pp. 145–176. URL: [https://www.princeton.edu/~lwantche/Why\\_Do\\_Resource\\_Dependent\\_Countries\\_Have\\_Authoritarian\\_Governments](https://www.princeton.edu/~lwantche/Why_Do_Resource_Dependent_Countries_Have_Authoritarian_Governments).
- [11] Hazem Beblawi. *The Rentier State in the Arab World on JSTOR*. 1987. URL: [https://www.jstor.org/stable/41857943?seq=1#metadata\\_info\\_tab\\_contents](https://www.jstor.org/stable/41857943?seq=1#metadata_info_tab_contents).

- [12] Douglas Fischer. “Why Carbon Dioxide Is a Greenhouse Gas”. In: *Scientific American* (2011). URL: <https://www.scientificamerican.com/article/why-carbon-dioxide-is-greenhouse-gas/>.
- [13] P. L. Meyer and M. W. Sigrist. “Atmospheric pollution monitoring using CO<sub>2</sub>-laser photoacoustic spectroscopy and other techniques”. In: *Review of Scientific Instruments* 61.7 (Sept. 1998), p. 1779. ISSN: 0034-6748. DOI: 10.1063/1.1141097. URL: <https://aip.scitation.org/doi/abs/10.1063/1.1141097>.
- [14] Chelsea Harvey. “Earth Hasn’t Warmed This Fast in Tens of Millions of Years”. In: *Scientific American* (2020). URL: <https://www.scientificamerican.com/article/earth-hasnt-warmed-this-fast-in-tens-of-millions-of-years/>.
- [15] Thomas Westerhold et al. “An astronomically dated record of Earth’s climate and its predictability over the last 66 million years”. In: *Science* 369.6509 (Sept. 2020), pp. 1383–1388. DOI: 10.1126/SCIENCE.ABA6853. URL: <https://www.science.org>.
- [16] *Global Warming*. URL: <https://earthobservatory.nasa.gov/features/GlobalWarming/page3.php>.
- [17] Scott C. Doney et al. “Ocean Acidification: The Other CO<sub>2</sub> Problem”. In: *Annual Review of Marine Science* 1 (Mar. 2009), pp. 169–192. DOI: 10.1146/ANNUREV.MARINE.010908.163834. URL: <https://www.annualreviews.org/doi/abs/10.1146/annurev.marine.010908.163834>.
- [18] David Francis Lanark and Henry Hengeveld. *Extreme Weather and Climate Change*. 1998. ISBN: 0662268490.
- [19] Allan Lavell et al. “Climate Change: New Dimensions in Disaster Risk, Exposure, Vulnerability, and Resilience”. In: *Managing the Risks of Extreme Events and Disasters to Advance Climate Change Adaptation*. Ed. by Christopher B. Field et al. Cambridge: Cambridge University Press, 2012, pp. 25–64. DOI: 10.1017/CBO9781139177245.004. URL: [https://www.cambridge.org/core/product/identifier/CBO9781139177245A014/type/book\\_part](https://www.cambridge.org/core/product/identifier/CBO9781139177245A014/type/book_part).
- [20] Jessie Guo, Daniel Kubli, and Patrick Saner. *The economics of climate change: no action not an option*. Tech. rep. Swiss Re. URL: <https://www.swissre.com/dam/jcr:e73ee7c3-7f83-4c17-a2b8-8ef23a8d3312/swiss-re-institute-expertise-publication-economics-of-climate-change.pdf>.
- [21] *Ocean Heat Content | Vital Signs – Climate Change: Vital Signs of the Planet*. URL: <https://climate.nasa.gov/vital-signs/ocean-heat/>.
- [22] *The Ocean Cannot Absorb Much More CO<sub>2</sub> | INSEAD Knowledge*. URL: <https://knowledge.insead.edu/blog/insead-blog/the-ocean-cannot-absorb-much-more-co2-4990>.
- [23] *How Much CO<sub>2</sub> Can The Oceans Take Up? | The Keeling Curve*. URL: <https://keelingcurve.ucsd.edu/2013/07/03/how-much-co2-can-the-oceans-take-up/>.

- [24] H. Teng et al. "Solubility of CO<sub>2</sub> in the ocean and its effect on CO<sub>2</sub> dissolution". In: *Energy Conversion and Management* 37.6-8 (June 1996), pp. 1029–1038. ISSN: 0196-8904. DOI: 10.1016/0196-8904(95)00294-4.
- [25] Kristy J. Kroeker et al. "Impacts of ocean acidification on marine organisms: quantifying sensitivities and interaction with warming". In: *Global Change Biology* 19.6 (June 2013), pp. 1884–1896. ISSN: 1365-2486. DOI: 10.1111/GCB.12179. URL: <https://onlinelibrary.wiley.com/doi/10.1111/gcb.12179>.
- [26] Rebecca L. Morris et al. "Large-scale variation in wave attenuation of oyster reef living shorelines and the influence of inundation duration". In: *Ecological Applications* 31.6 (Sept. 2021), e02382. ISSN: 1939-5582. DOI: 10.1002/EAP.2382. URL: <https://esajournals.onlinelibrary.wiley.com/doi/10.1002/eap.2382>.
- [27] Yu Yao et al. "The effect of reef roughness on monochromatic wave breaking and transmission over fringing reefs". In: *Marine Georesources & Geotechnology* 39.3 (2021), pp. 354–364. ISSN: 15210618. DOI: 10.1080/1064119X.2019.1702746. URL: <https://www.tandfonline.com/doi/abs/10.1080/1064119X.2019.1702746>.
- [28] Olivia Bispott and Joe Vallino. "Ocean Acidification and its effect on Phytoplankton growth". PhD thesis. University of Chicago.
- [29] *Algae might be a secret weapon to combatting climate change — Quartz*. URL: <https://qz.com/1718988/algae-might-be-a-secret-weapon-to-combatting-climate-change/>.
- [30] *Tiny plankton drive processes in the ocean that capture twice as much carbon as scientists thought*. URL: <https://theconversation.com/tiny-plankton-drive-processes-in-the-ocean-that-capture-twice-as-much-carbon-as-scientists-thought-136599>.
- [31] *Study: Plankton May Absorb Twice as Much CO<sub>2</sub> as Previously Believed*. URL: <https://www.maritime-executive.com/editorials/study-plankton-may-absorb-twice-as-much-co2-as-previously-believed>.
- [32] O. Hoegh-Guldberg et al. "Impacts of 1.5 C Global Warming on Natural and Human Systems". In: *Global Warming of 1.5° C. An IPCC Special Report on the impacts of global warming of 1.5° C above pre-industrial levels and related global greenhouse gas emission pathways, in the context of strengthening the global response to the threat of climate change*, ed. by V. Masson-Delmotte et al. 2018. URL: <https://www.ipcc.ch/sr15/chapter/chapter-3/>.
- [33] Piya Abeygunawardena et al. *Poverty and Climate Change Reducing the Vulnerability of the Poor through Adaptation*. Tech. rep. Organisation for Economic Co-operation and Development. URL: <https://www.oecd.org/env/cc/2502872.pdf>.
- [34] *Why Climate Change and Poverty Are Inextricably Linked*. URL: <https://www.globalcitizen.org/en/content/climate-change-is-connected-to-poverty/>.

- [35] Bongki Woo et al. "Residential Segregation and Racial/Ethnic Disparities in Ambient Air Pollution". In: *Race and Social Problems* 11.1 (Mar. 2019), pp. 60–67. ISSN: 18671756. DOI: 10.1007/S12552-018-9254-0. URL: <https://link.springer.com/article/10.1007/s12552-018-9254-0>.
- [36] Michael Ash and James K. Boyce. "Racial disparities in pollution exposure and employment at US industrial facilities". In: *Proceedings of the National Academy of Sciences of the United States of America* 115.42 (Oct. 2018), pp. 10636–10641. ISSN: 10916490. DOI: 10.1073/PNAS.1721640115.
- [37] Peter Christensen, Ignacio Sarmiento-Barbieri, and Christopher Timmins. *Housing Discrimination and the Pollution Exposure Gap in the United States*. Tech. rep. National Bureau of Economic Research, 2020. DOI: 10.3386/w26805. URL: <https://www.nber.org/papers/w26805>.
- [38] *Dakota Access pipeline | US news | The Guardian*. URL: <https://www.theguardian.com/us-news/dakota-access-pipeline>.
- [39] *Dakota Access Pipeline: What to Know About the Controversy | Time*. URL: <https://time.com/4548566/dakota-access-pipeline-standing-rock-sioux/>.
- [40] *The Keystone XL Pipeline: Everything You Need To Know | NRDC*. URL: <https://www.nrdc.org/stories/what-keystone-pipeline>.
- [41] Paul A M Van Lange, Jeff Joireman, and Manfred Milinski. "Climate Change: What Psychology Can Offer in Terms of Insights and Solutions." In: *Current directions in psychological science* 27.4 (Aug. 2018), pp. 269–274. ISSN: 0963-7214. DOI: 10.1177/0963721417753945. URL: <http://www.ncbi.nlm.nih.gov/pubmed/30166778>.
- [42] *Humans Wired to Respond to Short-Term Problems : NPR*. URL: <https://www.npr.org/templates/story/story.php?storyId=5530483&t=1646779097962>.
- [43] Kristen Ardani et al. *Solar Futures Study*. Tech. rep. United States Department of Energy, 2021. URL: <https://www.energy.gov/sites/default/files/2021-09/Solar%20Futures%20Study.pdf>.
- [44] *Solar Manufacturing Cost Analysis | Solar Market Research and Analysis | NREL*. URL: <https://www.nrel.gov/solar/market-research-analysis/solar-manufacturing-cost.html>.
- [45] *Solar-cell manufacturing costs: innovation could level the field | MIT Energy Initiative*. URL: <https://energy.mit.edu/news/solar-cell-manufacturing-costs-innovation-could-level-the-field/>.
- [46] *Solar is now 'cheapest electricity in history', confirms IEA*. URL: <https://www.carbonbrief.org/solar-is-now-cheapest-electricity-in-history-confirms-iea>.
- [47] *Solar Roof | Tesla*. URL: <https://www.tesla.com/solarroof>.
- [48] *Silicon Solar Cell Parameters | PVEducation*. URL: <https://www.pveducation.org/pvcdrom/design-of-silicon-cells/silicon-solar-cell-parameters>.

- [49] Lucio Claudio Andreani et al. “Silicon solar cells: toward the efficiency limits”. In: <https://doi.org/10.1080/23746149.2018.1548305> 4.1 (Jan. 2018), p. 1548305. ISSN: 23746149. DOI: 10.1080/23746149.2018.1548305. URL: <https://www.tandfonline.com/doi/abs/10.1080/23746149.2018.1548305>.
- [50] Jing Zhang et al. “Critical review of recent progress of flexible perovskite solar cells”. In: *Materials Today* 39 (Oct. 2020), pp. 66–88. ISSN: 1369-7021. DOI: 10.1016/J.MATTOD.2020.05.002.
- [51] Benjia Dou et al. “Roll-to-Roll Printing of Perovskite Solar Cells”. In: *ACS Energy Letters* 3.10 (Oct. 2018), pp. 2558–2565. ISSN: 23808195. DOI: 10.1021/acsenergylett.8b01556. URL: <https://pubs.acs.org/doi/abs/10.1021/acsenergylett.8b01556>.
- [52] Lisa Anna Zafoschnig, Sebastian Nold, and Jan Christoph Goldschmidt. “The Race for Lowest Costs of Electricity Production: Techno-Economic Analysis of Silicon, Perovskite and Tandem Solar Cells”. In: *IEEE Journal of Photovoltaics* 10.6 (Nov. 2020), pp. 1632–1641. DOI: 10.1109/JPHOTOV.2020.3024739.
- [53] Molang Cai et al. “Cost-Performance Analysis of Perovskite Solar Modules”. In: *Advanced Science* 4.1 (Jan. 2017), p. 1600269. ISSN: 2198-3844. DOI: 10.1002/ADVS.201600269. URL: <https://onlinelibrary.wiley.com/doi/10.1002/advs.201600269>.
- [54] Zongqi Li et al. “Cost Analysis of Perovskite Tandem Photovoltaics”. In: *Joule* 2.8 (Aug. 2018), pp. 1559–1572. ISSN: 2542-4351. DOI: 10.1016/J.JOULE.2018.05.001.
- [55] Huseyin Sarialtin, Roland Geyer, and Ceylan Zafer. “Life cycle assessment of hole transport free planar–mesoscopic perovskite solar cells”. In: *Journal of Renewable and Sustainable Energy* 12.2 (Mar. 2020), p. 023502. ISSN: 19417012. DOI: 10.1063/1.5129784. URL: <https://aip.scitation.org/doi/abs/10.1063/1.5129784>.
- [56] Gustav Rose. “Beschreibung einiger neuen Mineralien des Urals”. In: *Annalen der Physik* 124.12 (Jan. 1839), pp. 551–573. ISSN: 1521-3889. DOI: 10.1002/ANDP.18391241205. URL: <https://onlinelibrary.wiley.com/doi/full/10.1002/andp.18391241205>.
- [57] Eugene A. Katz. *Perovskite: Name Puzzle and German-Russian Odyssey of Discovery*. 2020. DOI: 10.1002/hlca.202000061. URL: <https://onlinelibrary.wiley.com/doi/abs/10.1002/hlca.202000061>.
- [58] *Perovskite Solar Cells Market: Size, Share, Trend Report to 2022*. URL: <https://www.bccresearch.com/market-research/energy-and-resources/perovskite-solar-cells-materials-fabrication-and-global-markets-report.html>.
- [59] *A History of Perovskite Solar Cells*. URL: <https://blog.bccresearch.com/a-history-of-perovskite-solar-cells>.
- [60] *File:Perovskite ABO3.jpg - Wikimedia Commons*. URL: [https://commons.wikimedia.org/wiki/File:Perovskite\\_ABO3.jpg](https://commons.wikimedia.org/wiki/File:Perovskite_ABO3.jpg).

- [61] Akihiro Kojima et al. "Organometal halide perovskites as visible-light sensitizers for photovoltaic cells". In: *Journal of the American Chemical Society* 131.17 (May 2009), pp. 6050–6051. ISSN: 00027863. DOI: 10.1021/ja809598r. URL: <https://pubs.acs.org/doi/full/10.1021/ja809598r>.
- [62] Hui Seon Kim et al. "Lead Iodide Perovskite Sensitized All-Solid-State Submicron Thin Film Mesoscopic Solar Cell with Efficiency Exceeding 9%". In: *Scientific Reports* 2:1 2.1 (Aug. 2012), pp. 1–7. ISSN: 2045-2322. DOI: 10.1038/srep00591. URL: <https://www.nature.com/articles/srep00591>.
- [63] Nam Joong Jeon et al. "Solvent engineering for high-performance inorganic–organic hybrid perovskite solar cells". In: *Nature Materials* 2014 13:9 13.9 (July 2014), pp. 897–903. ISSN: 1476-4660. DOI: 10.1038/nmat4014. URL: <https://www.nature.com/articles/nmat4014>.
- [64] Julian Burschka et al. "Sequential deposition as a route to high-performance perovskite-sensitized solar cells". In: *Nature* 2013 499:7458 499.7458 (July 2013), pp. 316–319. ISSN: 1476-4687. DOI: 10.1038/nature12340. URL: <https://www.nature.com/articles/nature12340>.
- [65] Yana Vaynzof and Y Vaynzof. "The Future of Perovskite Photovoltaics—Thermal Evaporation or Solution Processing?" In: *Advanced Energy Materials* 10.48 (Dec. 2020), p. 2003073. ISSN: 1614-6840. DOI: 10.1002/AENM.202003073. URL: <https://onlinelibrary.wiley.com/doi/10.1002/aenm.202003073>.
- [66] Sabu Thomas and Aparna Thankappan. "Perovskite photovoltaics: Basic to advanced concepts and implementation". In: *Perovskite Photovoltaics: Basic to Advanced Concepts and Implementation* (Jan. 2018), pp. 1–501. DOI: 10.1016/C2016-0-03790-7.
- [67] Sandy Sánchez et al. "Flash Infrared Pulse Time Control of Perovskite Crystal Nucleation and Growth from Solution". In: *Crystal Growth and Design* 20.2 (Feb. 2020), pp. 670–679. ISSN: 15287505. DOI: 10.1021/acs.cgd.9b01083. URL: <https://pubs.acs.org/doi/abs/10.1021/acs.cgd.9b01083>.
- [68] Fernando Valadares et al. "Electronic structure panorama of halide perovskites: Approximated DFT-1/2 quasiparticle and relativistic corrections". In: *Journal of Physical Chemistry C* 124.34 (Aug. 2020), pp. 18390–18400. ISSN: 19327455. DOI: 10.1021/acs.jpcc.0c03672. URL: <https://pubs.acs.org/doi/full/10.1021/acs.jpcc.0c03672>.
- [69] Christopher Eames. *CH<sub>3</sub>NH<sub>3</sub>PbI<sub>3</sub> Structure*. URL: <http://www.nature.com/ncomms/2015/150624/ncomms8497/full/ncomms8497.html>.
- [70] *PbI<sub>2</sub> Structure*. URL: <https://upload.wikimedia.org/wikipedia/commons/6/67/Lead-diiodide-3D-polyhedra.png>.
- [71] Zhen Li et al. "Stabilizing Perovskite Structures by Tuning Tolerance Factor: Formation of Formamidinium and Cesium Lead Iodide Solid-State Alloys". In: *Chemistry of Materials* 28.1 (Jan. 2016), pp. 284–292. ISSN: 15205002. DOI: 10.1021/acs.chemmater.5b04107. URL: <https://pubs.acs.org/doi/full/10.1021/acs.chemmater.5b04107>.

- [72] Anna Amat et al. "Cation-induced band-gap tuning in organohalide perovskites: Interplay of spin-orbit coupling and octahedra tilting". In: *Nano Letters* 14.6 (June 2014), pp. 3608–3616. ISSN: 15306992. DOI: 10.1021/nl5012992. URL: <https://pubs.acs.org/doi/full/10.1021/nl5012992>.
- [73] Alexander D. Jodlowski et al. "Large guanidinium cation mixed with methylammonium in lead iodide perovskites for 19% efficient solar cells". In: *Nature Energy* 2017 2:12 2.12 (Dec. 2017), pp. 972–979. ISSN: 2058-7546. DOI: 10.1038/s41560-017-0054-3. URL: <https://www.nature.com/articles/s41560-017-0054-3>.
- [74] Monojit Bag, Ramesh Kumar, and Priya Srivastava. "Role of a-site cation and x-site halide interactions in mixed-cation mixed-halide perovskites for determining anomalously high ideality factor and the super-linear power law in ac ionic conductivity at operating temperature". In: *ACS Applied Electronic Materials* 2.12 (Dec. 2020), pp. 4087–4098. ISSN: 26376113. DOI: 10.1021/acsaelm.0c00874. URL: <https://pubs.acs.org/doi/full/10.1021/acsaelm.0c00874>.
- [75] Pina Pitriana et al. "The characteristics of band structures and crystal binding in all-inorganic perovskite APbBr<sub>3</sub> studied by the first principle calculations using the Density Functional Theory (DFT) method". In: *Results in Physics* 15 (Dec. 2019), p. 102592. ISSN: 2211-3797. DOI: 10.1016/J.RINP.2019.102592.
- [76] Muhammad Usman and Qingfeng Yan. "Recent Advancements in Crystalline Pb-Free Halide Double Perovskites". In: *Crystals* 2020, Vol. 10, Page 62 10.2 (Jan. 2020), p. 62. ISSN: 2073-4352. DOI: 10.3390/CRYST10020062. URL: <https://www.mdpi.com/2073-4352/10/2/62>.
- [77] Qingdong Ou et al. "Band structure engineering in metal halide perovskite nanostructures for optoelectronic applications". In: *Nano Materials Science* 1.4 (Dec. 2019), pp. 268–287. ISSN: 2589-9651. DOI: 10.1016/J.NANOMS.2019.10.004.
- [78] Harshadeep Kukkikatte Ramamurthy Rao et al. "Techno-economic assessment of titanium dioxide nanorod-based perovskite solar cells: From lab-scale to large-scale manufacturing". In: *Applied Energy* 298 (Sept. 2021), p. 117251. ISSN: 0306-2619. DOI: 10.1016/J.APENERGY.2021.117251.
- [79] Tomáš Homola et al. "Perovskite Solar Cells with Low-Cost TiO<sub>2</sub> Mesoporous Photoanodes Prepared by Rapid Low-Temperature (70 °C) Plasma Processing". In: *ACS Applied Energy Materials* 3.12 (Dec. 2020), pp. 12009–12018. ISSN: 25740962. DOI: 10.1021/acsaem.0c02144. URL: <https://pubs.acs.org/doi/full/10.1021/acsaem.0c02144>.
- [80] Khalid Mahmood, Saad Sarwar, and Muhammad Taqi Mehran. "Current status of electron transport layers in perovskite solar cells: materials and properties". In: *RSC Advances* 7.28 (Mar. 2017), pp. 17044–17062. ISSN: 2046-2069. DOI: 10.1039/C7RA00002B. URL: <https://pubs.rsc.org/en/content/articlelanding/2017/ra/c7ra00002b>.

- [81] Chunyu Liu et al. "Effective stability enhancement in ZnO-based perovskite solar cells by MAI modification". In: *Journal of Materials Chemistry A* 9.20 (May 2021), pp. 12161–12168. ISSN: 2050-7496. DOI: 10.1039/D1TA02697F. URL: <https://pubs.rsc.org/en/content/articlelanding/2021/ta/d1ta02697f>.
- [82] Gon Namkoong, Abdullah A. Mamun, and Tanzila Tasnim Ava. "Impact of PCBM/C60 electron transfer layer on charge transports on ordered and disordered perovskite phases and hysteresis-free perovskite solar cells". In: *Organic Electronics* 56 (May 2018), pp. 163–169. ISSN: 1566-1199. DOI: 10.1016/J.ORGEL.2018.02.010.
- [83] Ilario Gelmetti et al. "Energy alignment and recombination in perovskite solar cells: weighted influence on the open circuit voltage". In: *Energy & Environmental Science* 12.4 (Apr. 2019), pp. 1309–1316. ISSN: 1754-5706. DOI: 10.1039/C9EE00528E. URL: <https://pubs.rsc.org/en/content/articlelanding/2019/ee/c9ee00528e>.
- [84] Florine M. Rombach, Saif A. Haque, and Thomas J. Macdonald. "Lessons learned from spiro-OMeTAD and PTAA in perovskite solar cells". In: *Energy & Environmental Science* 14.10 (Oct. 2021), pp. 5161–5190. ISSN: 1754-5706. DOI: 10.1039/D1EE02095A. URL: <https://pubs.rsc.org/en/content/articlelanding/2021/ee/d1ee02095a>.
- [85] Zhen Li et al. "Extrinsic ion migration in perovskite solar cells". In: *Energy & Environmental Science* 10.5 (May 2017), pp. 1234–1242. ISSN: 1754-5706. DOI: 10.1039/C7EE00358G. URL: <https://pubs.rsc.org/en/content/articlelanding/2017/ee/c7ee00358g>.
- [86] Seongtak Kim et al. "Relationship between ion migration and interfacial degradation of CH<sub>3</sub>NH<sub>3</sub>PbI<sub>3</sub> perovskite solar cells under thermal conditions". In: *Scientific Reports* 7.1 (Dec. 2017). ISSN: 20452322. DOI: 10.1038/S41598-017-00866-6. URL: <https://www.ncbi.nlm.nih.gov/pmc/articles/PMC5430925/>.
- [87] Eui Hyuk Jung et al. "Efficient, stable and scalable perovskite solar cells using poly(3-hexylthiophene)". In: *Nature* 2019 567:7749 567.7749 (Mar. 2019), pp. 511–515. ISSN: 1476-4687. DOI: 10.1038/s41586-019-1036-3. URL: <https://www.nature.com/articles/s41586-019-1036-3>.
- [88] Eric Wei Guang Diao, Efat Jokar, and Mohammad Rameez. "Strategies to improve performance and stability for tin-based perovskite solar cells". In: *ACS Energy Letters* 4 (May 2019), pp. 1930–1937. ISSN: 23808195. DOI: 10.1021/acsenenergylett.9b01179. URL: <https://pubs.acs.org/doi/full/10.1021/acsenenergylett.9b01179>.
- [89] Wenbin Han et al. "Recent Progress of Inverted Perovskite Solar Cells with a Modified PEDOT:PSS Hole Transport Layer". In: *ACS Applied Materials and Interfaces* 12.44 (Nov. 2020), pp. 49297–49322. ISSN: 19448252. DOI: 10.1021/acsami.0c13576. URL: <https://pubs.acs.org/doi/abs/10.1021/acsami.0c13576>.
- [90] Yawen Huang et al. "Stable Layered 2D Perovskite Solar Cells with an Efficiency of over 19% via Multifunctional Interfacial Engineering". In: *Journal of the American Chemical Society* 143.10 (Mar. 2021), pp. 3911–3917. ISSN: 15205126. DOI: 10.1021/jacs.0c13087. URL: <https://pubs.acs.org/doi/abs/10.1021/jacs.0c13087>.



- [91] Xiaoming Zhao et al. "Advancing 2D Perovskites for Efficient and Stable Solar Cells: Challenges and Opportunities". In: *Advanced Materials* 34.3 (Jan. 2022), p. 2105849. ISSN: 1521-4095. DOI: 10.1002/ADMA.202105849. URL: <https://onlinelibrary.wiley.com/doi/10.1002/adma.202105849>.
- [92] Yi Yang et al. "Origin of the stability of two-dimensional perovskites: a first-principles study". In: *Journal of Materials Chemistry A* 6.30 (July 2018), pp. 14949–14955. ISSN: 2050-7496. DOI: 10.1039/C8TA01496E. URL: <https://pubs.rsc.org/en/content/articlelanding/2018/ta/c8ta01496e>.
- [93] Eun Bi Kim et al. "A review on two-dimensional (2D) and 2D-3D multidimensional perovskite solar cells: Perovskites structures, stability, and photovoltaic performances". In: *Journal of Photochemistry and Photobiology C: Photochemistry Reviews* 48 (Sept. 2021), p. 100405. ISSN: 1389-5567. DOI: 10.1016/J.JPHOTOCHEMREV.2021.100405.
- [94] A. De Vos. "Detailed balance limit of the efficiency of tandem solar cells". In: *Journal of Physics D: Applied Physics* 13.5 (May 1980), p. 839. ISSN: 0022-3727. DOI: 10.1088/0022-3727/13/5/018. URL: <https://iopscience.iop.org/article/10.1088/0022-3727/13/5/018>.
- [95] C. H. Henry. "Limiting efficiencies of ideal single and multiple energy gap terrestrial solar cells". In: *Journal of Applied Physics* 51.8 (July 2008), p. 4494. ISSN: 0021-8979. DOI: 10.1063/1.328272. URL: <https://aip.scitation.org/doi/abs/10.1063/1.328272>.
- [96] J. E. Parrott. "The limiting efficiency of an edge-illuminated multigap solar cell". In: *Journal of Physics D: Applied Physics* 12.3 (Mar. 1979), p. 441. ISSN: 0022-3727. DOI: 10.1088/0022-3727/12/3/014. URL: <https://iopscience.iop.org/article/10.1088/0022-3727/12/3/014>.
- [97] Yichuan Chen et al. "Large-area perovskite solar cells – a review of recent progress and issues". In: *RSC Advances* 8.19 (Mar. 2018), pp. 10489–10508. ISSN: 2046-2069. DOI: 10.1039/C8RA00384J. URL: <https://pubs.rsc.org/en/content/articlelanding/2018/ra/c8ra00384j>.
- [98] S. Akhil et al. "Review on perovskite silicon tandem solar cells: Status and prospects 2T, 3T and 4T for real world conditions". In: *Materials & Design* 211 (Dec. 2021), p. 110138. ISSN: 0264-1275. DOI: 10.1016/J.MATDES.2021.110138.
- [99] Hui Li and Wei Zhang. "Perovskite Tandem Solar Cells: From Fundamentals to Commercial Deployment". In: *Chemical Reviews* 120.18 (Sept. 2020), pp. 9835–9950. ISSN: 15206890. DOI: 10.1021/acs.chemrev.9b00780. URL: <https://pubs.acs.org/doi/full/10.1021/acs.chemrev.9b00780>.
- [100] *Oxford PV secures £65 million in Series D funding round | Oxford PV*. URL: <https://www.oxfordpv.com/news/oxford-pv-secures-ps65-million-series-d-funding-round>.
- [101] Jiachen Sun et al. "Organic/Inorganic Metal Halide Perovskite Optoelectronic Devices beyond Solar Cells". In: *Advanced Science* 5.5 (May 2018), p. 1700780. ISSN: 2198-3844. DOI: 10.1002/ADVS.201700780. URL: <https://onlinelibrary.wiley.com/doi/10.1002/advs.201700780>.

- [102] Yuanwei Wang et al. “Perovskite quantum dots encapsulated in electrospun fiber membranes as multifunctional supersensitive sensors for biomolecules, metal ions and pH”. In: *Nanoscale Horizons* 2.4 (June 2017), pp. 225–232. ISSN: 2055-6764. DOI: 10.1039/C7NH00057J. URL: <https://pubs.rsc.org/en/content/articlelanding/2017/nh/c7nh00057j>.
- [103] Ronald E. Cohen. “Origin of ferroelectricity in perovskite oxides”. In: *Nature* 1992 358:6382 358.6382 (1992), pp. 136–138. ISSN: 1476-4687. DOI: 10.1038/358136a0. URL: <https://www.nature.com/articles/358136a0>.
- [104] Hyojin Park, Chihyeon Ha, and Ju Hyuck Lee. “Advances in piezoelectric halide perovskites for energy harvesting applications”. In: *Journal of Materials Chemistry A* 8.46 (Dec. 2020), pp. 24353–24367. ISSN: 2050-7496. DOI: 10.1039/D0TA08780G. URL: <https://pubs.rsc.org/en/content/articlelanding/2020/ta/d0ta08780g>.
- [105] Konrad Domanski et al. “Migration of cations induces reversible performance losses over day/night cycling in perovskite solar cells”. In: *Energy & Environmental Science* 10.2 (Feb. 2017), pp. 604–613. ISSN: 1754-5706. DOI: 10.1039/C6EE03352K. URL: <https://pubs.rsc.org/en/content/articlelanding/2017/ee/c6ee03352k>.
- [106] Shuxia Tao et al. “Absolute energy level positions in tin- and lead-based halide perovskites”. In: *Nature Communications* 2019 10:1 10.1 (June 2019), pp. 1–10. ISSN: 2041-1723. DOI: 10.1038/s41467-019-10468-7. URL: <https://www.nature.com/articles/s41467-019-10468-7>.
- [107] Jacky Even et al. “DFT and  $k \cdot p$  modelling of the phase transitions of lead and tin halide perovskites for photovoltaic cells”. In: *physica status solidi (RRL) – Rapid Research Letters* 8.1 (Jan. 2014), pp. 31–35. ISSN: 1862-6270. DOI: 10.1002/PSSR.201308183. URL: <https://onlinelibrary.wiley.com/doi/10.1002/pssr.201308183>.
- [108] marcus-cmc. *Shockley-Queisser-limit: Calculation and visualization tools for theoretical solar cell efficiencies based on the Shockley Queisser limit with options to change temperature, light intensity, and radiative efficiency*. URL: <https://github.com/marcus-cmc/Shockley-Queisser-limit>.
- [109] Damiano Ricciarelli et al. “Instability of tin iodide perovskites: Bulk p-doping versus surface tin oxidation”. In: *ACS Energy Letters* 5.9 (Sept. 2020), pp. 2787–2795. ISSN: 23808195. DOI: 10.1021/acsenergylett.0c01174. URL: <https://pubs.acs.org/doi/full/10.1021/acsenergylett.0c01174>.
- [110] Yang Zhou et al. “Defect activity in metal halide perovskites with wide and narrow bandgap”. In: *Nature Reviews Materials* 2021 (June 2021), pp. 1–17. ISSN: 2058-8437. DOI: 10.1038/s41578-021-00331-x. URL: <https://www.nature.com/articles/s41578-021-00331-x>.
- [111] Zhibin Yang et al. “Enhancing electron diffusion length in narrow-bandgap perovskites for efficient monolithic perovskite tandem solar cells”. In: *Nature Communications* 2019 10:1 10.1 (Oct. 2019), pp. 1–9. ISSN: 2041-1723. DOI: 10.1038/s41467-019-12513-x. URL: <https://www.nature.com/articles/s41467-019-12513-x>.

- [112] Maria Konstantakou and Thomas Stergiopoulos. "A critical review on tin halide perovskite solar cells". In: *Journal of Materials Chemistry A* 5.23 (June 2017), pp. 11518–11549. ISSN: 2050-7496. DOI: 10.1039/C7TA00929A. URL: <https://pubs.rsc.org/en/content/articlelanding/2017/ta/c7ta00929a>.
- [113] Taishi Noma et al. "Analysis of hysteresis behavior of tin perovskite solar cells using electric-field-induced optical second-harmonic generation measurement". In: *2019 Electron Devices Technology and Manufacturing Conference, EDTM 2019* (Mar. 2019), pp. 231–233. DOI: 10.1109/EDTM.2019.8731043.
- [114] Hansheng Li, Qi Wei, and Zhijun Ning. "Toward high efficiency tin perovskite solar cells: A perspective". In: *Applied Physics Letters* 117.6 (Aug. 2020), p. 060502. ISSN: 0003-6951. DOI: 10.1063/5.0014804. URL: <https://aip.scitation.org/doi/abs/10.1063/5.0014804>.
- [115] Asim Aftab and Md Imteyaz Ahmad. "A review of stability and progress in tin halide perovskite solar cell". In: *Solar Energy* 216 (Mar. 2021), pp. 26–47. ISSN: 0038-092X. DOI: 10.1016/J.SOLENER.2020.12.065.
- [116] Mahmoud Aldamasy et al. "Challenges in tin perovskite solar cells". In: *Physical Chemistry Chemical Physics* 23.41 (Oct. 2021), pp. 23413–23427. ISSN: 14639076. DOI: 10.1039/D1CP02596A. URL: <https://pubs.rsc.org/en/content/articlelanding/2021/cp/d1cp02596a>.
- [117] Syed Zulqarnain Haider et al. "A theoretical study for high-performance inverted p-i-n architecture perovskite solar cells with cuprous iodide as hole transport material". In: *Current Applied Physics* 20.9 (2020), pp. 1080–1089. DOI: 10.1016/j.cap.2020.06.022. URL: <https://doi.org/10.1016/j.cap.2020.06.022>.
- [118] Xianyuan Jiang et al. "One-Step Synthesis of SnI<sub>2</sub>·(DMSO)<sub>x</sub>Adducts for High-Performance Tin Perovskite Solar Cells". In: *Journal of the American Chemical Society* 143.29 (July 2021), pp. 10970–10976. ISSN: 15205126. DOI: 10.1021/jacs.1c03032. URL: <https://pubs.acs.org/doi/full/10.1021/jacs.1c03032>.
- [119] Pietro Caprioglio et al. "On the Relation between the Open-Circuit Voltage and Quasi-Fermi Level Splitting in Efficient Perovskite Solar Cells". In: *Advanced Energy Materials* 9.33 (Sept. 2019), p. 1901631. ISSN: 1614-6840. DOI: 10.1002/AENM.201901631. URL: <https://onlinelibrary.wiley.com/doi/10.1002/aenm.201901631>.
- [120] Xin Zhang et al. "The Voltage Loss in Tin Halide Perovskite Solar Cells: Origins and Perspectives". In: *Advanced Functional Materials* (2021), p. 2108832. ISSN: 1616-3028. DOI: 10.1002/ADFM.202108832. URL: <https://onlinelibrary.wiley.com/doi/10.1002/adfm.202108832>.
- [121] Alex Niemegeers et al. *SCAPS-1D*. URL: <https://scaps.elis.ugent.be/>.
- [122] S. Abdelaziz et al. "Investigating the performance of formamidinium tin-based perovskite solar cell by SCAPS device simulation". In: *Optical Materials* 101 (Mar. 2020), p. 109738. ISSN: 09253467. DOI: 10.1016/j.optmat.2020.109738.

- [123] Ke Yang et al. "Determination of Electron and Hole Mobility of Regioregular Poly(3-hexylthiophene) by the Time of Flight Method) Determination of Electron and Hole Mobility of Regioregular Poly(3-hexylthiophene) by the Time of Flight Method Determination of Electron and ". In: *Journal of Macromolecular Science, Part A* 44 (2007), pp. 1261–1264. ISSN: 1520-5738. DOI: 10.1080/10601320701606711. URL: <https://www.tandfonline.com/action/journalInformation?journalCode=lmsa20>.
- [124] Mohammad Mahdi Tavakoli et al. "Mesoscopic Oxide Double Layer as Electron Specific Contact for Highly Efficient and UV Stable Perovskite Photovoltaics". In: 18 (2018), p. 26. DOI: 10.1021/acs.nanolett.7b05469. URL: <https://pubs.acs.org/sharingguidelines>.
- [125] Si Chen. *Dielectric constant measurement of P3HT, polystyrene, and polyethylene*. Tech. rep. URL: [https://fse.studenttheses.ub.rug.nl/15828/1/Report\\_dielectric\\_constant\\_mea\\_1.pdf](https://fse.studenttheses.ub.rug.nl/15828/1/Report_dielectric_constant_mea_1.pdf).
- [126] Xin He et al. "Highly efficient tin perovskite solar cells achieved in a wide oxygen concentration range". In: *Journal of Materials Chemistry A* 8.5 (Feb. 2020), pp. 2760–2768. ISSN: 2050-7496. DOI: 10.1039/C9TA13159K. URL: <https://pubs.rsc.org/en/content/articlelanding/2020/ta/c9ta13159k>.
- [127] Wolfgang Tress and Olle Inganäs. "Simple experimental test to distinguish extraction and injection barriers at the electrodes of (organic) solar cells with S-shaped current–voltage characteristics". In: *Solar Energy Materials and Solar Cells* 117 (Oct. 2013), pp. 599–603. ISSN: 0927-0248. DOI: 10.1016/J.SOLMAT.2013.07.014.
- [128] Rebecca Saive. "S-Shaped Current-Voltage Characteristics in Solar Cells: A Review". In: *IEEE Journal of Photovoltaics* 9.6 (Nov. 2019), pp. 1477–1484. ISSN: 21563403. DOI: 10.1109/JPHOTOV.2019.2930409.
- [129] M. Thambidurai et al. "Highly stable and efficient planar perovskite solar cells using ternary metal oxide electron transport layers". In: *Journal of Power Sources* 448 (Feb. 2020), p. 227362. ISSN: 0378-7753. DOI: 10.1016/J.JPOWSOUR.2019.227362.
- [130] Ahmed E. Shalan et al. "Tin–zinc-oxide nanocomposites (SZO) as promising electron transport layers for efficient and stable perovskite solar cells". In: *Nanoscale Advances* 1.7 (July 2019), pp. 2654–2662. ISSN: 2516-0230. DOI: 10.1039/C9NA00182D. URL: <https://pubs.rsc.org/en/content/articlelanding/2019/na/c9na00182d>.
- [131] Weijun Ke et al. "TiO<sub>2</sub>-ZnS Cascade Electron Transport Layer for Efficient Formamidinium Tin Iodide Perovskite Solar Cells". In: *Journal of the American Chemical Society* 138.45 (Nov. 2016), pp. 14998–15003. ISSN: 15205126. DOI: 10.1021/jacs.6b08790. URL: <https://pubs.acs.org/doi/full/10.1021/jacs.6b08790>.
- [132] Tomoyasu Yokoyama et al. "Improving the Open-Circuit Voltage of Sn-Based Perovskite Solar Cells by Band Alignment at the Electron Transport Layer/Perovskite Layer Interface". In: *ACS Applied Materials and Interfaces* 12.24 (June 2020), pp. 27131–27139. ISSN: 19448252. DOI: 10.1021/acsami.0c04676. URL: <https://pubs.acs.org/doi/full/10.1021/acsami.0c04676>.

- [133] Xuedong Ou et al. "Long-range magnetic interaction and frustration in double perovskites  $\text{Sr}_2\text{NiIrO}_6$  and  $\text{Sr}_2\text{ZnIrO}_6$ ". In: *Scientific Reports* 2014 4:1 4.1 (Dec. 2014), pp. 1–6. ISSN: 2045-2322. DOI: 10.1038/srep07542. URL: <https://www.nature.com/articles/srep07542>.
- [134] Neelima Singh, Alpana Agarwal, and Mohit Agarwal. "Performance evaluation of lead-free double-perovskite solar cell". In: *Optical Materials* 114 (Apr. 2021), p. 110964. ISSN: 0925-3467. DOI: 10.1016/J.OPTMAT.2021.110964.
- [135] Jingxiu Yang, Peng Zhang, and Su Huai Wei. "Band Structure Engineering of  $\text{Cs}_2\text{AgBiBr}_6$  Perovskite through Order-Disordered Transition: A First-Principle Study". In: *Journal of Physical Chemistry Letters* 9.1 (Jan. 2018), pp. 31–35. ISSN: 19487185. DOI: 10.1021/acs.jpcclett.7b02992. URL: <https://pubs.acs.org/doi/full/10.1021/acs.jpcclett.7b02992>.
- [136] Xiaoqing Yang et al. "Simultaneous Power Conversion Efficiency and Stability Enhancement of  $\text{Cs}_2\text{AgBiBr}_6$  Lead-Free Inorganic Perovskite Solar Cell through Adopting a Multifunctional Dye Interlayer". In: *Advanced Functional Materials* 30.23 (June 2020), p. 2001557. ISSN: 1616-3028. DOI: 10.1002/ADFM.202001557. URL: <https://onlinelibrary.wiley.com/doi/10.1002/adfm.202001557>.
- [137] Liping Yu and Alex Zunger. "Identification of potential photovoltaic absorbers based on first-principles spectroscopic screening of materials". In: *Physical Review Letters* 108.6 (Feb. 2012), p. 068701. ISSN: 00319007. DOI: 10.1103/PhysRevLett.108.068701. URL: <https://journals.aps.org/prl/abstract/10.1103/PhysRevLett.108.068701>.
- [138] Yalan She et al. "Identifying and Passivating Killer Defects in Pb-Free Double  $\text{Cs}_2\text{AgBiBr}_6$  Perovskite". In: *Journal of Physical Chemistry Letters* 12.43 (Nov. 2021), pp. 10581–10588. ISSN: 19487185. DOI: 10.1021/acs.jpcclett.1c03134. URL: <https://pubs.acs.org/doi/full/10.1021/acs.jpcclett.1c03134>.
- [139] Davide Bartesaghi et al. "Charge Carrier Dynamics in  $\text{Cs}_2\text{AgBiBr}_6$  Double Perovskite". In: *Journal of Physical Chemistry C* 122.9 (Mar. 2018), pp. 4809–4816. ISSN: 19327455. DOI: 10.1021/acs.jpcc.8b00572. URL: <https://pubs.acs.org/doi/full/10.1021/acs.jpcc.8b00572>.
- [140] Joshua Leveillee, George Volonakis, and Feliciano Giustino. "Phonon-Limited Mobility and Electron-Phonon Coupling in Lead-Free Halide Double Perovskites". In: *Journal of Physical Chemistry Letters* 12.18 (May 2021), pp. 4474–4482. ISSN: 19487185. DOI: 10.1021/acs.jpcclett.1c00841. URL: <https://pubs.acs.org/doi/abs/10.1021/acs.jpcclett.1c00841>.
- [141] Thomas Kirchartz et al. "Photoluminescence-Based Characterization of Halide Perovskites for Photovoltaics". In: *Advanced Energy Materials* 10.26 (July 2020), p. 1904134. ISSN: 1614-6840. DOI: 10.1002/AENM.201904134. URL: <https://onlinelibrary.wiley.com/doi/10.1002/aenm.201904134>.

- [142] John C. De Mello, H. Felix Wittmann, and Richard H. Friend. “An improved experimental determination of external photoluminescence quantum efficiency”. In: *Advanced Materials* 9.3 (Mar. 1997), pp. 230–232. ISSN: 1521-4095. DOI: 10.1002/ADMA.19970090308. URL: <https://onlinelibrary.wiley.com/doi/10.1002/adma.19970090308>.
- [143] Enrico Greul et al. “Highly stable, phase pure Cs<sub>2</sub>AgBiBr<sub>6</sub> double perovskite thin films for optoelectronic applications”. In: *Journal of Materials Chemistry A* 5.37 (Sept. 2017), pp. 19972–19981. ISSN: 2050-7496. DOI: 10.1039/C7TA06816F. URL: <https://pubs.rsc.org/en/content/articlehtml/2017/ta/c7ta06816f>.
- [144] Shuting Yin et al. “Self-powered ultraviolet-blue photodetector based on GaN/double halide perovskite/NiO heterostructure”. In: *Journal of Materials Science* 56.24 (Aug. 2021), pp. 13633–13645. ISSN: 15734803. DOI: 10.1007/S10853-021-06169-6. URL: <https://link.springer.com/article/10.1007/s10853-021-06169-6>.
- [145] Tao Luo et al. “Dual interfacial engineering for efficient Cs<sub>2</sub>AgBiBr<sub>6</sub> based solar cells”. In: *Journal of Energy Chemistry* 53 (Feb. 2021), pp. 372–378. ISSN: 2095-4956. DOI: 10.1016/J.JEACHEM.2020.05.016.
- [146] S. J. Zelewski et al. “Revealing the nature of photoluminescence emission in the metal-halide double perovskite Cs<sub>2</sub>AgBiBr<sub>6</sub>”. In: *Journal of Materials Chemistry C* 7.27 (July 2019), pp. 8350–8356. ISSN: 2050-7534. DOI: 10.1039/C9TC02402F. URL: <https://pubs.rsc.org/en/content/articlelanding/2019/tc/c9tc02402f>.
- [147] Laura Schade et al. “Structural and Optical Properties of Cs<sub>2</sub>AgBiBr<sub>6</sub> Double Perovskite”. In: *ACS Energy Letters* 4.1 (Jan. 2019), pp. 299–305. ISSN: 23808195. DOI: 10.1021/ACSENERGYLETT.8B02090/SUPPL{ }FILE/NZ8B02090{ }SI{ }001.PDF. URL: <https://pubs.acs.org/doi/abs/10.1021/acsenergylett.8b02090>.
- [148] Wanyi Nie et al. “Light-activated photocurrent degradation and self-healing in perovskite solar cells”. In: *Nature Communications* 2016 7:1 7.1 (May 2016), pp. 1–9. ISSN: 2041-1723. DOI: 10.1038/ncomms11574. URL: <https://www.nature.com/articles/ncomms11574>.
- [149] Eric T. Hoke et al. “Reversible photo-induced trap formation in mixed-halide hybrid perovskites for photovoltaics”. In: *Chemical Science* 6.1 (Dec. 2014), pp. 613–617. ISSN: 2041-6539. DOI: 10.1039/C4SC03141E. URL: <https://pubs.rsc.org/en/content/articlelanding/2015/sc/c4sc03141e>.
- [150] Pranav H Joshi, Liang Zhang, and Istiaque M Hossain. “The physics of photon induced degradation of perovskite solar cells”. In: *AIP Advances* 6 (2016), p. 115114. DOI: 10.1063/1.4967817. URL: <http://dx.doi.org/10.1063/1.4967817>.
- [151] Hamid Shahivandi, Majid Vaezzadeh, and Mohammadreza Saeidi. “Theory of light-induced degradation in perovskite solar cells”. In: *Solar Energy Materials and Solar Cells* 208 (May 2020), p. 110383. ISSN: 0927-0248. DOI: 10.1016/J.SOLMAT.2019.110383.
- [152] Mingkui Wang et al. “Temperature Dependent Characteristics of Perovskite Solar Cells”. In: *ChemistrySelect* 2.16 (May 2017), pp. 4469–4477. ISSN: 2365-6549. DOI: 10.1002/SLCT.201700776. URL: <https://onlinelibrary.wiley.com/doi/full/10.1002/slct.201700776>.

- [153] Hua Zhang et al. "Effect of temperature on the efficiency of organometallic perovskite solar cells". In: *Journal of Energy Chemistry* 24.6 (Nov. 2015), pp. 729–735. ISSN: 2095-4956. DOI: 10.1016/J.JEChem.2015.10.007.
- [154] Tian Du et al. "Light-intensity and thickness dependent efficiency of planar perovskite solar cells: charge recombination versus extraction". In: *Journal of Materials Chemistry C* 8.36 (Sept. 2020), pp. 12648–12655. ISSN: 2050-7534. DOI: 10.1039/D0TC03390A. URL: <https://pubs.rsc.org/en/content/articlehtml/2020/tc/d0tc03390a>  
<https://pubs.rsc.org/en/content/articlelanding/2020/tc/d0tc03390a>.
- [155] Leqi Lin and N. M. Ravindra. "Temperature dependence of CIGS and perovskite solar cell performance: an overview". In: *SN Applied Sciences* 2.8 (Aug. 2020), pp. 1–12. ISSN: 25233971. DOI: 10.1007/S42452-020-3169-2. URL: <https://link.springer.com/article/10.1007/s42452-020-3169-2>.
- [156] Bo Chen et al. "Synergistic Effect of Elevated Device Temperature and Excess Charge Carriers on the Rapid Light-Induced Degradation of Perovskite Solar Cells". In: *Advanced Materials* 31.35 (Aug. 2019), p. 1902413. ISSN: 1521-4095. DOI: 10.1002/ADMA.201902413. URL: <https://onlinelibrary.wiley.com/doi/10.1002/adma.201902413>.
- [157] Konrad Domanski et al. "Systematic investigation of the impact of operation conditions on the degradation behaviour of perovskite solar cells". In: *Nature Energy* 2017 3:1 3.1 (Jan. 2018), pp. 61–67. ISSN: 2058-7546. DOI: 10.1038/s41560-017-0060-5. URL: <https://www.nature.com/articles/s41560-017-0060-5>.
- [158] Suhas Mahesh et al. "Revealing the origin of voltage loss in mixed-halide perovskite solar cells". In: *Energy & Environmental Science* 13.1 (Jan. 2020), pp. 258–267. ISSN: 1754-5706. DOI: 10.1039/C9EE02162K. URL: <https://pubs.rsc.org/en/content/articlelanding/2020/ee/c9ee02162k>.
- [159] Uli Würfel et al. "Impact of charge transport on current–voltage characteristics and power-conversion efficiency of organic solar cells". In: *Nature Communications* 2015 6:1 6.1 (Apr. 2015), pp. 1–9. ISSN: 2041-1723. DOI: 10.1038/ncomms7951. URL: <https://www.nature.com/articles/ncomms7951>.
- [160] Jarla Thiesbrummel et al. "Universal Current Losses in Perovskite Solar Cells Due to Mobile Ions". In: *Advanced Energy Materials* 11.34 (Sept. 2021), p. 2101447. ISSN: 1614-6840. DOI: 10.1002/AENM.202101447. URL: <https://onlinelibrary.wiley.com/doi/10.1002/aenm.202101447>.
- [161] Nandi Wu et al. "Identifying the Cause of Voltage and Fill Factor Losses in Perovskite Solar Cells by Using Luminescence Measurements". In: *Energy Technology* 5.10 (Oct. 2017), pp. 1827–1835. ISSN: 2194-4296. DOI: 10.1002/ENTE.201700374. URL: <https://onlinelibrary.wiley.com/doi/10.1002/ente.201700374>.
- [162] Pietro Caprioglio et al. "On the Origin of the Ideality Factor in Perovskite Solar Cells". In: *Advanced Energy Materials* 10.27 (July 2020), p. 2000502. ISSN: 1614-6840. DOI: 10.1002/AENM.202000502. URL: <https://onlinelibrary.wiley.com/doi/10.1002/aenm.202000502>.

- [163] Minkjin Kim et al. “Conformal quantum dot–SnO<sub>2</sub> layers as electron transporters for efficient perovskite solar cells”. In: *Science* 375.6578 (2020), pp. 302–306. DOI: 10.1126/science.abh1885. URL: <https://www.science.org/doi/10.1126/science.abh1885>.
- [164] Wolfgang Tress et al. “Interpretation and evolution of open-circuit voltage, recombination, ideality factor and subgap defect states during reversible light-soaking and irreversible degradation of perovskite solar cells”. In: *Energy & Environmental Science* 11.1 (Jan. 2018), pp. 151–165. ISSN: 1754-5706. DOI: 10.1039/C7EE02415K. URL: <https://pubs.rsc.org/en/content/articlelanding/2018/ee/c7ee02415k>.
- [165] Se Yong Jeong, Hui Seon Kim, and Nam Gyu Park. “Challenges for Thermally Stable Spiro-MeOTAD toward the Market Entry of Highly Efficient Perovskite Solar Cells”. In: *ACS Applied Materials and Interfaces* (2021). ISSN: 19448252. DOI: 10.1021/acsami.1c21852. URL: <https://pubs.acs.org/doi/full/10.1021/acsami.1c21852>.
- [166] Adam H. Slavney et al. “A Bismuth-Halide Double Perovskite with Long Carrier Recombination Lifetime for Photovoltaic Applications”. In: *Journal of the American Chemical Society* 138.7 (Mar. 2016), pp. 2138–2141. ISSN: 15205126. DOI: 10.1021/JACS.5B13294. URL: <https://pubs.acs.org/doi/full/10.1021/jacs.5b13294>.
- [167] Jin Kiong Ling et al. “A Perspective on the Commercial Viability of Perovskite Solar Cells”. In: *Solar RRL* 5.11 (Nov. 2021), p. 2100401. ISSN: 2367-198X. DOI: 10.1002/SOLR.202100401. URL: <https://onlinelibrary.wiley.com/doi/10.1002/solr.202100401>.
- [168] Rohit Abraham John et al. “Reconfigurable halide perovskite nanocrystal memristors for neuromorphic computing”. In: *Nature Communications* 2022 13:1 13.1 (Apr. 2022), pp. 1–10. ISSN: 2041-1723. DOI: 10.1038/s41467-022-29727-1. URL: <https://www.nature.com/articles/s41467-022-29727-1>.
- [169] Hanul Min et al. “Perovskite solar cells with atomically coherent interlayers on SnO<sub>2</sub> electrodes”. In: *Nature* 2021 598:7881 598.7881 (Oct. 2021), pp. 444–450. ISSN: 1476-4687. DOI: 10.1038/s41586-021-03964-8. URL: <https://www.nature.com/articles/s41586-021-03964-8>.
- [170] Hong Hua Fang et al. “Photoexcitation dynamics in solution-processed formamidinium lead iodide perovskite thin films for solar cell applications”. In: *Light: Science & Applications* 2016 5:4 5.4 (Dec. 2015), e16056–e16056. ISSN: 2047-7538. DOI: 10.1038/lsa.2016.56. URL: <https://www.nature.com/articles/lsa201656>.
- [171] Wolfgang Tress et al. “Performance of perovskite solar cells under simulated temperature-illumination real-world operating conditions”. In: *Nature Energy* 2019 4:7 4.7 (June 2019), pp. 568–574. ISSN: 2058-7546. DOI: 10.1038/s41560-019-0400-8. URL: <https://www.nature.com/articles/s41560-019-0400-8>.
- [172] Maximilian T. Sirtl et al. “The Bottlenecks of Cs<sub>2</sub>AgBiBr<sub>6</sub> Solar Cells: How Contacts and Slow Transients Limit the Performance”. In: *Advanced Optical Materials* 9.14 (July 2021), p. 2100202. ISSN: 2195-1071. DOI: 10.1002/ADOM.202100202. URL: <https://onlinelibrary.wiley.com/doi/10.1002/adom.202100202>.



- [173] Haizhou Lu et al. "Vapor-assisted deposition of highly efficient, stable black-phase FAPbI<sub>3</sub> perovskite solar cells". In: *Science* 370.6512 (Oct. 2020). ISSN: 10959203. DOI: 10.1126/SCIENCE.ABB8985. URL: <https://www.science.org/doi/full/10.1126/science.abb8985>.





## PEROVSKITE RESEARCH

---

I completed my PhD in the lab of Prof. Michael Grätzel. During my time I focused on optical characterization of thin film perovskite solar cells. I used standard experimental equipment to perform PL, TRPL, PLQY, UV-Vis absorption, and JV experiments. My focus with these experiments was on data analysis and interpretation. I built several custom experiments, including temperature dependent versions of PL, PLQY, and JV experiments, and a setup allowing for simultaneous emission and excitation PL experiments.


Due to the high sample variability when fabricating perovskite solar cells, I came to the realization that any results should be analyzed through a statistical framework. To facilitate this I automated all the experiments in my lab and built custom analysis toolkits to quickly perform these statistics.

My main interest became understanding the fundamental mechanisms at play yielding the observed PL spectra. I especially became interested in explaining the causes of the increased blackbody temperature observed across all perovskite spectra. To investigate I developed experiments which combined temperature dependent PL, PLQY, and JV measurements. I also became interested in describing the effects of reversible and irreversible degradation on cell performance which required long-running experiments with heavy data analysis requirements.

## PUBLICATIONS

---

Thermodynamic stability screening of IR-photon processed multication halide perovskite thin films

 S. Sanchez, B. Carlsen *et al.*

 2021  J. Mater. Chem. A Vol.9, Issue 47

 [DOI](#)

Performance of perovskite solar cells under simulated temperature-illumination real-world operating conditions

 W. Tress, K. Domanski, B. Carlsen *et al.*

 2019  Nat Energy Vol.4, Issue 7

 [DOI](#)


Transient Photovoltage Measurements on Perovskite Solar Cells with Varied Defect Concentrations and Inhomogeneous Recombination Rates

 Z.S. Wang, F. Ebadi, B. Carlsen, W.C.H. Choy, W. Tress

 2020  Small Methods Vol.4, Issue 9

 [DOI](#)

Vapor-assisted deposition of highly efficient, stable black-phase FAPbI<sub>3</sub> perovskite solar cells

 H. Lu, Y. Liu, *et al.*

 2020  Science Vol.370, Issue 6512

 [DOI](#)

## SOFTWARE DEVELOPED

---

 **Thot**

Data management and analysis framework for researchers.

 **Easy Biologic**

Python package for controlling Biologic potentiostats.

 **Easy SCPI**

Python package for controlling SCPI (Standard Control of Programmable Instruments) devices.

 **Analysis Libraries**

Analysis tools for evaluating optical, electrical, and other types of experiments.

## ACADEMIC TEACHING

---

General physics - Mechanics

Statistical thermodynamics

Differential geometry

## ATHLETIC TEACHING

---

**Brazilian Jiu Jitsu**

Adults

**Muay Thai**

Adults + Kids

**Skiing**

Adults + Kids

**Snowboarding**

Adults + Kids

**Wakeboarding**

Kids

## ACTIVITIES

---

Rock climbing

Skiing + Snowboarding

Mountain biking

Brazilian Jiu Jitsu

Muay Thai

Olympic weightlifting

Hacking competitions

Programming

Reading

## INTERESTS

---

Math

Physics

Computer science

Philosophy

Psychology

History

Economics

Art